FROM BIPEDAL LOCOMOTION TO PROSTHETIC WALKING: A HYBRID SYSTEM AND NONLINEAR CONTROL APPROACH

A Dissertation
Presented to
The Academic Faculty

by

Huihua Zhao

In Partial Fulfillment
of the Requirements for the Degree
Doctor of Philosophy in the
The George W. WoodRuff School of Mechanical Engineering

Georgia Institute of Technology
December 2016

FROM BIPEDAL LOCOMOTION TO PROSTHETIC WALKING: A HYBRID SYSTEM AND NONLINEAR CONTROL APPROACH

Approved by:

Professor Aaron D. Ames,
Committee Chair
School of Mechanical Engineering &
School of Electrical and Computer Engineering
Georgia Institute of Technology

Professor Ayanna M. Howard
School of Electrical and Computer Engineering
Georgia Institute of Technology

Professor Jonathan Rogers
School of Mechanical Engineering
Georgia Institute of Technology

Professor Daniel Goldman
School of Physics & School of Biology
Georgia Institute of Technology

Professor Jun Ueda
School of Mechanical Engineering
Georgia Institute of Technology

Date Approved: August 12 2016

To my mom,

and my wife,

for never ceasing in their love, encouragement, and support as I have grown through my life.

ACKNOWLEDGEMENTS

I would first like to thank my mom for her endless and unconditional support during my entire education, for inspiring me always chasing the best. I would like to thank my wife, Huanlin for her continuously encouraging and supporting, for her accompanying through all these tough but fruitful days. I would not make this far without their support.

I would put my great attitude to my advisor, Dr. Aaron Ames for his guidance and support throughout my research work, and for his enthusiasm for theoretically succinct that points me the right way to pursue. I would also have my thanks to my friends and teammates: Eric Ambrose, Jonathan Horn, Wenlong Ma, Jacob Reher, Victor Paredes, Shishir Yadukuma, Ayonga Hereid and Matthew Powell for sharing valuable ideas and insights with me that finally leads me to accomplish this much. Each of you have given of your time, energy, and expertise and I am richer for it. I would also extend my sincere gratitude to my reading committee Dr. Rogers, Dr. Ueda, Dr. Goldman and Dr. Howard for their keen supports in making this work a valuable literature. It's their insights and great mind that inspire my research and lead me through the puzzles.

TABLE OF CONTENTS

LIST OF TABLES

LIST OF FIGURES

SUMMARY

When modeled after the human form, humanoid robots more easily garner societal acceptance and gain increased dexterity in human environments. During this process of humanoid robot design, research on simulated bodies also yields a better understanding of the original biological system. Such advantages make humanoid robots ideal for use in areas such as elderly assistance, physical rehabilitation, assistive exoskeletons, and prosthetic devices. In these applications specifically, an understanding of human-like bipedal robotic locomotion is requisite for practical purposes. However, compared to mobile robots with wheels, humanoid walking robots are complex to design, difficult to balance, and hard to control, resulting in humanoid robots which walk slowly and unnaturally. Despite emerging research and technologies on humanoid robotic locomotion in recent decades, there still lacks a systematic method for obtaining truly kinematic and fluid walking. In this dissertation, we propose a formal optimization framework for achieving stable, human-like robotic walking with natural heel and toe behavior. Importantly, the mathematical construction allows us to directly realize natural walking on the custom-designed physical robot, AMBER2, resulting in a sustainable and robust multi-contact walking gait. As one of the ultimate goals of studying human-like robotic locomotion, the proposed systematic methodology is then translated to achieve prosthetic walking that is both human-like and energy-efficient, with reduced need for parameter tuning. We evaluate this method on two custom, powered transfemoral prostheses in both 2D (AMPRO1) and 3D (AMPRO3) cases. Finally, this dissertation concludes with future research opportunities.

CHAPTER I

INTRODUCTION

Bipedal humanoid robots[1] are ideal in applications such as assisted rehabilitation, exoskeletons and prostheses. In their design, it is essential that humanoid robots walk as humans themselves do. After millions of years of evolution, human locomotion has evolved to be elegant, robust and energy efficient, largely due to the heel and toe behavior of feet. Using the heel-off at the end of single support phase, a human can lift the swing leg higher, and thus achieve greater foot clearance without bending the swing knee significantly [116], [117]. With the whole body rotating around the stance toe joint, much less energy is required for human to move forward because of the beneficial utilization of rotational momentum, a phenomenon which is found to be important for achieving fast walking [104]. With changing ground contact points of the feet, human can also be more adaptable to various terrains. Therefore, it is of obvious importance of reproducing these behavior in robots when attempting to achieve human-like robotic walking.

Research of simulating human locomotion on bipedal robots can help us better understand the mechanism of natural walking. One immediate motivation is to help design rehabilitation devices or powered prostheses which will actively aid or restore legged locomotion to individuals suffering from lower limb muscular impairments, weakness, or amputations [120]. Despite the rapid development of actuation, sensing and on-board computation for bipedal robots, these advancements are yet to be fully extended in the development of powered prostheses. As a result, the amputees' choices are still limited to passive devices that can not reproduce the behavior of a

[1]The concept of a humanoid robot lacks rigorous definition. For example, a wheeled robot with human-like upper body and a jointed, bipedal robot with no upper body at all may both be classified as humanoid. This dissertation is focused on locomotion. Therefore, bipedal locomotion is the key feature used to define humanoid robots. In this dissertation, the terms humanoid and bipedal will be used interchangeably.

biological leg. In particular, there are several major difficulties when implementing the knowledge we gained from bipedal robotic walking to prosthetic locomotion. For example, while bipedal robots usually have the full state information of a system, prosthetic devices can only access limited local sensory information, which constrains them from interacting with human subjects in a well-coordinated way. Mechanically, prosthetic devices need to be light while at the same time strong enough to support human weight. Additionally, in order to be useful in typical applications, prosthetic controllers also need to be designed to work across different subjects and motion types. While most of these problems are still open, this dissertation will explore some of them with the motivation to develop a systematic methodology to bridge the research gap between bipedal robotic locomotion and prosthetic walking.

1.1 Research Problems

We begin by reviewing the state of art of both bipedal locomotion and powered prosthetic control research. More detailed literature review will be discussed in Chapter 2. Bipedal robotic walking has been studied from a variety of viewpoints, many of which are aimed at achieving human-like locomotion capabilities, i.e., reproducing the elegance, efficiency and robustness found in human walking. From this perspective, the role of multi-contact foot behavior is found to be essential to the humans in both biomechanical research and robotic control field. Coming along with the rapid development of bipedal robotic research, powered prostheses are also vigorously studied, and different intelligent controllers (as compared to passive prostheses) have been explored. However, most of them are limited to linear controllers with the requirement of a finite state-machine, which results inevitable heuristic parameter tuning. Additionally, controller development of these methods usually involves with extensive clinical testing with amputee patients, which is both time-consuming and costly.

1.1.1 Multi-Contact Bipedal Locomotion

Human locomotion gaits consist of multiple instances of both single and double support phases (or domains) [114], with switching between these phases occurring

changes in contact points with the environment, e.g., a heel-strike or a toe-off. This multi-domain, or multi-contact nature of human gaits results in walking that is both fluid and efficient [63], [72]. While dealing with these dynamic contact points changes is seemingly effortless for a human, it is challenging to incorporate these advantages into bipedal robot locomotion. Propelled by its advantages and challenges, multi-contact foot locomotion has been actively studied, aiming to reproduce the results of evolution.

Gait pattern generation and gait planning methods are adopted to design the foot trajectory specifically for the multi-contact foot behavior in [50], [59]. An optimized walking gait with two domains is proposed in [31] for a seven-link biped. Recent works of Nishiwaki *et al.* [95], Sellaouti *et al.* [104] and Li *et al.* [77] show that the presence of multi-contact behavior allow robots to perform longer strides, walk at a higher speed, and require lower torque. However, the vast majority of these approaches attempt to reduce the complexity of the problem through simplifying assumptions such that the stance foot is flat on the ground, i.e., the foot roll only happens at the double-support phase or swing phase. As a result, the foot push off at the end of single-support phase is lacking, which will yield a significant torque increase at the ankle joint in order to propel the body forward. Additionally, the trajectory is designed revolving around the Zero Moment Point (ZMP) [122]. Consequently, the performance of the bipedal robotic walking is constrained by these assumptions. Therefore, bipedal robots can not utilize advantages of the multi-contact feature of human locomotion.

Simulated robotic walking with only two domains can be found in [35], [119], in which the authors show that the walking gait with toe roll (i.e., foot push) helps with the reduced torque and faster walking speed. From the author's knowledge, noticeably lacking from existing methods from any of these perspectives is a formal way to generate multi-contact locomotion in a manner that is both formally correct as well as physically realizable.

1.1.2 Powered Lower-Limb Prostheses

In the context of locomotive activities of daily living, the lower-limb wearable robots can be generally divided into two categories—orthotic devices for mobility assistance and prosthetic devices for locomotion restoration. This dissertation focuses on discussing the development on prosthetic devices with a particular interest on transfemoral prostheses.

There are approximately 1.9 million people in the United States alone that are living with limb loss, and this number is expected to double by the year 2050 [147]. Despite this large demographic, the current market for commercial prostheses remains largely limited to energetically passive prosthetic devices, limiting the day-to-day life of amputees [131]. In particular, amputees with energetically passive prosthetic devices are found to be less stable, constrained in locomotion capabilities and require more force and energy during locomotion than healthy humans [39], [130]. Powered-lower-limb prostheses capable of providing net power in conjunction with various prosthetic controllers have been developed with the potential to regain full mobility in various terrains for amputees. Additionally, with intelligent high-level motion planning controllers, active prostheses also have the potential to increase self-selected gait speed and gait symmetry while reducing metabolic cost and wear-and-tear on the amputees' unaffected joints [120].

While these potential benefits are compelling from various perspectives, there still remain many engineering challenges such as mechanical design, system modeling, control development, and human-device interaction [120]. In particular, how can the prosthetic devices be as compact and light as possible while still can mechanically provide enough torque to bear the human weight during the stance phase? More importantly, with the lack of model information and sensory feedback, how to design and validate control approaches that can be generalized to different devices, different subjects and different motion types? How does the device interact with the subject (for example, gait detection or phase detection) in an intuitive way such that there is minimum instrumental requirement on the healthy human body side? Motivated

by control and system design of bipedal robotic systems, this dissertation aims to taking the first steps of answering these challenges, via the idea of translating these methodologies from bipedal locomotion to prosthetic walking.

1.2 Overview of Experiment Robots

A crucial part of research is to develop theorem or algorithm that can be validated on hardware with the goal of improving performance, which is especially true for humanoid and prosthetic robot studies. With this emphasis in mind, this dissertation implements the research results on four different robot platforms, which are all custom designed and manufactured by the AMBER (**A**dvanced **M**echanical **B**ipedal **E**xperimental **R**obot) Lab. AMBER1 is the first bipedal robot built by the AMBER Lab. AMBER1 is 61 cm tall with a total mass of 3.3 kg. It is made from aluminum with carbon fiber calves for the purpose of weight saving. Powered by 4 DC motors, it is controlled through LabView software by National Instruments. With pointed foot (no actuation at the ankle) and walking on a treadmill, AMBER1 is designed with the goal of studying underactuated dynamic robot walking. In this dissertation, we are going to use it as a robot platform for prosthetic controller design and validation. Note that, the motivation is to propose and validate the idea that a bipedal robot platform can be used for prosthetic control design and verification, therefore, could potentially reduce clinical testing effort for amputees.

AMBER2, as indicated by the name, is the second robot built by the AMBER Lab. Powered by 6 DC motors, it's a planar robot with the coronal plane movement constrained by a circular boom. Importantly, with special designed feet with articulated heel and toe joints, AMBER2 is constructed particularly for the goal of achieving human-like multi-contact robotic walking, i.e., verifying the proposed general optimization framework for multi-domain walking.

Two powered transfemoral prostheses AMPRO1 & 3 are designed and constructed for this work. AMPRO stands for **AM**BER **Pro**sthesis. As the first transfemoral prosthesis custom designed by the AMBER Lab, AMRPO1 is over designed with two 376 W brushless direct current (DC) motors for both the ankle and knee joints.

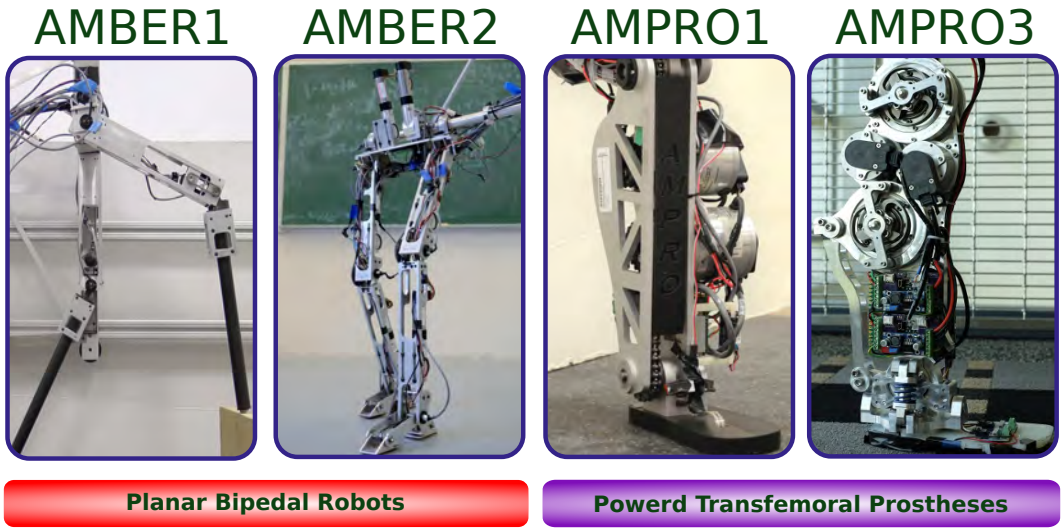

Figure 1: Experimental robot platforms considered in this dissertation.

Driven by a roller-chain mechanism, it can achieve responsive and accurate tracking. The major results of prostheses control validation in this dissertation will be discussed based on this device. With experience gained from AMPRO1, AMPRO3 is a newly designed transfemoral prosthesis that incorporates several improved design. Firstly, it is significantly lighter (3.5 Kg less weight) and smaller (both shorter and narrower) than AMPRO1. With two 206 W brushless DC motors, the actuation units also embed a torsional spring between the motor and the joint, therefore, yielding a *serials elastic actuator* (SEA) for each joint. A 6-axis load cell is added in serial between the shank and the foot to provide more responsive force feedback information. Additionally, a passive ankle roll joint with springs is considered to let amputees move freely in the coronal plane, which aims to improve walking and standing comfortabilities of daily use. Preliminary testing of a 3D multi-contact prosthetic gait will be carried out with this device. Future research can be focused on smart SEA control with the goal of improving energy performance and prosthetic walking comfortability.

Figure 1 shows the physical hardware of the four robot platforms. More details about each device and the actual experimental setup will be discussed in the corresponding chapters.

1.3 Thesis Contribution

Study of human-like robotic locomotion help us understand human walking better, therefore, can facilitate the design and control of powered prostheses. As the focus of this dissertation, the overarching contribution is to propose a framework which allows us to translate control and optimization methods from bipedal locomotion to prosthetic walking, to be more specific, via a hybrid system and nonlinear control approach. Figure 2 visually illustrates the main contribution and approach of this dissertation.

With the ultimate goal of achieving human-like powered prosthetic walking in mind, we begin with developing a general framework of multi-domain bipedal robotic locomotion. A bipedal robot platform is designed to experimentally verify this methodology. Since an amputee-prosthesis system can be naturally modeled as a bipedal robot hybrid system, the optimization framework developed based on bipedal robots can also be utilized for prosthetic gait design. Different from bipedal robots, prosthetic devices only have access to local sensory feedback information, therefore limiting admissible control strategies that can be applied for powered prostheses. Motivated by this fact, an optimization-based decentralized nonlinear controller is developed based on the amputee-prosthesis hybrid system. Because of the formal mathematical modeling, the prosthetic controller can be designed and validated in simulation formally. Additionally, this approach allows one to test the controller on a bipedal robot platform experimentally, therefore, could potentially reduce clinical tuning effort. Finally, prosthetic devices are built for testing with human subjects. The results show reduced parameter tuning, improved tracking performance and better energy efficiency [2].

Based on the summary above, this dissertation presents two main contributions. Firstly, a formal multi-domain optimization framework for achieving multi-contact

[2]This research has approval from the Institutional Review Board with IRB2014-0382F (for experiments done at Texas A&M University) and IRB00000548 (for experiments done at Georgia Institute of Technology) for testing with human subjects

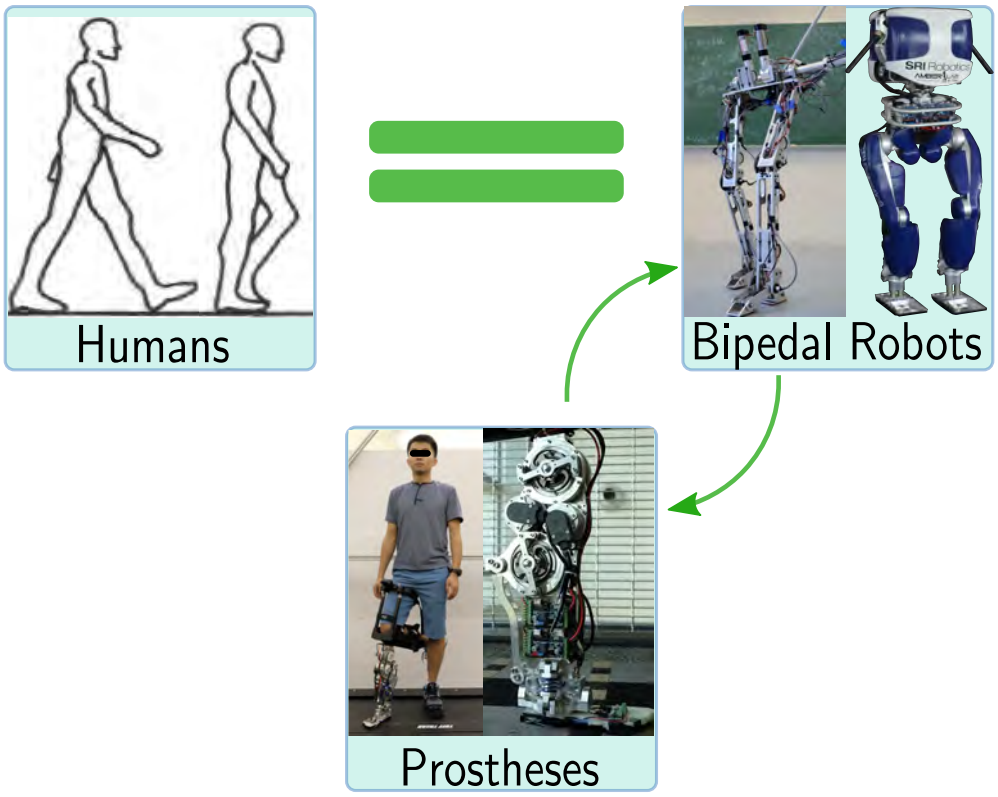

Figure 2: Overarching goal of this dissertation is to propose a novel framework of testing and verifying prosthetic controllers based on robotic platforms in both simulation and experiment. This goal is achieved via two steps. The first step is to realize human-like multi-contact robotic locomotion on bipedal robots. With realizing the first goal, the bipedal robots can be qualified as a testing platform for design and validating prosthetic controllers. The end result is that clinical testing effort can potentially be shifted from humans to bipedal robots.

bipedal robotic walking is proposed, and realized experimentally on a robot platform AMBER2. Inspired by the heel and toe behavior encoded in human walking, this approach begins with the analysis of human locomotion data and uses the data to motivate the construction of a multi-domain hybrid system model to represent a multi-contact robotic walking gait. Virtual constraints extracted from reference human locomotion data are employed to develop a human-inspired feedback linearization controller for exponential convergence of tracking. To guarantee impact invariance, *partial hybrid zero dynamics* (PHZD) are considered explicitly as nonlinear constraints to yield stable multi-domain walking. Considering physical limitation constraints at

the same time, the end result is a human-inspired multi-domain optimization framework, which, when converges, will generate stable multi-contact bipedal walking trajectories that can be implemented on robot hardware directly. Through a trajectory reconstruction strategy, this mathematical construction has been successfully realized on a physical bipedal robot, AMBER2, achieving sustainable robotic walking that displays remarkably human-like multi-contact feet behavior.

Secondly, the proposed systematic methodology—including optimization and nonlinear control—is extended from bipedal locomotion to prosthetic walking on two custom-built powered transfemoral prostheses. Compared to the conventional proportional and derivative (PD) based prosthetic controllers, the goal of this dissertation is to achieve prosthetic walking that is human-like and energy-efficient, along with reduced parameter-tuning requirement. These objectives are realized via two steps. The first step is to generate a multi-contact prosthetic gait automatically based on a multi-domain hybrid system model. Research shows that joint trajectory pattern in human locomotion is invariant across individuals and walking speeds. Therefore, this dissertation proposed the idea of using an unimpaired human subject—which has similar anthropomorphic parameters as the amputee—as a reference for prosthetic gait design. In particular, unimpaired human locomotion data is collected via an Inertial Measurement Unit (IMU) motion capture system. Utilizing the collected healthy human gait as a reference, the human-inspired multi-domain optimization problem—subject to both PHZD constraints and physical constraints—is applied to design stable multi-contact prosthetic gaits that can be implemented on physical prostheses directly.

The second step is to formulate a control Lyapunov function based controller to achieve rapidly exponential convergence of the designed gaits. Synthesized with variable impedance control which is implemented as a feed-forward control term, a quadratic program based method is leveraged to design an online optimization-based controller. The end result is a prosthetic controller that can achieve exponential tracking of the designed gaits without requiring accurate model information (i.e., it is model independent). Before testing on real human subjects, the proposed

methodology—including the gait generation method and the optimization-based nonlinear controller—is verified successfully in both simulation and experiment on a bipedal robot platform, AMBER1.

With the goal of testing this approach on real human/amputee subjects, a powered transfemoral prosthesis AMPRO1 is designed and built from scratch. Improved tracking and reduced energy consumption (compared to traditional PD control) are seen when this methodology is implemented experimentally with both unimpaired and amputee subjects. Importantly, the resulting multi-contact prosthetic walking captures the essentials of natural human locomotion both kinematically and kinetically.

To further validate this systematic methodology in more practical situation, a 3D asymmetrical amputee-prosthesis hybrid system model is considered for more realistic prosthetic gaits design. Specific requirements—such as amputee comfortability, human-likeness, gait symmetry and physical limitations for hardware implementation—are discussed explicitly in order to quantify a well-designed prosthetic gait. A 29 degrees of freedom 3D bipedal robotic model with two passive compliant feet and a passive ankle roll joint is considered to model the asymmetric amputee-prosthesis system. Leveraging a computation efficient two-step direct collocation optimization method, in the framework of which both the hybrid zero dynamics constraints and the prosthetic gait requirements can be imposed as explicit nonlinear constraints, a 3D multi-contact prosthetic gait can be automatically generated in an optimal fashion. A 3D capable prosthetic device AMPRO3 is designed and built particularly for the purpose of experimental implementation. The preliminary experiment results of AMPRO3 indicate that the proposed method has a promising potential to improve the everyday lives of amputee patients.

1.4 Thesis Outline

In this dissertation, there are total of 8 chapters. Chapter 1 and Chapter 2 introduce the problems that this dissertation is aiming to solve and review current approaches. The main results are discussed from Chapter 3 to Chapter 7. A graphical

illustration of the flow of topics and connections between different chapters is shown in Figure 3. The arrows indicate that discussion of a particular chapter depends on the previous chapter. Finally, the conclusion is presented at Chapter 8. More detailed introduction of each chapter is illustrated as the following.

Chapter 2 takes a detailed review about both bipedal robot research and active lower-limb prosthetic control. The bipedal robotic research is discussed with a special focus on dynamic robotic locomotion with feet. Three types of footed walking including ZMP based walking, passive walking and hybrid zero dynamics walking are considered. The approach utilized in this dissertation is presented at the end of the review of bipedal robots. For the active prosthetic control discussion, we put a strong focus on variable impedance control with illustrating its both advantages and disadvantages. Impedance parameter estimation methods are covered and the limitation is discussed. On the other end of the spectrum, as motivated by the control of bipedal robotic research, virtual constraints based prosthetic controllers are deliberated. The novel control approach in this dissertation is illustrated at the end.

Chapter 3 presents the general framework of a hybrid system based multi-domain optimization that will be used to generate multi-contact gaits for both bipedal robots and prostheses. This chapter begins with the analysis of human locomotion data and uses it to motivate the construction of a hybrid system model representing a multi-contact walking gait. Further motivated by the human data, human-inspired controllers are developed and used in the formulation of the optimization problem. In particular, with human data as the cost function, this optimization problem is subject to both PHZD constraints (for gait stability) and physical constraints (for hardware implementation), the end result of which is stable human-like multi-domain walking gaits in simulation. Importantly, a main theory is developed to formally guarantee that if certain assumptions were met, the optimized gait has a limit cycle, i.e., it is stable in a hybrid sense.

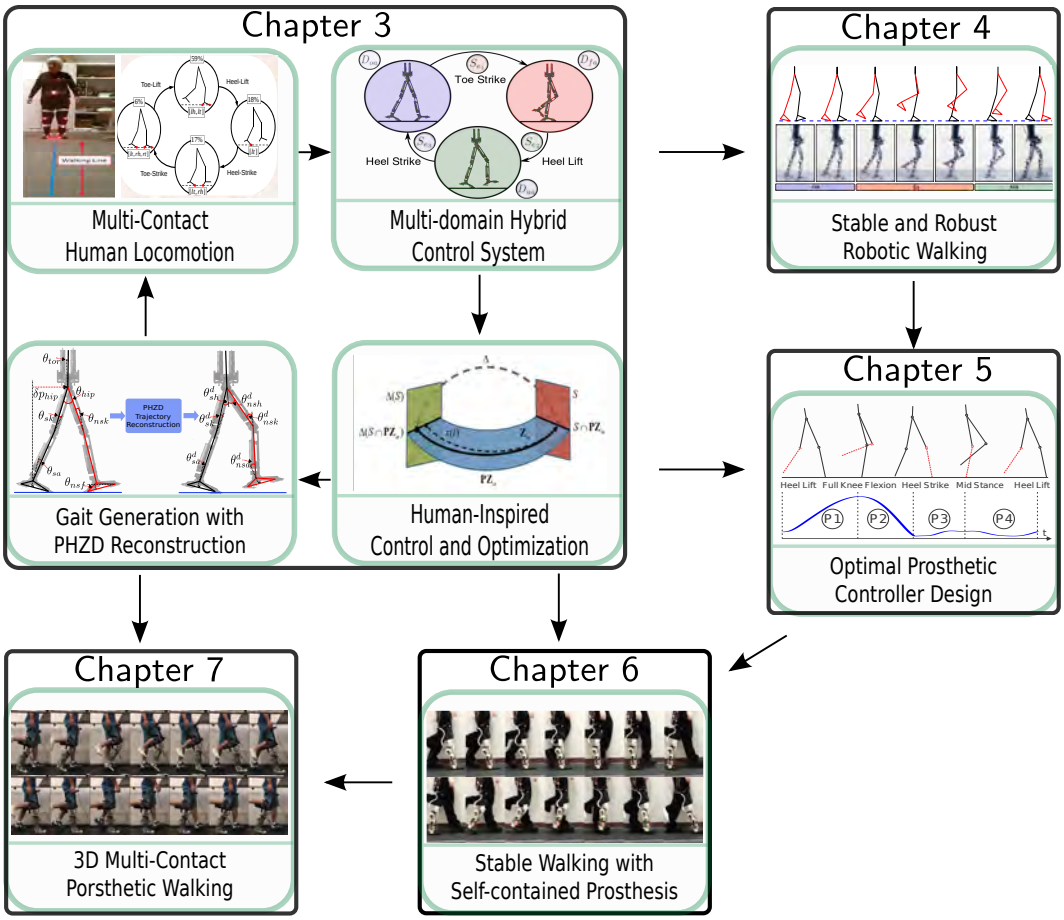

Figure 3: Flow of topics and connections between the main chapters.

Chapter 4 focuses on translating the mathematical framework developed in Chapter 3 onto a physical bipedal robot: AMBER2. The experimental platform of AMBER2, including hardware design, experiment setup and control architecture, is introduced first. With the specially designed artificial feet (heel and toe joints are passively turnable), AMBER2 is constructed with the goal to achieve human-like locomotion with multi-contact foot behavior. The detailed hybrid system modeling of AMBER2 is discussed, which also serves as an explicit example of the general discussion in Chapter 3. In particular, a corollary is proposed based on the main theory to show that with the control method chosen as the human-inspired controllers, the optimized gait is mathematically stable for AMBER2. Finally, the experiment results of AMBER2 are presented with showing sustainable and robust human-like multi-contact robotic walking.

Chapter 5 starts with a brief review about the variable impedance control. Inspired by a newly developed hybrid system controller, *rapidly exponential stabilizing control Lyapunov function* (RES-CLF) control, a *model independent quadratic program* (MIQP) strategy is proposed for prosthetic joints control. When coupled with impedance control, which will be served as a feed-forward term, the end result is a novel optimization-based controller which preserves the model independent property while at the same time guarantees rapidly exponential convergence. For the purpose of control validation, this dissertation propose the idea of using bipedal robot as a testing platform. In this way, different prosthetic controllers can be designed and tested on a robotic platform, which could potentially reduce clinical testing time for amputees. In particular, the proposed controller is successfully verified on a robot platform: AMBER1 in both simulation and experiment at the end of this chapter.

Chapter 6 presents the experimental implementation of the systematic methodology, including both trajectory generation optimization and nonlinear model independent control, on a physical transfemoral prosthesis and human subjects. The design of a powered transfemoral prosthesis is discussed first, followed by the experiment setup and embedded control architecture. An IMU motion capture system is developed specifically to capture reference human trajectory for prosthetic gait design for a particular subject. With the MIQP+Impedance controller running online with on-board computation, we achieved stable prosthetic walking with both unimpaired subject and amputee subject. Analysis of the experiment results showed improved tracking performance and energy efficiency of the novel controller when compared to PD controller. Utilizing machine learning method, automatic motion transitions among standing, level-ground walking and stair climbing is realized successfully, which validates that this method can be implemented for different motion types.

Chapter 7 extends the multi-domain optimization framework from 2D symmetric prosthetic gait generation to 3D asymmetric gait design. Motivated by the objective to obtain a well-designed prosthetic gait, we propose a novel two-step asymmetric 3D gait design method for generating human-like multi-contact prosthetic gaits which also satisfy various realistic requirements such as human comfortability and

energy consumption. In particular, a 3D bipedal hybrid system model is developed to characterize the asymmetric multi-contact amputee-prosthesis locomotion system. Two compliant feet with high stiffness passive springs are included in the model to capture effects of compliance in both the human and prosthetic feet. Imposing the requirements as constraints and objectives, a novel two-step direct collocation method is utilized to solve the optimization problem efficiently with generating human-like prosthetic gaits for this asymmetric 3D model.

A 3D capable transfemoral prosthetic device with a passive ankle roll joint for more comfortability to the testing subject during walking, is designed and built from ground up to verify the designed gaits. The preliminary results are presented and discussed at the end of this chapter.

Chapter 8 concludes with discussion remarks and future research possibilities. Co-operating with clinical institutes for testing with more amputees would be necessary for further validation of the proposed method in this dissertation.

CHAPTER II

RESEARCH BACKGROUND AND LITERATURE REVIEW

Bipedal robots are more mobile than wheeled robots, especially when moving on rough terrain, stairs and in environments with obstacles. These advantages are mainly due to the reason that the feet motion allows bipedal robots to be adaptable to different ground conditions. The complex feet motion also contributes to smaller torque, fast motion and more natural appearance of bipedal robotic walking. In this section, we will review the studies about bipedal robots with a special focus on bipedal walking with feet. Motivated by research of bipedal robots, active prosthetic control is also reviewed with emphasis on variable impednace control.

2.1 Bipedal Locomotion with Feet

The topic of bipedal robotic locomotion has been studied since 1960. The first functioning bipedal robots was developed by Kato in 1970s [67]. Since bipedal robots walk with only one stance foot on the ground most of the time, the stability has always been the most important consideration during the control design.

2.1.1 Flat-Foot Walking

Initial approaches constrain the center of mass (CoM) position to be within the area of the supporting foot [67]. A double support phase is required to shift the CoM position from one foot to another, and then the next step carries on. Therefore, the robot is static stable at any moment. These methods require massive amount of energy and generate very slow walking. Motivated by the fact that the stability (not falling) of locomotion is highly regulated by the net body momentum, Zero Moment Point (ZMP), first proposed by [23], has been one of the most accepted methods for bipedal locomotion control design due to its dynamic feature, simple intuition

Figure 4: An example list of several well-known footed robot with different types of locomotion style.

and easy implementation [123]. In particular, the ZMP is defined as a point on the ground about which total moments of the active forces equal to zero [42]. If the ZMP is within the convex hull of all contact points between the feet and the ground, the biped robot will keep stability, i.e., walking without fall or tip. Basically, common steps of ZMP based methods are to first design a desired trajectory that satisfies ZMP conditions. Then hip motion and other joint trajectories are derived inversely to achieve that desired ZMP trajectory [87]. The advantage of this method is that the stability margin can be designed to be large in prior. However, since the hip motion is constrained by the ZMP conditions and the foot has to be flat on the ground, torque requirement is usually large and energy consumption is high. Step size and walking speed are also greatly constrained because of the lack of foot push. One way to reduce the total momentum for easier ZMP trajectory design is to keep the center of mass low, i.e., to keep the knee unnaturally bending with a big angle. A lot of famous humanoid robots walk with a flat-foot fashion based on the ZMP approach, for example, Honda Robot ASIMO [54], Sony's biped SDR-4X [45], Kawada's humanoid HRP-2 [66], Aldebaran's NAO [14] and Jogging Johnnie at the Institute of Applied Mechanics of Munich [46], to name a few. The left two pictures of Figure 4 show the robot HRP-2 and ASIMO as examples to compare with other two types of locomotion with feet.

2.1.2 Passive Walking with Rolling Feet

Another approach of bipedal walking with roller feet is the passive walking first introduced by McGeer [83], [84], which shows that a bipedal robot can walk down a slope without any actuation. Based on these initial results, minimum actuation effort has been added to the control design with achieving efficient locomotion on flat ground in both 2D [132] and 3D [36]. The resulting locomotion is also kinematically human-like because of the added knee joint and the roller feet. While this type of walking is not applicable for complex motion types (for example, stand still, stair climbing and rough terrain walking), it is useful to study about the mechanism of human locomotion and brings emphasis to the point that mechanical design of a bipedal robot (for example, the capability of foot roll) is as important as the control algorithm.

2.1.3 Multi-Contact Walking

With the goal of releasing full mobility potential of humanoid robots, study of foot motion has become an active area in bipedal robotic research. Research in [95] starts with analysis of toe joints with showing that a passive toe roll at the beginning of swing phase could achieve 80% faster locomotion and increase the step height for stair climbing. Similar type of passive toe movement is also studied in [59]. A gait pattern generation method with considering physical constraints (e.g., torque requirement, actuator speed) is proposed to generate different foot motion. A spline function based parametric optimization method is proposed in [31] to generate walking gait with two domains for a seven-link biped. In [50], a heel contact behavior is added along with the passive toe roll for designing gait patterns of bipedal robots. The results show that this heel and toe behavior increase the support area during double support phase and eliminate knee stretch singularity. Similar results of bipedal walking with passive toe joints can also be found in, [13], [30], [55], [77]. However, the vast majority of these approaches attempt to reduce the complexity of the problem through simplifying assumptions that the stance foot is flat on the ground, i.e., the foot roll only happens at the double-support phase or swing phase. During the flat-foot stance phase, ZMP

is then used to synthesis the constrained hip motion for the robots. Consequently, the performance of the bipedal robotic walking is constrained by this assumption. For example, the foot push off at the end of single-support phase is lacking, which will result a significant torque increase at the ankle joint in order to propel the body forward.

Simulated bipedal walking that allows point contact with feet during the single-support phase is first found in [115]. Faster and smoother walking without requiring the foot to be flat during single-support phase is studied in [104]. In this work, a big size passive toe joint is required for satisfying ZMP conditions during the foot push (i.e., only toe is in contact with the ground) at the single-support phase. Trajectories for the rest domains are also designed to evolve around the ZMP. Through direct regulation of the ZMP for each domain, simulated planar robotic walking with significant rotation of the stance foot (i.e., foot push) during the single-support phase can be found in [35], in which the authors show that the walking gait with foot push helps with the reduced torque and faster walking speed. However, the locomotion type considered in this work does not include heel strike and toe roll. A multi-domain hybrid model based bipedal robot with locking knees and feet is developed in [108] with displaying foot behaviors such as heel strike, toe roll and foot push in simulation. Motivated by energy efficiency and versatility of locomotion, different cyclic gaits have been analyzed for a planar biped robot in [118] in simulation with showing that foot push is useful to reduce the energy consumed in the walking. Two-domain walking with foot push feature is then considered for a 3D bipedal robot model in [119] in simulation. In this work, a recursive NewtonEuler algorithm based optimization method is used to design piece-wise trajectories for each domain.

The reviewed work clearly indicate that the multi-contact feature can benefit bipedal locomotion with longer steps, faster walking, less energy and more mobility. However, few of them can capture the whole picture of realistic multi-contact human locomotion. That is said, most of them only consider partial of the multi-contact behavior, i.e., either toe roll or foot push or heel strike is missing. More importantly, because of the controllers or gaits are designed differently based on domains, most

of the methods are only applicable in simulation environment. As a result, there is very few physical robot that can walk like a human with displaying all the heel and toe behavior. To the authors' knowledge, only the PETMAN from Boston Dynamics can walk naturally in a dynamic multi-contact fashion (a YouTube video of which can be seen in [8]), yet it requires massive amount of energy with hydraulic actuators and their approach is classified to be unknown. Motivated by these problems, this dissertation proposes a formal way to generate multi-contact locomotion in a manner that is both formally correct as well as physically realizable.

2.1.4 Proposed Control Approach

Recent work from the AMBER Lab has looked toward human locomotion for inspiration for the synthesis of walking controllers with the goal to achieve human-like robotic locomotion. Point-foot model with under actuation is considered in the work [134], [143]; models with one fully actuated domain, i.e., flat-foot walking, are discussed in the cases of both 2D walking [79] and 3D walking [17]. While these work is constrained to either point-foot or flat-foot walking, it takes the first steps forward formally generating human-like bipedal robotic walking from human data in the cases of both under- and fully- actuation. Therefore, with these results in hand, this dissertation is ready to present a formal way to achieve multi-contact robotic walking through the inspiration of human locomotion.

With the goal of exploring a general way to produce multi-contact robotic bipedal locomotion, this dissertation begins by noting that the multi-contact behavior (including both continuous dynamics and discrete dynamics) presenting in human locomotion can be represented as a hybrid system model. Therefore, a hybrid system model with multiple domains is constructed to describe the multi-contact robotic locomotion in a general form. Further motivated by the human locomotion data, the *extended canonical walking function* (ECWF) is utilized to serve as a low dimensional representation of the human locomotion system. This allows for the formulation of human-inspired controllers that drive outputs of the robot to the outputs of human (as represented by the ECWF) in an exponential convergence fashion. In regard of the fact that

the multi-contact locomotion consists of discrete dynamics, i.e., impacts, a multi-domain optimization framework is proposed to generate controller parameters that yield invariant tracking even through impacts. More importantly, this optimization construction is also subject to specific physical constraints, such as torque bounds and foot scuffing prevention; therefore, the obtained parameters can be successively translated to physical robots. Finally, with the PHZD reconstruction strategy, this formal result can be realized on physical robots to achieve multi-contact robotic locomotion.

2.2 Active Lower-Limb Prosthetic Control

The daily living of transfemoral amputees is greatly limited by the use of energetically passive prostheses. While the development of passive devices has achieved stable level ground walking, reports indicate that the amputees using them have increased metabolic costs and exert as much as three times the affected-side hip power and torque comparing to healthy human [130]. With passive devices, it is also found that individuals with lower-limb amputations are more vulnerable to fall than able-bodied individuals and often struggle to traverse on ramps and stairs [47], [85]. On the other hand, powered prostheses capable of providing net power for both ankle and knee joints in conjunction with various prosthetic controllers have been developed in recent decades with achieving successful walking on flat-ground [27], [112], stairs [26], [74], [145] and running [105].

Another fundamental advantage of powered prostheses, when compared to the passive ones, is that the powered devices (equipped with on-board microprocessing ability) are capable of interacting with the user in a smart and natural way, while passive devices can only assist the user with a predefined routine, i.e., either bear the weight during the stance phase or bounce forward to finish the swing phase. Therefore, in order to realize the potential of powered prostheses, an intention interface can be designed to allow the users to control the device for different motion behaviors, i.e., switching between different motion primitives. Proposed approaches include using mechanical triggers or compensatory body movements [62]. However, more natural and smooth motion switching strategies are found to be when utilizing pattern

recognition algorithms. With using mechanical sensor data, the intent recognition algorithms are realized in [121] with a maximum $500ms$ delay and in [136] to achieve transitions between 5 modes with over 93.7% accuracy. Combining residual limb electromyography (EMG) signals and the mechanical sensor information, the method in [58] is able to transit between 5 motion primitives with accuracy above 95%.

With particular emphasis on mid-level[1] control of powered prosthetic device, the literature review of this section will mainly focus on various control methods that have been used for lower-limb prosthetic walking. [43] developed a hydraulically actuated knee prosthesis with the "echo control" method to mirror the modified trajectory of a healthy leg on the opposing side. An EMG controlled knee with four damping levels (i.e., breaking one step into four phases), for both swing and stance control, is proposed in [41]. Without requiring a finite state machine, adaptive control is proposed in [125] to produce the desired joint trajectory similar to that of normal persons. A Center Pattern Generator (CPG) based method is proposed to generate virtual knee angle reference for prosthesis in [88]. The generated virtual knee angle reference is then successfully demonstrated in experiment on a physical prosthesis. Among different prostheses controllers, variable impedance control, which is first introduced in [56] as an approach to manipulation, is one of the most common approaches for controlling prostheses (to name a few [26], [57], [106], [112]). In the following section, a more detailed review about variable impedance control is presented. Various impedance parameter estimation methods are also discussed. Different from torque-based control such as impedance control, the kinematic-based controller is introduced as a new trend for prosthetic control. Finally, the control approach proposed in this dissertation is presented in detail.

[1]Commonly, the control architecture of a robotic system can be divided into three levels. The high-level controller is in charge of tasks such as motion intent recognition, contact switch, etc. The mid-level controller generate the actual control input for each motion types. This is the particular level of control that different controllers will be implemented, which is also the focus of this dissertation. The low-level control is usually in charge of realizing the torque commanded by the mid-level controllers on hardware through interacting with motion amplifiers (i.e., motor drivers).

2.2.1 Variable Impedance Control

As one of the most accepted prosthetic controllers, variable impedance control breaks one step cycle into multiple phases, each of which has its own impedance parameters along with the corresponding phase switching parameters. By adjusting the corresponding impedance parameters for different phases or motion types, the controller is expected to mimic the impedance feature of actual human joints, therefore, can potentially recover the mobilities of amputees. With advantages of its simple formula and model independence, impedance control has been applied widely for prosthetic control with great success, for example, stair climbing in [26], [113], motion transitions in [135] and adaptive standing in [75]. However, the main drawback of this method is that currently clinicians tune these parameters by trial and error for each patient [112], [113]. This impedance controller tuning process usually takes four hours on average for each individual as mentioned in [106]. Moreover, multiple sessions are necessary to tune the device for different modes of locomotion such as stair ascent/descent and ramp ascent/descent.

2.2.2 Impedance Parameters Estimation

Considering the shortcoming of requiring parameter tunning of variable impedance control, biomechanical system identification approaches provide possible methods that in principle can be used to select impedance parameters for lower-limb impedance controllers [69], [96]. These approaches consist of both stationary and time-varying impedance identification techniques. With stationary impedance identification methods, the impedance of the joint is assumed to be time-invariant and estimated by perturbing the joint multiple times. While the stationary methods are very well studied, it is limited to impedances only in steady-state mode [68], [126]. On the other hand, the time-varying impedance identification techniques [80] continuously perturb the joints and are able to estimate instantaneous impedance values in dynamic cases. However, these approaches were limited by the amount of experimental data that they required, therefore yielding high experimental cost which could limit their use for individuals.

Inspired by the fact that locomotion outputs are invariant across individuals and walking speeds [33], the author's previous work proposed a computational-efficient algorithm to learn impedance parameters based on the outputs that are generated by solving a human-inspired optimization problem [12]. In particular, by constructing a humanoid robot model with the amputee's physical characteristics, i.e. mass and length information of the individual, the exemplar joint trajectories corresponding to the size of the amputee can be generated using the same multi-domain optimization problem that has been verified on bipedal robots. Once the amputee-specific trajectories are generated, impedance controller parameters can be estimated using a least-squares minimization. While this method has been successfully validated on a testing subject using the Vanderbilt Leg [112] at Rehabilitation Institute of Chicago (a video of which can be seen in [1]), it is limited to only prosthetic knee joint only.

2.2.3 Virtual-Constraints based Control

On the other end of the spectrum, as motivated by the control of bipedal robotic research, virtual constraints (which are imposed by motor actuators as opposite to physical constraints) can be utilized to design a unified reference prosthetic gait for tracking purposes [47], [49], [120], [140]. Compared to the traditional impedance control, this method has several advantages: a) it does not require discretization of a step cycle, therefore, eliminating possible incidents of incorrect phase switching; b) stability can be formalized and analyzed mathematically; c) optimal nonlinear controllers can be applied, which can potentially reduce parameter-tuning and improving prosthesis performance (e.g., reduced power consumption). Motivated by these benefits, multiple past works have successfully implemented this method with achieving prosthetic walking in either simulation or experiment. Control of a powered prosthetic leg through virtual constraints using the Center of Pressure (COP) as a phasing variable was realized in [47]. Further results from the same group have successfully implemented a novel control strategy that unifies the entire gait cycle of a powered knee-ankle prosthetic leg without the need to switch between controllers for different periods of gait (i.e., stance or swing phases) [99]. Robust adaptive control is

utilized to track a predefined trajectory with realizing robust prosthetic walking on a prosthesis robot testing platform [29]. Feedback decentralized controllers for exponentially stabilizing periodic orbits are utilized with achieving stable 3D prosthetic walking in simulation [49].

2.2.4 Proposed Control Approach

Utilizing the impedance controller as a feed-forward term, the work of this dissertation presents a novel prosthetic control method that can be utilized to optimally track the designed virtual constraints with increased robustness and reduced energy consumption. In particular, this control method begins with considering rapidly exponentially stabilizing control Lyapunov functions (RES-CLFs) as introduced in [19]. This class of CLFs can naturally be stated as inequality constraints in torque such that, when satisfied, rapid exponential convergence of the error is formally guaranteed. Furthermore, these inequality constraints can be solved in an optimal fashion through the use of quadratic programs, which yields a novel feedback control methodology: Model Independent Quadratic Programs (MIQP) based upon RES-CLFs. This control was then combined with impedance control to obtain the final prosthetic controller: MIQP+Impedance controller. With the proposed controller, it was shown that the tracking performance has been improved in both simulation [138] and experiment [141] on the robotic platform: AMBER1. In addition, utilizing this novel control method, the robot displays improved stability and robustness to unknown disturbances.

The systematic methodology was then successfully translated to a custom built prosthesis AMPRO1 for achieving both flat-foot level ground walking [144] and stair ascending [145], showing improvements on both tracking and energy efficiency compared to other controllers such as PD. With this framework in hand, the proposed real-time optimization-based controller is then utilized to realize more natural multi-contact prosthetic walking on AMPRO1.

Despite the improvements achieved by the framework of virtual constraints, the current research of virtual constraints based control is still limited with several basic

assumptions: a) a single domain is used for gait design while actual human locomotion is a multi-domain system; b) forward human walking is simplified as a 2D model, i.e., a simple planar model is usually chosen for generating the desired prosthetic trajectory; c) the amputee-prosthesis system is assumed to be symmetric. However, in reality, the amputee side and prosthetic side have the different requirements and model parameters; d) realistic requirements (human comfortability, energy consumption, hardware torque and velocity limitations) of a prosthetic gait have not yet been considered intuitively during the gait design procedure.

Motivated by these open problems, this dissertation takes a further step by considering a 3D and asymmetric amputee-prosthesis model for more realistic multi-contact prosthetic gait design. Additionally, with adapting a computational-efficient direct collocation optimization method, various prosthetic gait design requirements such as "human-likeness" requirements, comfortability requirements and physical related requirements can be imposed directly as explicit nonlinear constraints. The end result of solving this optimization problem is a "proper" 3D human-like prosthetic gait that can be applied to prostheses directly. A 3D capable prosthetic device: AMPRO3 is designed and built from scratch for experiment verification. The final experiment results indicate that the method has a great potential for benefiting amputees in reality.

CHAPTER III

MULTI-DOMAIN OPTIMIZATION

With the goal of achieving human-like locomotion on either bipedal robots or prosthetic devices, we turn to the most prevalent source, the human locomotion system, for inspiration. This chapter begins with analysis of human locomotion by breaking one step into multiple domains based on the contact points (i.e., heel or toe). A multi-domain hybrid system model is constructed to represent the multi-contact human locomotion system in a formal way. With this hybrid system modeling in hand, a multi-domain optimization framework is proposed to design outputs (i.e., virtual constraints) for bipedal robotic systems. Subject to human data based cost, this optimization problem satisfies both partial hybrid zero dynamic constraints and physical constraints, resulting human-like multi-contact gaits that can be analyzed formally and implemented directly.

3.1 Multi-Contact Human Locomotion

During the course of a step, humans undergo changes in phase through changes in their contact points with the environment (heel or toe leaving and striking the ground) as depicted in Figure 5. This multi-domain, or multi-contact nature of the human gait results in walking which is both fluid and efficient [63]. Using the foot push off during the single support phase, a human can lift the swing leg higher, and thus achieve greater foot clearance without bending the swing knee significantly. By having the body pivoting over the the stance toe, much less energy is required for a human to move forward through the utilization of their forward rotational momentum. Researchers also found that the prosthetic foot push off is negatively correlated with leading intact limb loading impulse, which may help reduce knee osteoarthritis in lower extremity amputees [89]. Therefore, incorporating these advantages into bipedal robots or prostheses locomotion in a systematic way is important for both kinetically

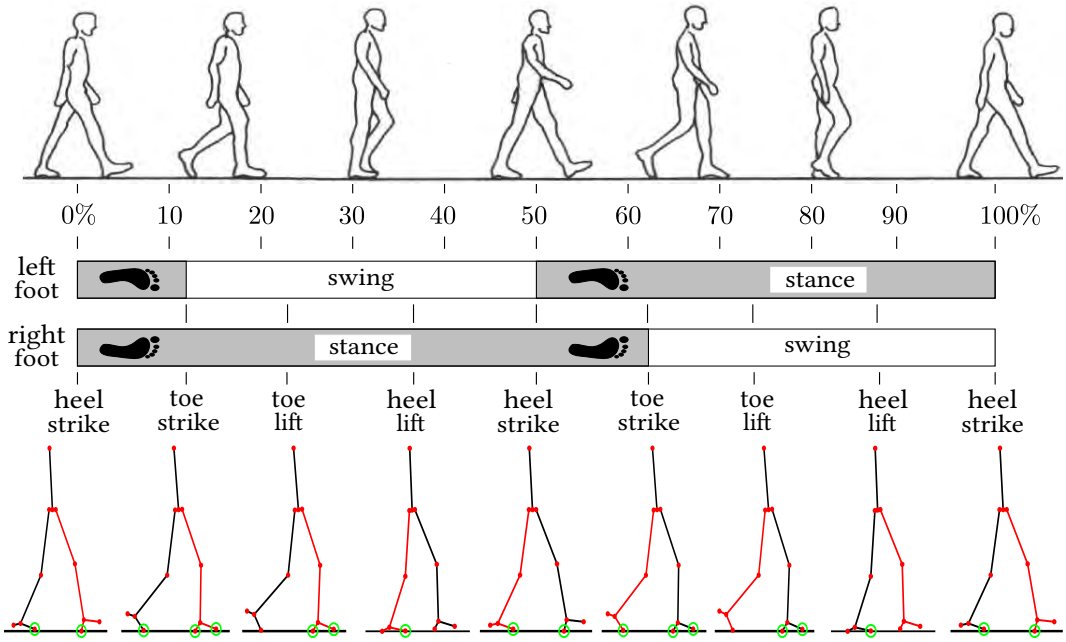

Figure 5: Multi-contact locomotion diagram of a typical human gait cycle [11] (top) and multi-contact domain breakdown of two steps of one subject based on the changes of heel and toe contact condition (bottom). Green circle represents one specific point is in contact with the walking surface.

and kinematically human-like walking.

Understanding this walking pattern of a normal leg is of obvious importance when attempting to reproduce it robotically. Normally, a human gait consists of two phases [40]: stance phase, when the foot is on the ground, and swing phase, when the same foot is in the air. Specifically, sub-phases are usually disintegrated from each phase to describe human locomotion more explicitly. Though different approaches break one step into different phases (for example, in impedance prosthetic control [32], the swing phase is divided into two sub-phases based on the knee angle), we break one step cycle into sub-phases based on the contact points of the heel and toe.

In particular, the human locomotion data capturing experiments were carried out by the motion capture lab in the UC Berkeley with the IRM Protocol $\#2011-04-3088$. Total of nine subjects participated in the experiment. For each subject, data which contained the least noise were used in the computation of kinematic outputs. Here, the noisy data are mainly because of the from time to time dysfunction of the sensors. The process by which the contact point changes of a single step

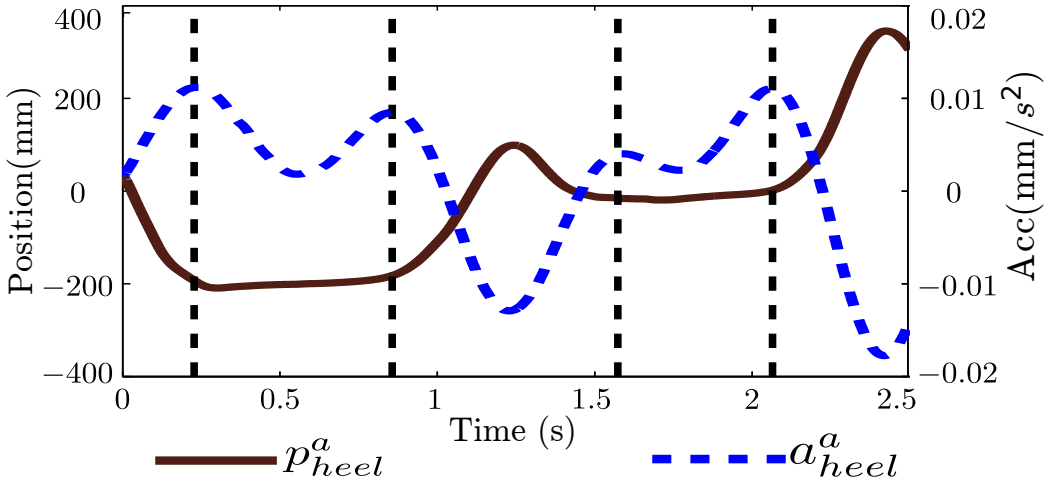

Figure 6: Position and acceleration data of heel of human subject walking up stairs during the motion capture experiment [143].

are determined, is termed the *domain breakdown* procedure. Generally, the domain breakdown is obtained through a position threshold which specifies when the heel or toe is on the ground. Differently, a new method by utilizing the acceleration data—rather than position—of the heel and toe to determine the contact points is proposed in this work. This method is motivated by noting that the time when the contact points (heel or toe) hit or lift the ground is the moment that maximum acceleration occurs. Data of the heel position and acceleration of a test subject during the stair ascending are shown in Figure 6 as an example. The peak accelerations are indicated with dashed vertical lines. The corresponding positions of the heel show the moment of heel strike and lift.

This method is similar to the analysis of ground reaction forces using force plate, which is common in the bio-mechanics community [38], [76]. Utilizing this domain breakdown method (more details can be found in [143]), it is found that human locomotion can be divided into four domains (i.e., sub-phases) in general [21], [143], which are termed based on the switching event of that domain as toe-strike (ts), toe-lift (tl), heel-lift (hl) and heel-strike (hs). The domain breakdown of one subject is plotted in Figure 5 along with the triggering events to show the domain configuration explicitly.

3.2 Hybrid System Model

This section presents the mathematical model of a general multi-domain locomotion bipedal robot systems. In particular, considering the changes of foot contact points over a gait cycle, a multi-domain hybrid system model is developed with both continuous dynamics and discrete dynamics.

3.2.1 Multi-Domain Hybrid System

Multi-domain robotic locomotion can be formally modeled as a hybrid control system [16], [70], [128], which is given by the following tuple:

$$\mathscr{HC} = (\Gamma, D, U, S, \Delta, FG), \tag{1}$$

where

- $\Gamma = (V, E)$ is a *directed circle* graph, with vertices $V = \{v_1, v_2, ..., v_N\}$; and edges $E = \{e_1, e_2, ..., e_N\}$, where N is the number of the total domains. e_i denotes the transition from the current domain to the next domain: $v_i \to v_{i+1}$ if $i < N$ and $v_N \to v_1$ if $i = N$.
- $D = \{D_v\}_{v \in V}$ is a set of *domains of admissibility*, where $D_v \subseteq X \times U$ with $X \subseteq \mathbb{R}^{2n}$ the state space set,
- $U = \{B_v u\}$ is the set of *admissible controls* determined by the controller map B_v which depends on the degree of actuation of the system in domain D_v,
- $S = \{S_e\}_{e \in E}$ is a set of *guards* with $S_e \subseteq D_v$ a proper set,
- $\Delta = \{\Delta_e\}_{e \in E}$ is a set of *reset maps*, where $\Delta_e : X \to X$ is a smooth map,
- $FG = \{(f_v, g_v)\}_{v \in V}$ with (f_v, g_v) a *control system* on D_v, i.e., $\dot{x} = f_v(x) + g_v(x)u$ with $x \in X$, $u \in U$ and $\{x, u\} \in D_v$.

Correspondingly, a *hybrid system* is a hybrid control system with $U = \emptyset$, e.g., after any feedback controllers have been applied, making the system closed-loop. In this case,

$$\mathscr{H} = (\Gamma, D^X, S^X, \Delta, F^X), \tag{2}$$

where $D^X = \{D_v^X\}_{v \in V}$ is the set of domains with $D_v^X \subset X$ being a smooth subset of only X. Similarly, $S^X = \{S_e^X\}_{e \in E}$ is the set of guards with $S_e^X \subseteq D_v^X$, and $F^X = \{f_v^X\}_{v \in V}$ is a set of *dynamical systems* on X, i.e., $\dot{x} = f_v^X(x)$ with $x \in D_v^X$.

3.2.2 Coordinates and Holonomic Constraints

To explicitly construct a hybrid system corresponding to the multi-domain robotic locomotion, basic concepts related to coordinates and constraints are introduced in a general form.

3.2.2.1 General Coordinates

Due to the changes of contact points between the robot and the walking surface throughout the course of a gait, generalized coordinates for the unpinned model are utilized. Specifically, for a serials linkage bipedal robot, the configuration space $\mathcal{Q}$ is represented in the generalized coordinates as $\theta = \{\theta_e, \theta_b\}^T$ with the extended coordinates θ_e representing the positions and rotation angle of the body fixed frame R_b with respect to a fixed inertial frame R_0; and the body coordinates θ_b denoting the relative joint angles (including both revolute and prismatic joints) of the robot. With n denoting the general degrees of freedom of the unconstrained robot, the state space of the model is denoted accordingly as $X := \{x = (\theta; \dot{\theta}) \in T\mathcal{Q}\}$.

3.2.2.2 Holonomic Constraints

With a given vertex $v \in V$, the domain D_v, which describes the admissible configuration of the system, is restricted by the constraints associated with specific contact points interacting with the walking surface. In general, any physical contact of the robot with the external environment introduces a *holonomic constraint*, $\eta_c(\theta)$. Let $\mathcal{C}_v$ be an indexing set of all holonomic constraints defined on D_v, we state the holonomic constraints of the domain as

$$\eta_v = \{\eta_c\}_{c \in \mathcal{C}_v} \equiv \text{constant}, \tag{3}$$

and the associated kinematic constraints as $J_v(\theta)\dot{\theta} = 0$, where $J_v(\theta) = \frac{\partial \eta_v}{\partial \theta}$ is the Jacobian matrix of η_v, i.e., the contact points of a particular domain.

3.2.3 Robot Dynamics

With the generalized coordinates and contact constraints in hand, we are now ready to construct the continuous control system FG for each domain D_v of the hybrid control system $\mathscr{HC}$.

3.2.3.1 Continuous Dynamics

Given the mass and inertia properties of each link of a specific robot (typically obtained via a CAD model or system identification methods), the Lagrangian of a bipedal robot, $\mathcal{L} : T\mathcal{Q} \to \mathbb{R}$, can be stated in the form of the kinetic energy minus the potential energy as:

$$\mathcal{L} = \frac{1}{2}\dot{\theta}^T M(\theta)\dot{\theta} - P(\theta). \tag{4}$$

The continuous dynamics can be constructed using this Euler-Lagrangian equations according to [93]. Holonomic constraints are then added to enforce the contact conditions (additional details can be found in [48]). The end result is a constrained dynamic system:

$$M(\theta)\ddot{\theta} + H(\theta, \dot{\theta}) = B_v u + J_v(\theta)^T F_v(\theta, \dot{\theta}, u), \tag{5}$$

$$J_v(\theta)\ddot{\theta} + \dot{J}_v(\theta)\dot{\theta} = \mathbf{0}, \tag{6}$$

where $M(\theta) \in \mathbb{R}^{n\times n}$ is the inertial matrix, and $H(\theta, \dot{\theta}) = C(\theta, \dot{\theta})\dot{\theta} + G(\theta) \in \mathbb{R}^{n\times 1}$ contains the terms resulting from the centripetal forces, Coriolis effect $C(\theta, \dot{\theta})\dot{\theta}$ and the gravity term $G(\theta)$. $B_v \in \mathbb{R}^{n\times m_r}$ denotes the torque distribution matrix with m_r defined as the number of actuators and $u \in \mathbb{R}^{m_r\times 1}$ is the input torque vector. $F_v(\theta, \dot{\theta}, u)$ is a vector containing a contact wrench for each point on the robot that is in contact with the walking surface. F_v can be explicitly derived from the states $(\theta, \dot{\theta})$ and the controller u by substituting the holonomic constraints in (6) into (5), which yields:

$$F_v(\theta, \dot{\theta}, u) = -(J_v(\theta)M(\theta)^{-1}J_v(\theta)^T)^{-1}(\dot{J}_v(\theta, \dot{\theta})\dot{\theta} + J_v(\theta)M(\theta)^{-1}(B_v u - H(\theta, \dot{\theta}))). \tag{7}$$

Substituting this equation back to (5) allows us to convert the equations of motion to a first order ODE, which yields the affine control system (f_v, g_v) in the following form:

$$\dot{x} = f_v(x) + g_v(x)u \tag{8}$$

where,

$$f_v(x) = \begin{bmatrix} \dot{\theta} \\ M(\theta)^{-1}J_v(J_vM(\theta)^{-1}J_v^T)^{-1}((J_vM(\theta)^{-1} - I)H(\theta,\dot{\theta}) - \dot{J}_v\dot{\theta}) \end{bmatrix},$$
$$g_v(x) = \begin{bmatrix} 0 \\ (I - M(\theta)^{-1}J_v(J_vM(\theta)^{-1}J_v^T)^{-1}J_vM(\theta)^{-1})B_v \end{bmatrix}. \tag{9}$$

3.2.3.2 Domains and Guards.

Due to the presence of impacts and the varying nature of the contact points throughout a gait cycle, we have to carefully consider the modeling of domains D_v and guards S_e for a hybrid system given in (1). Given a vertex $v \in V$, the continuous domain is a set of admissible configurations of the system factoring in both normal reaction forces and a unilateral constraint. Specifically, from the wrench $F_v(\theta, \dot{\theta}, u)$, one can ensure that a particular point on the foot is both in contact with the ground and not slipping by considering inequalities in the form: $R_v^T F_v(\theta, \dot{\theta}, u) \geq 0$ with R_v^T defined as coefficients of the normal reaction forces and the static friction conditions for domain D_v. For example, with only one contact point for a 2D case, R^T can be defined as $[0, 1; -1, \mu]$, where μ is the static friction coefficient (see [107] for more details). The unilateral constraint is another class of constraints that determines the admissible configuration of the system, denoted by $h_v(\theta, \dot{\theta}, u) > 0$. For example, the non-stance foot should always be above the ground during the swing phase. In other words, the height of the non-stance foot should always be positive.

Combining the holonomic constraints $\eta_v(\theta)$ imposed by the contact wrench $F_v(\theta, \dot{\theta}, u)$ and the unilateral constraint $h_v(\theta, \dot{\theta}, u)$, yields the set of admissible configurations on

this domain:

$$\mathcal{A}_v(\theta, \dot{\theta}, u) = \begin{bmatrix} R_v^T F_v(\theta, \dot{\theta}, u) \\ h_v(\theta, \dot{\theta}, u) \end{bmatrix} \geq \mathbf{0}. \tag{10}$$

With this setup, the domains and guards are thus given as:

$$D_v = \{(\theta, \dot{\theta}, u) \in X \times U : \mathcal{A}_v(\theta, \dot{\theta}, u) \geq \mathbf{0}\}, \tag{11}$$

$$S_e = \{(\theta, \dot{\theta}, u) \in X \times U : h_v = 0 \text{ and } \dot{h}_v < 0\}. \tag{12}$$

In particular, the guard is the boundary of this domain with the additional condition that the unilateral constraint is decreasing [128].

3.2.3.3 Discrete Dynamics

Associated with the guard S_e is a reset map Δ_e that maps the current system states (at the moment right before impact, i.e. pre-impact) to the states of the subsequent domain (at the moment of right after impact, i.e., post-impact). In this work, impact reset maps are computed assuming perfectly plastic (i.e., inelastic) impacts, which is a common practice in the bipedal research literature [48], [60], [82]. Specifically, the velocity of the swing foot is assumed to be zero (i.e., no rebound or slipping) after impacts and there is no instantaneous change in the configuration (i.e., no deformation) [60]. Based on these assumption, the impact equations are given by considering the holonomic constraints enforced on the subsequent domain. In particular, the post-impact velocity $\dot{\theta}^+$ can be derived from the pre-impact velocity $\dot{\theta}^-$ via the plastic impact equation:

$$\begin{bmatrix} M(\theta^-) & -J_{v^+}^T(\theta^-) \\ J_{v^+}(\theta^-) & 0 \end{bmatrix} \begin{bmatrix} \dot{\theta}^+ \\ \delta F_v \end{bmatrix} = \begin{bmatrix} M(\theta^-)\dot{\theta}^- \\ 0 \end{bmatrix}, \tag{13}$$

Note that, since $M(\theta)$ is positive definite and J_v is full rank, the matrix on the left-hand side of (13) is invertible. Solving (13) yields,

$$\begin{bmatrix} \dot{\theta}^+ \\ \delta F_v \end{bmatrix} = \begin{bmatrix} \Delta_{\dot{\theta},e}(\theta^-) \\ \Delta_{F_v,e}(\theta^-) \end{bmatrix} \dot{\theta}^- \tag{14}$$

with $\Delta_{F_v,e}(\theta^-) = -(J_v M(\theta^-)^{-1} J_v^T)^{-1}) J_v$ and $\Delta_{\dot{\theta},e}(\theta^-) = M(\theta^-)^{-1} J_v^T \Delta_{F_v,e}(\theta^-) + I$.

As a result of considering "stance" and "non-stance" legs, the re-labeling on the body coordinates must be considered when the stance/non-stance legs switched after one stride. This is a common "trick" in robotic walking which is used to reduce the number of discrete domains. With this notation, the reset map is given by,

$$\Delta_e(\theta^+, \dot{\theta}^+) = \begin{bmatrix} \Delta_{\theta,e}\theta^- \\ \Delta_{\dot{\theta},e}(\theta^-)\dot{\theta}^- \end{bmatrix}. \tag{15}$$

To be more explicit, $\Delta_{\dot{\theta},e} = I_{n\times n}$ for smooth transitions, i.e., transitions without relabeling or impact. For the transition with impact which is also the moment when the relabeling should be considered. More details can be referred to [128], [139].

3.3 Human-Inspired Control

This section extends the traditional framework of the human-inspired control in [15], [16] to the multi-contact case. Virtual constraints are defined in an unified form, based on which, a set of human-inspired controllers is developed explicitly for the purpose of automatic generating multi-domain walking gaits.

3.3.1 Virtual Constraints of Locomotion System

Consider the continuous system with the specific virtual constraints defined on each domain D_v as given by:

$$\begin{aligned} \dot{x} &= f_v(x) + g_v(x)u, \\ y_v &= y_v^a(x) - y_v^d(x), \end{aligned} \tag{16}$$

with y_v the *virtual constraints* for $v \in V$, consisting of the differences between the actual human outputs, $y_v^a(x)$, and the desired value for these outputs, $y_v^d(x)$. The human-inspired control design process consists of determining the proper choice of actual and desired outputs, along with the construction of a control law u that drives $y_v^a(x) \to y_v^d(x)$ such that the resulting hybrid system obtained by applying this control law has a periodic orbit, i.e., a stable walking gait.

3.3.2 Human Locomotion Outputs

Motivated by the goal of achieving human-like robotic walking [21], the actual human outputs are extracted from the human locomotion data to represent the locomotion patterns of a human throughout a step with the goal of control synthesis. In particular, we formally define a human output combination as follows [16]:

Definition 1. *A human output combination for $v \in V$ is a tuple $Y_v^H = (Q, y_{1,v}^H, y_{2,v}^H)$ consisting of a configuration space Q, velocity-modulating outputs $y_{1,v}^H : Q \to \mathbb{R}^{n_{1,v}}$ and position-modulating outputs $y_{2,v}^H : Q \to \mathbb{R}^{m_v - n_{1,v}}$ with $n_{1,v}$ the number of velocity-modulating outputs and m_v the admissible degrees of actuation. Let O_v be an index set for $y_{2,v}^H$ whereby $y_{2,v}^H(\theta) = [y_{2,v}^H(\theta)_o]_{o \in O_v}$.*

A human output combination is *independent* if

$$rank(\begin{bmatrix} y_{1,v}^H(\theta) \\ y_{2,v}^H(\theta) \end{bmatrix}) = m_v, \tag{17}$$

on Q_b; and linear if

$$y_{1,v}^H(\theta) = c_v\theta, \tag{18}$$

$$y_{2,v}^H(\theta) = H_v\theta, \tag{19}$$

for $c_v \in \mathbb{R}^{n_{1,v} \times n}$ and $H_v \in \mathbb{R}^{(m_v - n_{1,v}) \times n}$. Note that this definition is not limited to the human locomotion data, but can also be applied to different types of reference output data. For example, one can consider a SLIP model output combination (see [139] for an example of ATRIAS).

Remark The fundamental idea behind obtaining human-like robotic walking from human walking data is that, rather than looking at the dynamics of the human, we look at outputs of the human that represent the walking behavior. By tracking these actual human locomotion outputs in a robot, through their representation via carefully selected walking functions, the robot will display the same qualitative behavior as the human despite the differences in dynamics. That is, we seek to find a "low-dimensional" representation of human walking, i.e., the desired outputs represented by specific walking functions, which will be discussed in the following section.

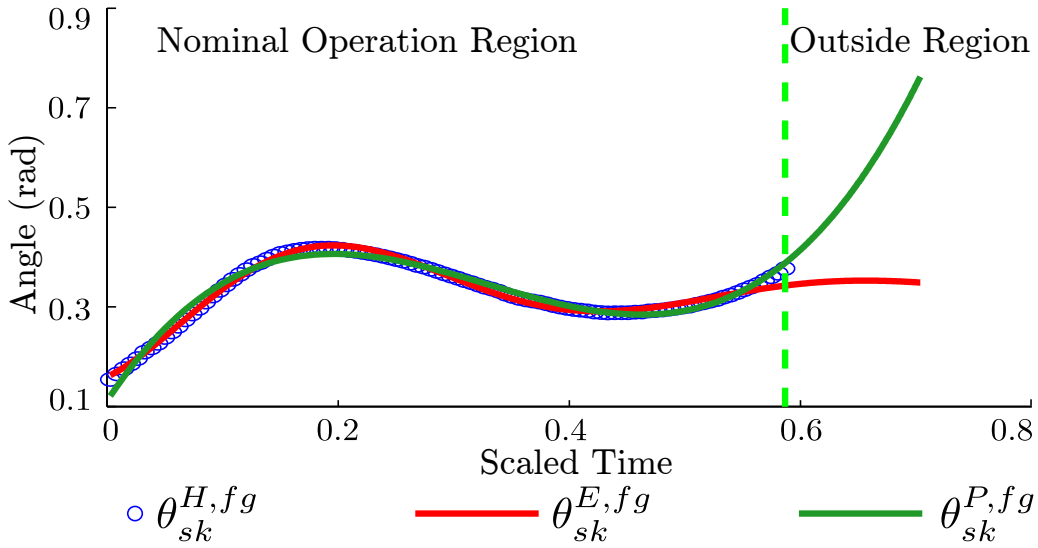

Figure 7: Stance knee angle for flat-ground (fg) locomotion data fit comparison between the CWF and the $4th$ order polynomial function at the outside of the nominal operation region, which is obtained by extending 20% of the nominal operation region. The superscripts H, E, P denote the human data, CWF fitting and polynomial fitting, respectively [143].

3.3.3 Desired Robotic Outputs

With the actual human locomotion outputs in hand, the next step is to search for specific walking functions to characterize the behavior of human locomotion, while with the hope that the fundamental mechanisms underlying human walking can be discovered, simplified and exploited to achieve robust walking in bipedal robots.

3.3.3.1 Extended Canonical Walking Function

Previous work reveal that the actual human outputs considered for various types of locomotion (flat-ground walking [15] and running [146]) can be represented by a simple function characterizing the solution to a linear spring-mass-damper system, which we termed the *canonical walking function* (CWF). That is, the human locomotion system appears to display simple behavior when locomoting in a periodic fashion. In addition, studying human locomotion data for more complex locomotion types, e.g., stair climbing [133] and rough terrain walking [143], the actual human outputs can be characterized by a natural extension to the canonical walking function consisting of a linear mass-spring-damper system subject to sinusoidal excitation.

Note that, there are many other forms of desired walking functions—such as polynomial function and Bézier function—that are used commonly in bipedal researches. Comparing to those polynomial based desired functions, the CWF provides a simpler form (requires fewer parameters) that appears to characterize all the basic human locomotion primitives (walking, stair ascending, stair descending and running [146]). Moreover, another advantage of this approach over other similar methods (for example, a $4th$ order polynomial function used in [34]) is the better behavior of the CWF outside the nominal operation region. As shown in Figure 7, both the CWF (with correlation as 0.9934) and the $4th$ order polynomial function (with the correlation as 0.9875) can fit the human data very well. However, the $4th$ order polynomial function blows up outside the operation window immediately and becomes infeasible while the CWF still remains a reasonable value, which we claim is very important to give the robot more robustness while handling external disturbance. As robot will always miss the designed right time frame in real world due to the environment disturbance and model uncertainty, the behavior outside the nominal region plays a key role to the stability and robustness of the robot.

In this work, it is found that the actual multi-domain human locomotion outputs for a complete step cycle can be characterized by this extended function, which we term the *extended canonical walking function* (ECWF):

$$y_{ecwf}(t) = e^{-\alpha_4 t}\left(\alpha_1 \cos(\alpha_2 t) + \alpha_3 \sin(\alpha_2 t)\right) + \alpha_5 \cos(\alpha_6 t) + \kappa(\alpha)\sin(\alpha_6 t) + \alpha_7, \quad (20)$$

where $\kappa(\alpha) = (2\alpha_4\alpha_5\alpha_6/((\alpha_2)^2 + (\alpha_4)^2 + (\alpha_6)^2)$. Analysis of the possible position-modulating human outputs shows that this function can fit the human locomotion data with high correlation, i.e., multi-domain human locomotion can be accurately represented by this simple function.

3.3.3.2 Parameterization of Time

Noted for the study of human outputs, the linearized forward hip position can be approximated by a linear function of time $\delta p_{hip}(t) = \mathrm{v}_{hip} t$ throughout a single step; therefore, this is chosen to be the desired behavior for the velocity modulating output.

Through this observation, and with the goal of controlling the velocity of the robot, we define the following relative degree one output[1]:

$$y^a_{1,v}(\theta,\dot{\theta}) = \dot{y}^H_{1,v}(\theta,\dot{\theta}) = dy^H_{1,v}(\theta)\dot{\theta}, \quad y^d_{1,v}(\alpha_v) = \mathrm{v}_{hip} \tag{21}$$

with α_v defined as the walking function parameters for domain D_v.

To define the actual and desired outputs for the position modulating outputs, we begin by noting that—due to the linearity of the hip velocity—we can parameterize time in the following fashion:

$$\tau(\theta) = (\delta p_{hip,v}(\theta) - \delta p_{hip}(\theta^0))/\mathrm{v}_{hip}. \tag{22}$$

Compared to the standard tracking control laws in [103] (the end result of which would be a time-based, or non-autonomous, control law), the time parameterization method removes the dependence of time in (20) and yields an autonomous control law. This procedure is common in literature [128], [129], and the parameterization chosen draws inspiration from both those that have been used in the past in the context of bipedal walking and the human data. θ^0 represents the robot configuration at the beginning of one step. Therefore, the desired outputs y^d_2 can be stated as:

$$y^d_{2,v}(\tau(\theta),\alpha_v) := [y_{ecwf}(\tau(\theta),\alpha_v)_o]_{o\in O_v}. \tag{23}$$

Correspondingly, the actual outputs can be obtained through the position-modulating outputs as:

$$y^a_{2,v} = y^H_{2,v}(\theta) = H_v\theta. \tag{24}$$

3.3.3.3 Human-Inspired Virtual Constraints

With the autonomous ECWF in hand, we formally define the human-inspired virtual constraints for a robot as:

$$y_v(\theta,\dot{\theta},\alpha_v) = \begin{bmatrix} y_{1,v}(\theta,\dot{\theta},\alpha_v) \\ y_{2,v}(\theta,\alpha_v) \end{bmatrix} = \begin{bmatrix} y^a_{1,v}(\theta,\dot{\theta}) - y^d_{1,v}(\alpha_v) \\ y^a_{2,v}(\theta) - y^d_{2,v}(\tau(\theta),\alpha_v) \end{bmatrix}, \tag{25}$$

[1]The desired relative degree one output v_{hip} can be viewed as a special case of the ECWF with $\alpha_{1,\ldots,6} = 0$ and $\alpha_7 = v_{hip}$

where $y_{1,v}(\theta, \dot{\theta}, \alpha_v)$ and $y_{2,v}(\theta, \alpha_v)$ are the relative degree one and relative degree two virtual constraints, respectively.

The parameter set α is the grouped parameters of all the outputs consisting of both the relative degree one virtual constraint and relative degree two virtual constraints for a complete step cycle. Particularly, based on the actuation type in each domain v, the corresponding components α_v of α will be utilized to define the human-inspired virtual constraints via (20) and (21). Note that, for a specific virtual constraint, the parameters will be kept unchanged for all the domains during one step cycle, i.e., only one set of parameters α is used to characterize an entire step.

3.3.4 Control Law Construction

The goal of the controller is to drive the outputs of robot to the outputs of human (or other reference trajectories of interest, e.g., SLIP-based trajectories) as represented by the ECWF in each domain. Due to the fact that the dynamics of the robotic systems are highly nonlinear, input-output linearization is a natural choice of control methodology to drive $y_{\alpha_v,v} \to 0$ in an exponential fashion.

3.3.4.1 Input-Output Linearization

In particular, with the affine control system defined in (16) and the human-inspired virtual constraints defined in (25), differentiating the velocity modulating output $y_{1,v}$ once with respect to time yields,

$$\dot{y}_{1,v} = \underbrace{\frac{\partial y_{1,v}}{\partial x} f_v(x)}_{L_{f_v} y_{1,v}} + \underbrace{\frac{\partial y_{1,v}}{\partial x} g_v(x)}_{L_{g_v} y_{1,v}} u, \tag{26}$$

where $L_{f_v} y_{1,v} : \mathbb{R}^n \to \mathbb{R}$ and $L_{g_v} y_{1,v} : \mathbb{R}^n \to \mathbb{R}$ are the *L*ie derivatives of $y_{1,v}$ with respect to f_v and g_v respectively for domain v [103]. If $L_{g_v} y_{1,v}$ is non-zero for all $x \in D_v$, the linearization feedback law can be given by

$$u = \frac{1}{L_{g_v} y}(-L_{f_v} y_{1,v} + \mu), \tag{27}$$

the end result of which is the first-order linear system from the new input μ to the output $y_{1,v}$,

$$\dot{y}_{1,v} = \mu. \tag{28}$$

With this form, different linear control laws can be applied to achieve exponentially convergence.

Due to the second order nature of the position modulating outputs, one have $L_{g_v} y_{2,v} \equiv 0$ for $\forall x \in D_v$. Differentiating $y_{2,v}$ twice computes the accelerations of the position modulating outputs, rendering

$$\begin{aligned} \ddot{y}_{2,v} =& \frac{\partial}{\partial x}\left(\frac{\partial y_{2,v}}{\partial x} f_v(x)\right)(f_v(x) + g_v(x)u) \\ =& \underbrace{\frac{\partial}{\partial x}\left(\frac{\partial y_{2,v}}{\partial x} f_v(x)\right) f_v(x)}_{L_{f_v}^2 y_{2,v}} + \underbrace{\frac{\partial}{\partial x}\left(\frac{\partial y_{2,v}}{\partial x} f_v(x)\right) g_v(x)}_{L_{g_v} L_{f_v} y_{2,v}} u. \end{aligned} \tag{29}$$

Similarly, $L_{f_v}^2 y_{2,v} : \mathbb{R}^n \to \mathbb{R}$ and $L_{g_v} L_{f_v} y_{2,v} : \mathbb{R}^n \to \mathbb{R}$ are the *L*ie derivatives of $y_{2,v}$ with respect to f_v and g_v respectively for domain v [103]. The linearization feedback law can be given accordingly as

$$u = \frac{1}{L_{g_v} L_{f_v} y_{2,v}}(-L_{f_v}^2 y_{2,v} + \mu), \tag{30}$$

which yields the linear form as

$$\ddot{y}_{2,v} = \mu. \tag{31}$$

More generally, the control law can be defined similarly for higher degree outputs. The details can be referred to [103].

3.3.4.2 Human-Inspired Feedback Controller

With the linearization feedback laws defined above, the affine control system (16) with the human-inspired virtual constraints in (25) can be reformulated as:

$$\begin{bmatrix} \dot{y}_{1,v} \\ \ddot{y}_{2,v} \end{bmatrix} = \begin{bmatrix} L_f y_{1,v}(\theta, \dot{\theta}, \alpha_v) \\ L_f^2 y_{2,v}(\theta, \dot{\theta}, \alpha_v) \end{bmatrix} + \begin{bmatrix} L_g y_{1,v}(\theta, \dot{\theta}, \alpha_v) \\ L_g L_f y_{2,v}(\theta, \dot{\theta}, \alpha_v) \end{bmatrix} u. \tag{32}$$

For the domains of fully- and over- actuation, i.e., the admissible degrees of actuation is greater or equal than the unconstrained degrees of freedom, we consider both velocity modulating output and position modulating outputs. Therefore, the human-inspired controller can be defined as:

$$u_v^{\varepsilon}(\theta,\dot{\theta},\alpha_v) = -\Lambda_v^{-1}(\theta,\dot{\theta},\alpha_v)\left(\begin{bmatrix} 0 \\ L_{f_v}^2 y_{2,v}(\theta,\dot{\theta},\alpha_v)\end{bmatrix} + \begin{bmatrix} L_{f_v} y_{1,v}(\theta,\dot{\theta},\alpha_v) \\ 2\frac{1}{\varepsilon} L_{f_v} y_{2,v}(\theta,\dot{\theta},\alpha_v)\end{bmatrix} + \begin{bmatrix} \frac{1}{\varepsilon} y_{1,v}(\theta,\dot{\theta},\alpha_v) \\ \frac{1}{\varepsilon^2} y_{2,v}(\theta,\dot{\theta},\alpha_v)\end{bmatrix}\right). \tag{33}$$

Applying this controller gives us a linear form as:

$$\dot{y}_{1,v} = -\frac{1}{\varepsilon} y_{1,v}(\theta,\dot{\theta},\alpha_v) \tag{34}$$

$$\ddot{y}_{2,v} = -2\frac{1}{\varepsilon} L_{f_v} y_{2,v}(\theta,\dot{\theta},\alpha_v) - \frac{1}{\varepsilon^2} y_{2,v}(\theta,\dot{\theta},\alpha_v), \tag{35}$$

which renders the virtual constraints exponentially stable. $\varepsilon > 0$ is a user defined control gain that determines the convergence rate of $y_v(\theta,\dot{\theta},\alpha_v) \to 0$. The decoupling matrix $\Lambda_v(\theta,\dot{\theta},\alpha_v)$ is given as:

$$\Lambda_v(\theta,\dot{\theta},\alpha_v) = \begin{bmatrix} L_{g_v} y_{1,v}(\theta,\dot{\theta},\alpha_v) \\ L_{g_v} L_{f_v} y_{2,v}(\theta,\dot{\theta},\alpha_v)\end{bmatrix}, \tag{36}$$

which is nonsingular if a linear and independent output combination was chosen.

For the under-actuated domains that with only position modulating outputs, the controller is defined as:

$$u_v^{\varepsilon}(\theta,\dot{\theta},\alpha_v) = -\Lambda_v^{-1}(\theta,\dot{\theta},\alpha_v)\left(L_{f_v}^2 y_{2,v}(\theta,\dot{\theta},\alpha_v) + 2\frac{1}{\varepsilon} L_{f_v} y_{2,v}(\theta,\dot{\theta},\alpha_v) + \frac{1}{\varepsilon^2} y_{2,v}(\theta,\dot{\theta},\alpha_v)\right), \tag{37}$$

with $\Lambda_v(\theta,\dot{\theta},\alpha_v) = L_{g_v} L_{f_v} y_{2,v}(\theta,\dot{\theta},\alpha_v)$, which will be full rank if the outputs were chosen to be mutually exclusive. Applying this controller renders a linear form as defined in (35), which results in exponential convergence of $y_v(\theta,\dot{\theta},\alpha_v) = y_{2,v}(\theta,\alpha_v) \to 0$ for the under-actuated case.

With the human-inspired feedback control laws (33) and (37) in hand, the next step is to find such a parameter set α that a hybrid periodic orbit can be obtained

for the multi-domain locomotion system. Guided by this objective, an optimization framework that yields a qualified parameter set α will be presented in the next section.

3.4 Multi-Domain Optimization

This section focuses on developing of a multi-domain optimization framework that yields the parameter set α which results in stable multi-contact robotic locomotion. Multi-domain *partial hybrid zero dynamics* (PHZD) constraints are introduced to insure the partial zero dynamics are invariant through all the discrete transitions; the end result is a formal guarantee that there is a periodic orbit for the full dimension dynamics given the partial zero dynamics have a stable limit cycle. With the objective function being the least square errors between the robotic outputs and the corresponding outputs computed from human locomotion data, the ultimate goal is to find a parameter set α that yields a multi-domain locomotion gait that is both kinematically human-like and mathematically stable.

3.4.1 Partial Hybrid Zero Dynamics (PHZD)

Before revealing the optimization problem that aims to obtain stable multi-contact walking gaits, it is necessary to introduce several constructions that are fundamental to its formulation.

3.4.1.1 Zero Dynamics

For the general case of under-actuated locomotion, the goal of the human-inspired control laws is to drive the virtual constraints $y(\theta) \to \mathbf{0}$ exponentially. Note that, $y(\theta)$ is a set of general defined virtual constraints that only contains relative degree two outputs. In other words, the control objective is to drive the system dynamics to a parameterized smooth surface exponentially, termed the *zero dynamic surface* $\mathbf{Z}$, which is defined as the following:

$$\mathbf{Z} = \{(\theta, \dot{\theta}) \in X : y(\theta) = \mathbf{0},\ L_f y(\theta, \dot{\theta}) = \mathbf{0}\}. \tag{38}$$

There are several advantages of studying this reduced order (or restricted) dynamics instead of the full order dynamics. For example, the computation time of controller

design, which usually involves with dynamics integration, can be reduced significantly with less degrees of freedom (more details in [53, 128]). In particular, we begin by considering the generalized under-actuated affine control system (16), and it assumes can be represented in the zero dynamics normal form as [103]:

$$\dot{\eta} = b(\eta, \xi) + a(\eta, \xi)u, \tag{39}$$

$$\dot{\xi} = q(\eta, \xi), \tag{40}$$

where η represent the controlled normal states $\eta \in X_c$ and $\xi \in \mathbf{Z}$ are the uncontrolled states for the zero dynamics surface. Note that, we use X_c to represent the controllable substates. The vector fields b, a, and q are assumed to be locally Lipschitz continuous. In addition, we assume that $b(\mathbf{0}, \xi) = \mathbf{0}$, so that the zero dynamics surface $\mathbf{Z}$ (with $y(\theta) = \eta$) defined by $\eta = \mathbf{0}$ with dynamics

$$\dot{\xi} = q(\mathbf{0}, \xi), \tag{41}$$

is invariant [19].

3.4.1.2 Partial Hybrid Zero Dynamics

The above construction is for general under-actuated single-domain systems. Considering the multi-domain hybrid zero dynamics with fully- and over- actuation domains that includes relative degree one virtual constraint, enforcing this invariance through impact is a strong condition that limits the behavior of the robots. Therefore, with a view towards the importance of relative degree two virtual constraints $y_{2,v}(\theta, \alpha_v)$, we consider the zero dynamics by defining $y(\theta) = y_{2,v}(\theta, \alpha_v)$, which we termed the *partial zero dynamics surface*[2]:

$$\mathbf{PZ}_{\alpha_v} = \{(\theta, \dot{\theta}) \in D_v^X : y_{2,v}(\theta, \alpha_v) = \mathbf{0}, L_{f_v} y_{2,v}(\theta, \dot{\theta}, \alpha_v) = \mathbf{0}\}. \tag{42}$$

[2]Note that, the reason we term this dynamics as *partial zero dynamics* is because the real zero dynamics also includes the relative degree one virtual constraint for the fully-actuated (fa) and over-actuated (oa) domains. For the under-actuated (ua) domain that only has relative degree two virtual constraints, the $\mathbf{PZ}_{\alpha_v}$ surface is actually the *full zero dynamic surface*, i.e., $\mathbf{PZ}_{\alpha_{\text{ua}}} := \mathbf{Z}_{ua}$. For notation simplicity, $\mathbf{PZ}_{\alpha_v}$ is adopted for both situations.

Through the exclusion of the relative degree one virtual constraint in the zero dynamics, the partial zero dynamics surface $\mathbf{PZ}_{\alpha_v}$ can be specifically designed such that it is invariant for a hybrid system with multiple domains. In other words, the goal of considering the PHZD is to find the parameter set α to ensure that the original systems remain on the partial zero dynamics surfaces through all of the discrete transitions present in the multi-domain walking. Formally stated, the multi-domain hybrid control system in (1) with the human-inspired controller defined as in (33) and (37), has PHZD if:

$$\Delta_{e_i}(S_{e_i}^X \cap \mathbf{PZ}_{\alpha_{v_i}}) \subset \mathbf{PZ}_{\alpha_{v_{i+1}}}, \tag{43}$$

for each transition $e_i \in E$.

Note that, the formula in (39) and (40) is explicitly defined for domains with under-actuation. For the cases of fully- and over- actuation, the outputs $y_v(\theta, \dot{\theta}, \alpha_v)$ can be separated into relative degree one virtual constraints $y_{1,v}(\theta, \dot{\theta}, \alpha_v)$ and relative degree two virtual constraints $y_{2,v}(\theta, \alpha_v)$. Having the relative degree two virtual constraints converged to $\mathbf{0}$, which is defined as the partial zero dynamics surface, we could explicitly define the relative degree one virtual constraints as ξ_v satisfying (40) with applying a pre-feedback controller. That is to say, because of the full control authority, we could carefully shape the dynamics of relative degree one virtual constraints to the form of (40), which can be reasonably viewed as a "controllable" zero dynamics. This discussion is important because it allows the general construction of the zero dynamics as in (39) and (40) to suit for all domains with different types of actuation. Therefore, this forms the framework for later discussion.

3.4.2 Main Results

With the goal of formally establishing stable bipedal robotic walking, we start with introducing the periodic orbits of the multi-domain hybrid systems as in (2) and the corresponding generalized *Poincaré* return maps. In the context of hybrid systems, we define terms with a focus on periodic orbits and solutions that evolve in a neighborhood of such orbits. In particular, we consider periodic orbits based on the

transverse dynamics (39) and zero dynamics (40). With $D^X = D^X_{v_1} \cup D^X_{v_2} \cdots \cup D^X_{v_N}$, a solution $\varphi^\varepsilon_t(\eta_0, \xi_0)$ of (2) is hybrid periodic if there exists a finite $T > 0$ such that $\varphi^\varepsilon_{t+T}(\eta_0, \xi_0) = \varphi^\varepsilon_t(\eta_0, \xi_0)$ for all $t \in [\, t_0, \infty)$ and initial condition $(\eta_0, \xi_0) \in D^X$. We could also find $(\eta^*, \xi^*) \in S^X$ such that $\varphi^\varepsilon_t(\Delta(\eta^*, \xi^*)) = (\eta^*, \xi^*)$. A set $\mathscr{O} \subset D^X$ is a periodic orbit of (2) if $\mathscr{O} = \{\varphi^\varepsilon_t(\Delta(\eta^*, \xi^*)) \mid 0 \le t \le T\}$ for a hybrid periodic solution φ^ε_t. Similarly, we denote the solution of the zero dynamics $\dot{\xi} = q(\mathbf{0}, \xi)$ by $\varphi^z_t(\xi_0)$ with $\xi_0 \in \mathbf{Z}$. Correspondingly, the periodic orbit of the zero dynamics is denoted as $\mathscr{O}_\mathbf{Z} \subset \mathbf{Z}$.

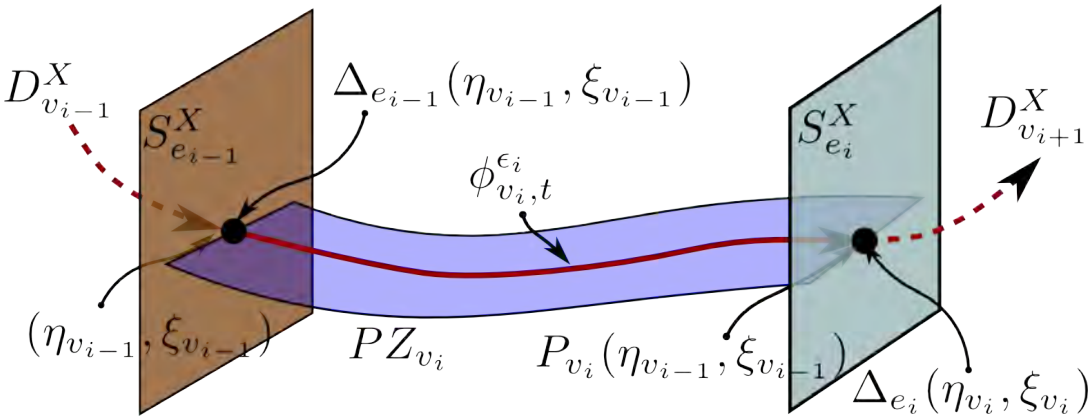

Figure 8: Flow of a domain of a multi-doman hybrid system. $(\eta_{v_{i-1}}, \xi_{v_{i-1}}) \in S^X_{e_{i-1}}$ is the state when the flow of domain v_{i-1} hits the guard $S^X_{e_{i-1}}$. $\Delta_{e_{i-1}}(\eta_{v_{i-1}}, \xi_{v_{i-1}}) \in S^X_{e_{i-1}}$ is the initial condition of domain v_i. $\varphi^{\varepsilon_i}_{v_i,t}$ is the flow of domain v_i on the partial zero dynamics surface PZ_{v_i} and $P^{\varepsilon_i}_{v_i}(\eta_{v_{i-1}}, \xi_{v_{i-1}})$ is the generalized *Poincaré* map when the flow reaches the guard $S^X_{e_i}$.

The *Poincaré* return map [91] is a general mathematical tool for determining the existence and stability properties of periodic orbits for hybrid dynamical systems with impulses. Analogous to the hybrid systems with a single-domain as discussed in [16], we can obtain the generalized *Poincaré* map for domain v_i from one switching surface to anther as $P^{\varepsilon_i}_{v_i} : S^X_{e_{i-1}} \to S^X_{e_i}$, which is a partial function:

$$P^{\varepsilon_i}_{v_i}(\eta_{v_{i-1}}, \xi_{v_{i-1}}) = \varphi^{\varepsilon_i}_{v_i, T^{\varepsilon_i}_{I_{v_i}}}(\Delta_{e_{i-1}}(\eta_{v_{i-1}}, \xi_{v_{i-1}})), \tag{44}$$

where $(\eta_{v_{i-1}}, \xi_{v_{i-1}}) \in S^X_{e_{i-1}}$ and $T^{\varepsilon_i}_{I_{v_i}} : S^X_{e_{i-1}} \to \mathbb{R} > 0$ is the *time-to-impact* function for

domain v_i:

$$T^{\varepsilon_i}_{I_{v_i}}(\eta_{v_{i-1}}, \xi_{v_{i-1}}) := \inf\{t \geq 0 \mid \varphi^{\varepsilon_i}_{v_i,t}(\Delta_{e_{i-1}}(\eta_{v_{i-1}}, \xi_{v_{i-1}})) \in S^X_{e_i}\}, \quad \text{if } \exists\, t \text{ such that } \varphi^{\varepsilon_i}_{v_i,t}(\Delta_{e_{i-1}}(\eta_{v_{i-1}}, \xi_{v_{i-1}})) \in S^X_{e_i}. \tag{45}$$

This time-to-impact function is obtained through the Implicit Function Theorem [103] by considering the function $H_{v_i}(t, \eta_{v_{i-1}}, \xi_{v_{i-1}}) = h_{v_i}(\varphi^{\varepsilon_i}_{v_i,t}(\Delta_{e_{i-1}}(\eta_{v_{i-1}}, \xi_{v_{i-1}})))$ for which $H_{v_i}(t, \eta_{v_{i-1}}, \xi_{v_{i-1}}) = 0$ when $t = T^{\varepsilon_i}_{I_{v_i}}(\eta_{v_{i-1}}, \xi_{v_{i-1}})$. To better illustrate the definition of each term, Figure 8 shows the flow of a domain v_i of the multi-domain system.

In particular, for system (1) with the directed circle graph defined as Γ, the complete *Poincaré* return map can be defined with the composition of generalized *Poincaré* maps for each domain v_i as discussed in [48]:

$$P := P^{\varepsilon_N}_{v_N} \circ \cdots \circ P^{\varepsilon_1}_{v_1}. \tag{46}$$

With multi-domain hybrid system defined in (2) and the definition in (46), P is also the *Poincaré* map for the hybrid system with a single domain[3]:

$$\bar{\mathscr{H}} = (\bar{D}, \bar{S}, \bar{\Delta}, \bar{f}), \tag{47}$$

with $\bar{D} = D^X_{v_1}$, $\bar{f} = f^X_{v_1}$, $\bar{S} = S^X_{e_1}$ and the wrapped reset map

$$\bar{\Delta} = \Delta_{e_N} \circ P^{\varepsilon_N}_{v_N} \circ \cdots \circ P^{\varepsilon_2}_{v_2}. \tag{48}$$

Similarly, the restricted *Poincaré* map for the zero dynamics (as discussed in [19]) can be defined accordingly as $\rho_{v_i} : S^X_{e_{i-1}} \cap \mathbf{Z}_{v_{i-1}} \to S^X_{e_i} \cap \mathbf{Z}_{v_i}$ and more explicitly:

$$\rho_{v_i}(\xi_{v_{i-1}}) = \varphi^z_{v_i, T_{\rho_{v_i}}}(\Delta^z_{e_i}(\xi_{v_{i-1}})), \tag{49}$$

where $\xi_{v_{i-1}} \in S^X_{e_{i-1}} \cap \mathbf{Z}_{v_{i-1}}|_{\mathbf{Z}}$; $\Delta^z_{e_i} = \Delta_{e_i}|_{\mathbf{Z}}$ is the restricted reset map for the zero dynamics and $T_{\rho_{v_i}}$ is the restricted time-to-impact function which can be define similarly as the time-to-impact function (45) of the full dynamics. Particularly, the *Poincaré* return map for the multi-domain zero dynamics can be defined as:

$$\rho := \rho_{v_N} \circ \cdots \circ \rho_{v_1}, \tag{50}$$

[3]Single domain hybrid system can be defined as the multi-domain hybrid system without the graph Γ.

and therefore ρ is also the complete *Poincaré* map for the hybrid zero dynamics system with a single-domain as defined in [19]:

$$\bar{\mathscr{H}}_{\mathbf{Z}} = (\bar{\mathbf{Z}}, \bar{S}^z, \bar{\Delta}^z, \bar{q}), \tag{51}$$

where $\bar{\mathbf{Z}} = \mathbf{Z}_{v_1}$, $\bar{S}^z = S^X_{e_1} \cap \mathbf{Z}_{v_1}$ and $\bar{\Delta}^z = \Delta^z_{e_N} \circ \rho_{v_N} \circ \cdots \circ \rho_{v_2}$, $\bar{q} = q_{v_1}$. Therefore, the invariance of the multi-domain hybrid zero dynamics which is guaranteed by the satisfaction the mutli-domain PHZD constraints as in (43) is equivalent to the invariance of the partial hybrid zero dynamics of single domain as in (51).

It is important to notice that this observation allows the results developed for single-domain models in [19] to be applied to models with multiple domains as in (1). With the assumption that the multi-domain hybrid system is C^1 in each domain and has a transversal periodic orbit $\mathscr{O}$ [48], we know that $\bar{\Delta} = \Delta_{e_N} \circ P^{\varepsilon_N}_{v_N} \circ \cdots \circ P^{\varepsilon_2}_{v_2}$ is Lipschitz in a neighborhood of $(\eta^*, \xi^*) = \mathscr{O} \cap \bar{S}$. Therefore, because of the results in Sect. 4.2.2 of [128] along with the assumption that the periodic orbit $\mathscr{O}$ is transversal, exponential stability of the multi-domain hybrid system can be checked by evaluating eigenvalues of the Jacobian of P at (η^*, ξ^*). Note that, we are assuming that the fixed point is in the one of the switching surface of the multi-domain system. More general definitions can be referred to [48]. Importantly, due to the fact that a periodic orbit for the zero dynamics, $\mathscr{O}_{\mathbf{Z}}$, corresponds to a periodic orbit for the full-order dynamics, $\mathscr{O} = \iota_0(\mathscr{O}_{\mathbf{Z}})$, through the canonical embedding $\iota_0 : \mathbf{Z} \to D^X$ given by $\iota_0(\xi) = (\mathbf{0}, \xi)$, the exponential stability of the full order hybrid system can be guaranteed by the exponential stability of the reduced order hybrid system.

Therefore, the above framework of the reconstructed full- and reduced- order multi-domain hybrid system allow us to formally expand the results from [19] to the multi-domain situation by stating the following theorem:

Main Theorem. *Given the multi-domain hybrid system* (2)*, which can be reconstructed to a single-domain hybrid system as* (47)*, let* $\mathscr{O}_Z$ *be an exponentially stable transverse periodic orbit of the corresponding hybrid zero dynamics system* (51)*, then there exists* $\varepsilon \in (0, 1)$ *such that* $\varepsilon = \min\{\varepsilon_1, \ldots, \varepsilon_N\}$ *with each* ε_i *belonging to the set* $(0, 1)$ *for all the human-inspired controllers in each domain* D_v *as defined in* (33) *and*

(37), $\mathscr{O} = \iota_0(\mathscr{O}_{\mathbf{Z}})$ *is an exponentially stable periodic orbit for the full order dynamics of the multi-domain hybrid system* (1).

Proof of this theory requires several foundation work, which will be introduced in the following chapters. Therefore, we will prove this theory in the Appendix I at the end of this dissertation.

3.4.3 Multi-Domain Optimization

We now have the necessary framework to present an optimization problem with the goal of finding the controller parameter set α, which delivers both human-like and stable multi-domain robotic walking. To achieve the goal of human-like locomotion, reference-data-based cost is adopted as the objective of the optimization problem. Specifically, the objective cost function is sum of the least squares fit errors between the robot outputs and the actual outputs of the reference human walking behavior in each domain, which can be stated as follows:

$$\text{Cost}_{\text{REF}}(\alpha) = \sum_{j \in O_v} \sum_{k=1}^{K_j} \left(y_j^H[k] - y_j^d(t_j^H[k], \alpha) \right)^2, \tag{52}$$

where t_j^H and K_j are the discrete time and the number of discrete points for output $j \in O_v$, respectively.

The optimization problem is subject to two key types of constraints: PHZD constraints that ensure hybrid invariant of the partial zero dynamics through impacts, and physical constraints (such as torque limits and velocity limits) that guarantee the results are practically realizable. Given the cost function and the major constraints, the optimization problem can be stated as:

$$\begin{aligned} \alpha^* = \text{argmin} \ \ & \text{Cost}_{\text{REF}}(\alpha) && \text{(HIO)} \\ \text{s.t} \quad & \Delta_{e_i}(S_{e_i}^X \cap \mathbf{PZ}_{\alpha_{v_i}}) \subset \mathbf{PZ}_{\alpha_{v_{i+1}}} && \text{(PHZD)} \\ & \text{Physical Constraints} && \text{(PHYC)} \end{aligned}$$

which we term the *human-inspired multi-domain optimization* problem due to the human-inspiration for generating the output functions that form the basis of this

optimization. As discussed before, while this optimization problem is inspired by human locomotion (in the selection of outputs), it is not limited to human-locomotion data—nor even dependent on such data. Therefore, the end result of this generalized optimization problem is the control parameter set α that yields formal multi-domain bipedal locomotion while simultaneously guaranteeing that the obtained walking is as close to the reference system as possible. For example, the reference system can be the human locomotion system if the goal is to achieve human-like robotic multi-domain walking [142]; and can also be a SLIP model if we want to achieve SLIP-like multi-domain locomotion [53].

CHAPTER IV

MULTI-CONTACT LOCOMOTION ON AMBER2

With the general multi-domain optimization framework in hand, this chapter will focus on realizing these formal results on an example hardware platform AMBER2 via a novel dynamic trajectory generation strategy. A hybrid system model is constructed specifically for AMBER2. The specific control structure utilized for realizing trajectory tracking on hardware is presented. The end result is experimentally realized stable robotic walking with remarkably human-like multi-contact foot behaviors on AMBER2.

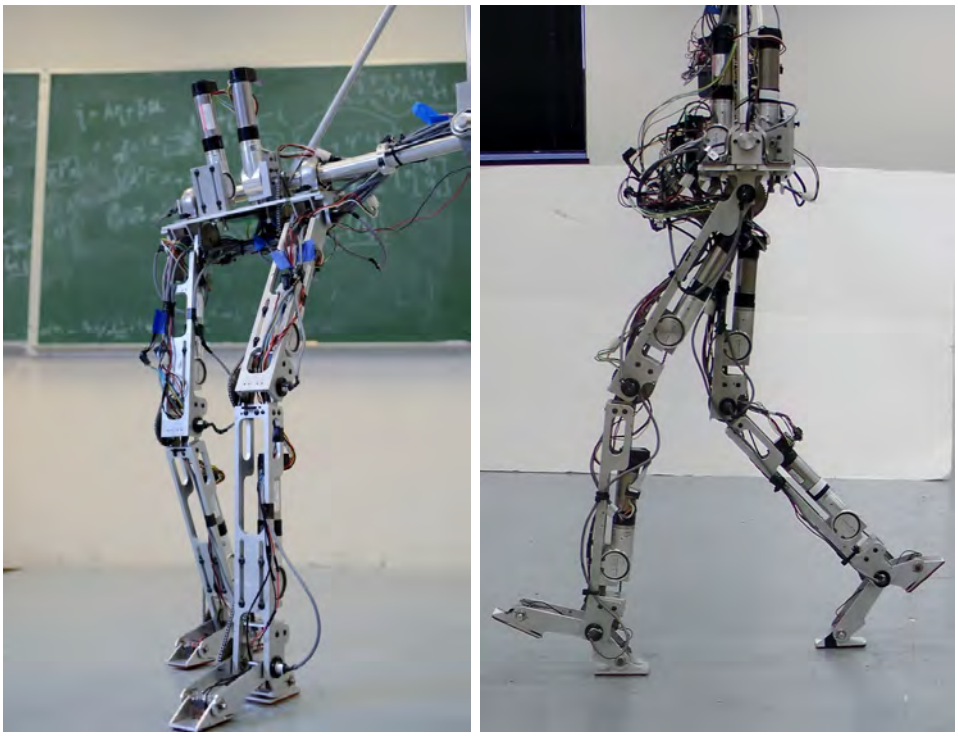

Figure 9: The bipedal robot AMBER2 (left) is constructed with the specific goal of multi-contact locomotion as indicated by the design of the feet (right).

4.1 AMBER2 Model

AMBER2 is a 2D footed bipedal robot with seven links (two calves, two thighs, two feet and a torso, see Figure 9). Six brushless DC motors actuate six joints. The feet of AMBER2 are designed particularly with passive articulated joints aiming to mimic the function of heel and toe ball of human. As a planar robot, the motion of AMBER2 has been restricted to the sagittal plane via a circular boom shown in Figure 10, which is configured as a parallel four-bar linkage such that no support in the sagittal plan is provided by the boom. The boom is fixed rigidly to a low friction rotating mechanism, allowing the biped to walk in a circular fashion. In addition, counterweights are provided on the other end of the pivot point to negate the weight of the boom. The motor H-bridges are located close to the pivot of the boom along with other sensing and controller modules supplied by National Instruments. The modules are remotely connected to the stationary power supply with the help of a slip ring located below the pivot. The joint angles of the robot are measured by PWM absolute MR encoders and single-ended incremental quadrature encoders, and the signal is sent into the FPGA in the controller.

4.1.1 Hybrid System Model

While a general step cycle of human locomotion contains four domains (as discussed in Section 3.1), further analysis shows that the *tl* domain only takes a small portion (about 5%) of the gait (details can be found in [21], [142]). Omission of this phase is reasonable while without sacrificing the ability to capture the essentials of multi-domain human locomotion. Therefore, the multi-contact walking of AMBER2 will focus on the other three domains of a single step as shown in Figure 11. Correspondingly, the hybrid control system can be defined as:

$$\mathscr{HC}_R = (\Gamma_R, D_R, S_R, \Delta_R, FG_R), \tag{53}$$

where the subscript R comes from the last letter of AMBER. The corresponding hybrid system can be defined as:

$$\mathscr{H}_R = (\Gamma_R, D_R^X, S_R^X, \Delta_R, F_R^X). \tag{54}$$

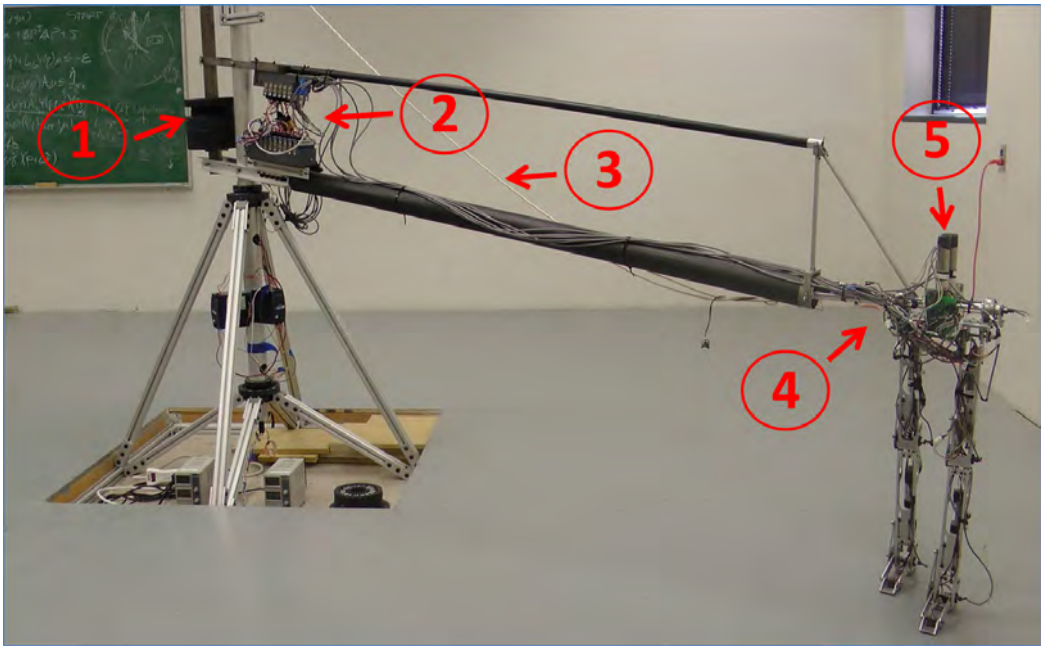

Figure 10: AMBER2 with the boom and electronics. The boom restricts motion to the sagittal plane. As shown in the figure: **(1)** Counterweight used to balance the boom around the pivot, **(2)** Controller module where the walking algorithm is running, **(3)** The boom, **(4)** Boom support structure which keeps the torso horizontal by using a parallel four-bar linkage mechanism, **(5)** The bipedal robot AMBER2.

Motivated by the desire to discuss the multi-contact locomotion of AMBER2 in a more intuitive fashion, we label the domains explicitly based on the major impact[1] in this work. Therefore, for the multi-domain walking gait of AMBER2, the vertices and edges of the directed graph Γ_R are specifically defined as:

$$\begin{aligned} V_R &= \{v^+, v^i, v^-\}, \\ E_R &= \{e^i_+ = (v^+ \to v^i), e^-_i = (v^i \to v^-), e^+_- = (v^- \to v^+)\}. \end{aligned} \tag{55}$$

where $+$, i and $-$ represent post-impact (corresponds to ts domain, which is over-actuated), intermediate (corresponds to hl domain, which is fully-actuated) and pre-impact (corresponds to hs domain, which is under-actuated), respectively. The edges

[1]It is possible that for a particular multi-domain hybrid system, there may be more than one impact. However, it is often the case that certain impact may be considered "soft" impact, thus not imparting a large impulse to the system. Toe strike for example could be considered a soft impact since the toe does not generally impact the ground with a considerable velocity. Heel strike, however, can have a large effect on the system and is not generally ignored. Therefore, it is considered the major impact.

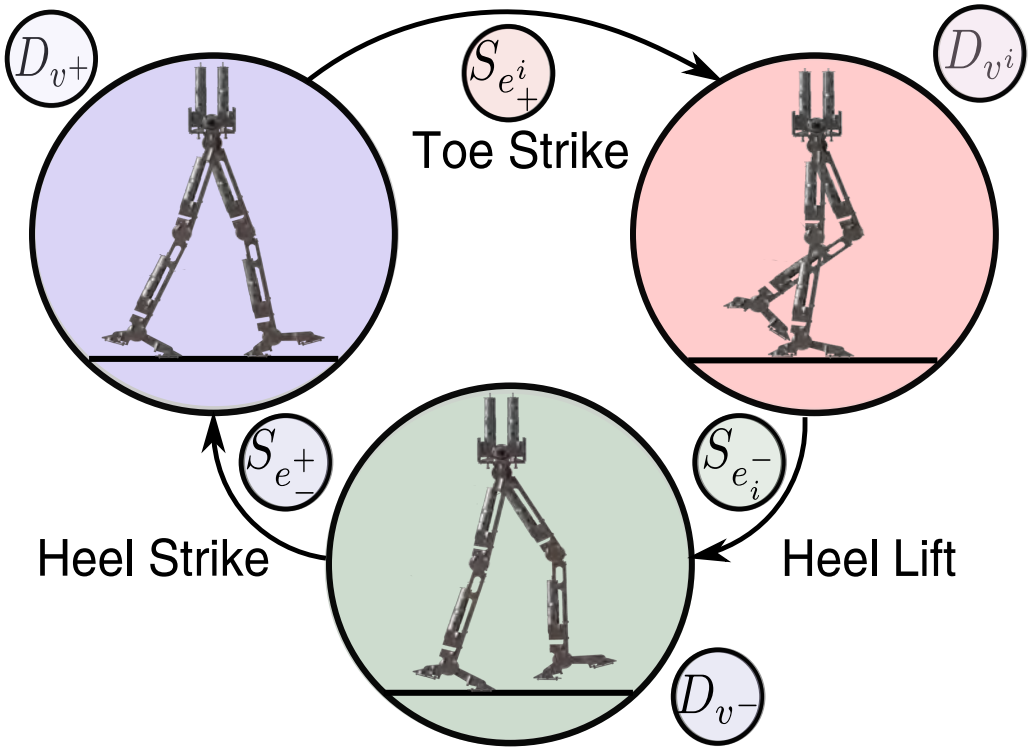

Figure 11: Three-domain graph configuration of the hybrid system of AMBER2.

are defined to be the transitions of interest. For example, edge e^i_+ denotes the transition from the post-impact domain to the intermediate domain.

Note that, the actuation type is defined based on the number of actuators and the number of unconstrained degree of freedoms. For example, during the hs domain, there are 7 unconstrained degree of freedoms which is more than the numbers of actuators, which is 6. Therefore, the hs or v^- domain is under-actuated. Similarly, by definition, the v^i domain is fully-actuated and the v^+ is over-actuated. The actuation types considered for AMBER2 can characterize all the types of actuation present in locomotion (more details can be found in [139]), therefore, the results validated on AMBER2 can also be extended to other types of multi-domain locomotion (e.g. ATRIAS [53]).

4.1.2 Dynamics of AMBER2

For the coordinates of the planar robot AMBER2, the body fixed frame is located at the position of the stance toe. In particular, $\{p_x, p_z\}$ denote the x and z

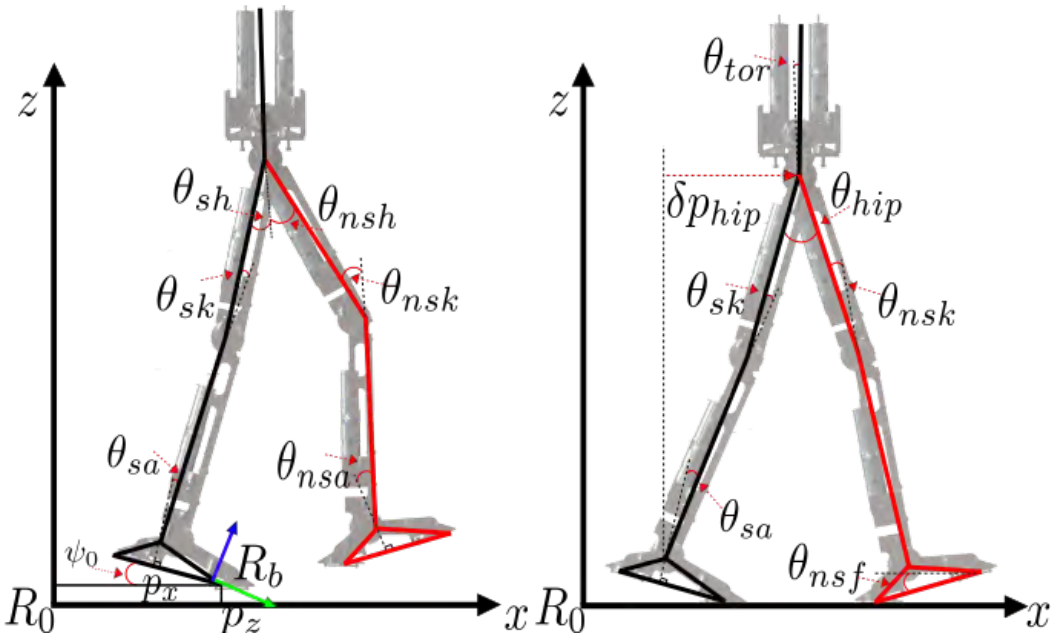

Figure 12: Configuration (left) and outputs (right) of AMBER2 model.

positions of the stance toe w.r.t the ground frame, respectively; φ_0 is the pitch angle measured from the walking surface to the bottom of the foot; the body coordinates $\theta_b = \{\theta_{sa}, \theta_{sk}, \theta_{sh}, \theta_{nsh}, \theta_{nsk}, \theta_{nsa}\}$ are shown in Figure 12. In the context of the multi-domain walking gait of interest as shown in Figure 11, the constraints of each domain of AMBER2 can be defined explicitly as the following:

- For v^+, the unilateral constraint $h_{v^+}(\theta)$ consists of the vertical height of stance toe, while the holonomic constraints $\eta_{v^+}(\theta)$ consists the vertical height of stance heel and swing toe;
- For v^i, the unilateral constraint $h_{v^i}(\theta, \dot{\theta})$ is the vertical reaction force at the stance heel, while the holonomic constraints $\eta_{v^i}(\theta)$ consists the vertical height of stance heel and toe;
- For v^-, the unilateral constraint $h_{v^-}(\theta)$ is the non-stance heel vertical height, while the holonomic constraints $\eta_{v^-}(\theta)$ is the vertical height of stance toe.

With the coordinates and constraints of AMBER2 in hand, the continuous dynamics, domains D_v, guards S_e and reset maps Δ_e for AMBER2 can be configured explicitly according to the general discussion in Section 3.2.

The mathematical model of AMBER2 also contains the motors and the boom. The inertias of these two elements are included in the model differently. Details of this approach are explained in [134]. Since the end of the boom can move vertically and horizontally, it exhibits yaw and roll about the pivot. This would correspond to the x component and z component of the velocities of the torso. The CoM of the boom can be approximated to be at the center of the pivot considering the counterweight mass. With I_{boom} being the inertia of the boom, its mass matrix, $M_{boom} \in \mathbb{R}^{6\times6}$, is:

$$M_{boom} = \begin{bmatrix} \frac{I_{boom}}{L_{boom}^2} & \mathbf{0}_{3\times3} \\ \mathbf{0}_{3\times3} & \mathbf{0}_{3\times3} \end{bmatrix}, \tag{56}$$

where L_{boom} is the distance between CoM of the torso and the pivot.

The new combined mass inertia matrix, M_{com}, used in the lagrangian will be updated as:

$$M_{com}(\theta) = M(\theta) + diag(0, I_{m,sk}, I_{m,sh}, I_{m,nsh}, I_{m,nsk}, I_{m,nsa}) + J(\theta)^T M_{boom} J(\theta), \tag{57}$$

where $I_{m,sk}, I_{m,sh}, I_{m,nsh}, I_{m,nsk}, I_{m,nsa}$ correspond to the motor inertia of respective links and $J(\theta)$ is the body Jacobin of the center of mass of the torso. The measured mass and length parameters of AMBER2 can be found in Table 3.

4.1.3 Virtual Constraints of AMBER2

Investigation of human locomotion data reveals that seven linear independent outputs can be chosen as candidates to characterize the human-like model of AMBER2 [142]: $\delta p_{hip}(\theta)$, the linearized forward position of the hip measured from the stance

Table 1: The mass and length parameters of the AMBER2.

Model Parameters				
Parameter	Mass g	Length m	Inertia x-axis $\times10^3\ g\,mm^2$	Inertia z-axis $\times10^3\ g\,mm^2$
Stance foot	204.42	0.07445	139.698	406.384
Stance calf	1119.43	0.34313	9343.395	22211.105
Stance knee	1172.57	0.29845	9004.044	22404.696
Torso	2154.79	0.10401	20342.192	64678.601
Non-stance knee	1172.57	0.29845	9004.044	22404.696
Non-stance calf	1119.43	0.34313	9343.395	22211.105
Non-stance foot	204.42	0.07445	139.698	406.384

ankle joint; θ_{sa}, the stance ankle angle; θ_{sk}, the stance knee angle; θ_{nsk}, the non-stance knee angle; θ_{hip}, the hip angle between two thighs; $\theta_{tor}(\theta)$, the torso angle measured from the vertical, and $\theta_{nsf}(\theta)$, the angle of the non-stance foot w.r.t the horizontal. These outputs are shown visually in Figure 12.

Specifically, the linearized forward hip position is utilized as the velocity-modulating output and, as in (18), is characterized by c_v:

$$c_v = \begin{bmatrix} 0 & 0 & -L_a - L_c - L_t & -L_c - L_t & -L_t & 0 & 0 & 0 & 0 \end{bmatrix}, \tag{58}$$

where L_a, L_c and L_t are the lengths of ankle, calf and thigh, respectively. Since the pre-impact domain v^- has one degree of under-actuation, only the post-impact and intermediate domain have the velocity-modulating output. The remaining six position-modulating outputs can be written in the matrix form H_{v^-}, as in (19), via:

$$H_{v^-} = \begin{bmatrix} 0 & 0 & 1 & 0 & 0 & 0 & 0 & 0 & 0 \\ 0 & 0 & 0 & 1 & 0 & 0 & 0 & 0 & 0 \\ 0 & 0 & 0 & 0 & 0 & 0 & 0 & 1 & 0 \\ 0 & 0 & 0 & 0 & 0 & 1 & -1 & 0 & 0 \\ 0 & 0 & 1 & 1 & 1 & 1 & 0 & 0 & 0 \\ 0 & 0 & 1 & 1 & 1 & 1 & -1 & -1 & -1 \end{bmatrix}. \tag{59}$$

The motivation for using the notation H_{v^-} is that the position-modulating output combination is also the output combination for the pre-impact (under-actuated) domain for AMBER2, i.e., $O_{v^-} = \{sa, sk, nsk, hip, tor, nsf\}$. Therefore, the notation can be simiplifed. Based on this construction, the position-modulating outputs for the post-impact and intermediate domains are chosen to be sub-matrices of H_{v^-} based upon the admissible degrees of actuation in each of these domains. In particular, $H_{v^+} = (H_{v^-})_{1,2,5,6}$, where we use the notation $(H_{v^-})_i$ to denote the i^{th} row of H_{v^-}. Therefore, the complete outputs set for the post impact domain would be $O_{v^+} = \{\delta p_{hip}, sa, sk, tor, nsf\}$. Similarly, the position modulating outputs for the intermediate domain can be defined as $H_{v^i} = (H_{v^-})_{2-6}$ and the complete set is $O_{v^i} = \{\delta p_{hip}, sk, nsk, hip, tor, nsf\}$.

Correspondingly, for the desired outputs, we use the notation α_{v^-} to represent the generalized position-modulating desired outputs for simplicity. The parameter set can be obtained as $\alpha = \{\mathrm{v}_{hip}, \alpha_{v^-}\} \in \mathbb{R}^{43}$ with $\alpha_{v^-} = \{\alpha_{sa}, \alpha_{sk}, \alpha_{nsk}, \alpha_{hip}, \alpha_{tor}, \alpha_{nsf}\}$. By defining $\alpha_{v_{hip}} = \{\mathrm{v}_{hip}, 0, 0, 0, 0, 0, 0\} \in \mathbb{R}^7$, the vector components of α can be stacked in matrix form with $\alpha \in \mathbb{R}^{7\times 7}$. Because the actuation type in each domain is different, the parameter set matrix for specific domain will be the sub-row matrices of α. In particular, $\alpha_{v^+} = \alpha([1-3, 6, 7], :)$, $\alpha_{v^i} = \alpha([1, 3-7], :)$ and $\alpha_{v^-} = \alpha([2-7], :)$.

By choosing the linearized forward hip velocity $\delta\dot{p}_{hip} = c_v\dot{\theta}$ as the velocity-modulating output, the relative degree one virtual constraints can be easily defined as $y_{1,v} = c_v\dot{\theta} - v_{hip}$. With the definition of both the actual human outputs and the desired robotic outputs, the generalized position-modulating virtual constraints can be defined explicitly as:

$$y_{2,v^-}(\theta, \alpha_{v^-}) = y^a_{2,v^-}(\theta) - y^d_{2,v^-}(\tau(\theta), \alpha_{v^-}) \tag{60}$$

with $y^a_{2,v^-}(\theta) = H_{v^-}\theta$ and $y^d_{2,v^-} = [y_{ecwf}(\tau(\theta), \alpha_{v^-})_o]_{o\in O_{v^-}}$.

With the human-inspired virtual constraints defined above, the human-inspired controllers can be constructed according to (33) for the post-impact and intermediate domains and (37) for the pre-impact domain.

4.2 Multi-Domain Optimization for AMBER2

With the goal to explicitly state the PHZD constraints for optimization solving, some foundation work has to be laid out first. The hybrid zero dynamics for AMBER2 is constructed as the following.

4.2.1 PHZD Reconstruction

With the formal constructions of PHZD constraints in Chapter 3, the goal of this section is to restate the PHZD constraints in a way that can be solved numerically in an optimization problem for AMMBER2. This is done via the PHZD reconstruction methodology. With the assumption that the system evolves on the PHZD surface, a low dimensional representation of the system can be obtained by defining the partial

hybrid zero dynamics coordinates for fully- or over- actuated domains:

$$\begin{aligned}\xi_{1,v} &= \delta p_{hip}(\theta) := c_v\theta, \\ \xi_{2,v} &= y^a_{1,v}(\theta,\dot{\theta}) := \delta \dot{p}_{hip}(\theta) := c_v\dot{\theta}.\end{aligned} \tag{61}$$

With this choice of zero dynamics coordinates, and due to the fact that the system is fully controllable, the dynamics of this surface can be shaped explicitly according to the control purpose. Therefore, the partial zero dynamics can be designed to evolve according to the following linear system:

$$\begin{aligned}\dot{\xi}_{1,v} &= \xi_{2,v}, \\ \dot{\xi}_{2,v} &= -\varepsilon(\xi_{2,v} - v_{hip}).\end{aligned} \tag{62}$$

In addition, with the fact that the desired position modulating outputs $y^d_{2,v}$ is a function of the parameterized time $\tau(\theta)$ as shown in (22), $y^d_{2,v}$ is also a function of $\xi_{1,v}$. Therefore, utilizing $\xi_{1,v}$, $\xi_{2,v}$ and the fact that on the partial zero dynamics surface we have $y^H_{2,v}(\theta) = y^d_{2,v}(\xi_{1,v},\alpha_v)$ and $\partial y^H_{2,v}(\theta)/\partial\theta\dot{\theta} = \partial y^d_{2,v}(\xi_{1,v},\alpha_v)/\partial\xi_{1,v}\xi_{2,v}$, one can obtain:

$$\begin{aligned}\begin{bmatrix} c_v \\ H_v \end{bmatrix}\theta &= \begin{bmatrix} \xi_{1,v} \\ y^d_{2,v}(\xi_{1,v},\alpha_v) \end{bmatrix} \\ \begin{bmatrix} c_v \\ H_v \end{bmatrix}\dot{\theta} &= \begin{bmatrix} \xi_{2,v} \\ \frac{\partial y^d_{2,v}(\xi_{1,v},\alpha_v)}{\partial\xi_{1,v}}\xi_{2,v} \end{bmatrix}.\end{aligned} \tag{63}$$

As a result, we can explicitly, and in closed form, reconstruct the full order state of the robot through the formula:

$$\begin{aligned}\theta = \Psi(\xi_{1,v},\alpha_v) &= \begin{bmatrix} c_v \\ H_v \end{bmatrix}^{-1}\begin{pmatrix} \xi_{1,v} \\ y^d_{2,v}(\xi_{1,v},\alpha_v) \end{pmatrix}, \\ \dot{\theta} = \Phi(\xi_{1,v},\xi_{2,v},\alpha_v) &= \begin{bmatrix} c_v \\ H_v \end{bmatrix}^{-1}\begin{bmatrix} \xi_{2,v} \\ \frac{\partial y^d_{2,v}(\xi_{1,v},\alpha_v)}{\partial\xi_{1,v}}\xi_{2,v} \end{bmatrix}.\end{aligned} \tag{64}$$

Note that, the explicit coordinates in (61) and the linear ODE in (62) for the partial hybrid zero dynamics are valid for over-[2] and fully-actuated domains only. For

[2]For the over-actuated domain, the PHZD reconstruction only yields directly controlled states. The rest states will be computed through geometry constraints in closed form [142].

the under-actuated domain, numerical integration of the zero dynamics is required to obtain the zero dynamics states, which will be then utilized with (64) for the reconstruction of the full-order joint state (as outlined in [15, 128]).

4.2.2 Multi-Domain Optimization

With the PHZD reconstruction in hand, this section discusses the detailed construction of the PHZD constraints for the multi-domain optimization of AMBER2.

4.2.2.1 Intermediate to Pre-Impact Constraints

In order to re-frame the PHZD constraints in a way such that the optimization problem can be numerically approached, we use the PHZD reconstruction strategy to construct a point $(\upsilon, \dot{\upsilon}) \in \mathbf{PZ}_{v^i} \cap S^X_{e^i_-}$, and due to the full control authority, we know that $\xi_{2,v^i} = v_{hip}$. Next, we add an additional parameter by defining $\xi_{1,v^i} = \alpha^{v^i}_{p_{hip}}$ to obtain the hip position ξ_{1,v^i}. Therefore, we expand our set of parameters by defining: $\beta_{v^i} = \{\alpha^{v^i}_{p_{hip}}, \alpha_{v^i}\}$. By doing so, we can explicitly solve the point $(\upsilon(\beta_{v^i}), \dot{\upsilon}(\beta_{v^i}))$ as $\upsilon(\beta_{v^i}) = \Psi(\alpha^{v^i}_{p_{hip}}, \alpha_{v^i})$ and $\dot{\upsilon}(\beta_{v^i}) = \Phi(\alpha^{v^i}_{p_{hip}}, v_{hip}, \alpha_{v^i}))$.

With this construction, we can specifically impose the constraint of domain v^i, which indicates that the reaction force on the heel has to cross zero,

$$h_{v^i}(\upsilon(\beta_{v^i}), \dot{\upsilon}(\beta_{v^i}) = 0. \tag{RC1}$$

Note that, the intermediate domain v^i will switch to the pre-impact domain v^- smoothly without requiring any further constraints except the guard condition. This is the benefit of using only one ECWF through all three domains. Particularly, with the addition parameter $\alpha^{v^i}_{p_{hip}}$, the time of the switch moment $S^X_{e^i_-}$ can also be optimized.

4.2.2.2 Pre-Impact to Post-Impact Constraints

The constructed point $(\upsilon(\beta_{v^i}), \dot{\upsilon}(\beta_{v^i})) \in \mathbf{PZ}_{v^i} \cap S^X_{e^i_-}$ above is also the initial point of domain v^- due to the fact $\Delta_{e^i_-} = I$, i.e., the reset map of this transition is identity. With φ^{v^-} denoting the solution of the vector (f_{v^-}, g_{v^-}), we can define the following

point:

$$(\varphi(\beta_{v^i}), \dot{\varphi}(\beta_{v^i})) = \varphi^{v^-}_{T_{v^-}(\upsilon(\beta_{v^i}),\dot{\upsilon}(\beta_{v^i}))}(\upsilon(\beta_{v^i}), \dot{\upsilon}(\beta_{v^i})). \tag{65}$$

Clearly, $(\varphi(\beta_{v^i}), \dot{\varphi}(\beta_{v^i})) \in S^X_{e^-_+}$. In order to satisfy the PHZD constraints, the post impact state of $(\varphi(\beta_{v^i}), \dot{\varphi}(\beta_{v^i}))$ has to be on the surface of $\mathbf{PZ}_{v^+}$, which implies the following constraints:

$$y_{2,v^+}(\Delta_{\theta,e^-_+}\varphi(\beta_{v^i})) = 0, \tag{RC2}$$

$$dy_{2,v^+}(\Delta_{\theta,e^-_+}\varphi(\beta_{v^i}))\Delta_{\dot{\theta},e^-_+}\dot{\varphi}(\beta_{v^i}) = 0, \tag{RC3}$$

$$\frac{\partial h_{v^-}(\varphi(\beta_{v^i}))}{\partial \varphi(\beta_{v^i})}\dot{\varphi}(\beta_{v^i}) < 0, \tag{RC4}$$

where constraint (RC4) implies that the impact is transverse to the guard [15].

4.2.2.3 Post-impact to Intermediate Constraints

Analogous to the PHZD reconstruction at the end of domain v^i, we seek to construct a point $(\upsilon, \dot{\upsilon}) \in \mathbf{PZ}_{v^+} \cap S^X_{e^i_+}$ with an additional parameter $\alpha^{v^+}_{p_{hip}}$ denoting the hip position at the end of domain v^+. Note that, with the assumption that the controller gain ε is large enough to drive the actual hip velocity to the desired value with sufficient speed (before the end of domain v^+), we have $\xi_{2,v^+} = v_{hip}$. Therefore, by defining the extended parameter set to be $\beta_{v^+} = \{\alpha^{v^+}_{p_{hip}}, \alpha_{v^+}\}$, we can solve for this point as $\upsilon(\beta_{v^+}) = \Psi(\alpha^{v^+}_{p_{hip}}, \alpha_{v^+})$ and $\dot{\upsilon}(\beta_{v^+}) = \Phi(\alpha^{v^+}_{p_{hip}}, v_{hip}, \alpha_{v^+}))$.

Finally, we can explicitly compute the point at the beginning of the domain v^i using the reset map $\Delta_{e^i_+}$ with $\Delta_{\theta,e^i_+} = I$ and $\Delta_{\dot{\theta},e^i_+}$ as discussed in (15). Thence, the specific constraints for the minor impact transition can be stated as follows:

$$y_{\{hip,tor\},v^i}(\upsilon(\beta_{v^i})) = 0, \tag{RC5}$$

$$|dy_{2,v^i}(\upsilon(\beta_{v^+}))\Delta_{\dot{\theta},e^i_+}\dot{\upsilon}(\beta_{v^+})| < \sigma, \tag{RC6}$$

$$\frac{\partial h_{v^+}(\upsilon(\beta_{v^+}))}{\partial \upsilon(\beta_{v^+})}\dot{\upsilon}(\beta_{v^+}) < 0, \tag{RC7}$$

where (RC7) implies that the impact is transverse to the guard. The constant σ is a small positive user-defined value, which is chosen to be 0.1 in our application. Note

that, since only one ECWF has been utilized to characterize the outputs of a whole gait cycle, the PHZD surface can not be fully guaranteed throughout the whole step, which contains three domains and two impacts. Therefore, the PHZD constraints for the switch between the post-impact domain v^+ and the intermediate domain v^i have to be relaxed by only constraining the positions of the outputs, i.e., the states are allowed to be off the PHZD surface for a small moment right after the minor impact. Therefore, the constraints (RC6) make sure that the velocity changes due to the minor impact of the toe strike are smaller than a specific value. As a result, the system will not be thrown off the PHZD surface too much and will converge back to the surface sufficiently quick. In particular, since the shared position modulating outputs between domain v^+ and v^i will be continuous by construction due to the identity position reset map, constraints (RC5) enforce that the outputs y_{hip,v^+} and y_{tor,v^+} which are not tracked during the domain v^+ should be on the surface of $\mathbf{PZ}_{v^i}$.

4.2.2.4 Physical Constraints

Despite the PHZD constraints which insure a stable periodic orbit for the considered hybrid system [15], we also consider several physical constraints such that the results of the optimization are in a form that can be implemented on the physical robots directly. In particular, the following two types of physical constraint are considered:

Torque Constraints. Torques acting on the joints are limited by the capacity of the motors and the motion control modules. Therefore, the optimized gait has to respect the hardware torque bounds, which is stated as:

$$\max_{0\leq\tau(\theta(\beta))} ||u(\theta(\beta),\dot{\theta}(\beta),\varepsilon)|| \leq MAX_{torque}, \tag{RC8}$$

where $\beta=\{\alpha_{p_{hip}}^{v^+},\alpha_{p_{hip}}^{v^i},\alpha\}$ is the final expanded parameter set.

Foot Scuffing Conditions. The swing height clearance of toe and heel, and stride length during the swing phase must be sufficient to avoid scuffing amidst sensor noise, tracking error, uneven ground and even imperfections in the mechanical design. Therefore, foot scuffing conditions must be imposed to insure sustainable walking.

Explicitly, we define:

$$\begin{aligned}
&\max_{0\leq\tau(\theta(\beta))}(h_{nst}(\theta(\beta)) - h_{quad}(\theta(\beta), hmax)) > 0,\\
&\max_{0\leq\tau(\theta(\beta))}(h_{nsh}(\theta(\beta)) - h_{quad}(\theta(\beta), hmax)) > 0,\\
&\max_{0\leq\tau(\theta(\beta))} l_{nsf}(\theta(\beta)) - MIN_{steplength} > 0, \qquad \text{(RC9-11)}
\end{aligned}$$

where h_{quad} is a quadratic polynomial above which the height of non-stance toe (h_{nst}) and heel (h_{nsh}) must remain during the course of a step. The stride length l_{nsf} is constrained to be greater than a minimum specified stride length, $MIN_{steplength}$.

4.2.2.5 Main Results

Utilizing all of the formal constructions above, together with the constraints needed for practical implementation, the final multi-domain optimization problem for AMBER2 can be stated as:

$$\begin{aligned}
\beta^* = \underset{\beta\in\mathbb{R}^{45}}{\text{argmin}}\ & \text{Cost}_{\text{HD}}(\beta) && \text{(HIO)}\\
\text{s.t}\quad & \text{PHZD}\quad \text{Constraints} && \text{(RC1-7)}\\
& \text{Physical}\quad \text{Constraints} && \text{(RC8-11)}
\end{aligned}$$

where the human-data-based cost is defined as:

$$\text{Cost}_{\text{HD}}(\beta) = \sum_{i\in O_v}\sum_{k=1}^{K_i}\left(y_i^H[k] - y_i^d(t_i^H[k], \beta_i)\right)^2, \qquad (66)$$

with t_i^H and K_i being the discrete time and the number of discrete points for output $i \in O_v$, respectively. By solving this optimization problem using the MATLAB built-in function $fmincon$, we can obtain the optimized β^* parameters that best fit human-walking data while enforcing the desired constraints to achieve stable multi-domain robotic walking.

More importantly, motivated by the fact that the multi-domain locomotion of AMBER2 consists one domain that is fully-actuated, this allows one to construct an equivalent single-domain hybrid system around this fully-actuated intermediate

domain D_{R,v^i} as:

$$\bar{\mathscr{H}}_R = (\bar{D}_R, \bar{S}_R, \bar{\Delta}_R, \bar{f}_R), \tag{67}$$

where $\bar{D}_R = D_{R,v^i}$, $\bar{f}_R = f^X_{R,v^i}$, $\bar{S}_R = S^X_{R,e_i^-}$ and $\bar{\Delta}_R = \Delta_{R,e_+^i} \circ P_{R,v^+} \circ P_{R,v^-}$. Combining the *Theorem 1* and the results from [16], we propose the following corollary to show that satisfying the PHZD constraints yields formally provable stable gait for AMBER2.

Corollary 1. *Given the hybrid system* (53) *which can be reconstructed to a single-domain hybrid system as* (67)*, let* β^* *be the parameters that satisfy the PHZD constraints as in* (43)*, then there exists* $\varepsilon \in (0,1)$ *such that* $\varepsilon = \min\{\varepsilon_1, \varepsilon_2, \varepsilon_3\}$ *with each* ε_i *belonging to the set* $(0,1)$ *for all the human-inspired controllers in each domain* $D_{R,v}$ *as defined in* (33) *and* (37)*, the multi-domain hybrid system has an exponential stable periodic orbit,* $\mathscr{O}_\varepsilon$*, which depends on* ε*.*

According to the *Theorem 1* in [16], constraints RC2-4 guarantee that the system is invariant in the partial hybrid zero dynamics through the major impact, i.e., the heel strike. Another important fact of satisfying constraints RC2-4 is that we are able to make sure that under-actuated domain can complete one step by using the numerical integration through the course of under-actuated domain. More importantly, benefited from the fact that only one ECWF is used for the whole step cycle, the system is thus invariant through the rest domain transitions. In particular, for AMBER2 walking with an extra small toe impact, constraints RC5-7 indicate that this impact is minor and transversal, insuring the system converges back to the partial hybrid system sufficiently quick. Therefore, with the folded one domain construction of AMBER2, we have $\Delta(S^X \cap \mathbf{PZ}_\beta) \subset \mathbf{PZ}_\beta$ with $\mathbf{PZ}_\beta$ being the partial hybrid zero dynamics of domain $D^X_{v^i}$. According to the *Theorem 2* in [16], the hybrid system (53) has an exponentially stable periodic.

4.3 Trajectory Reconstruction

With the parameters of human-inspired virtual constraints obtained from the optimization problem, this section will utilize the PHZD reconstruction methodology

for computing the desired joint trajectory for the purpose of tracking on the physical robot AMBER2.

As discussed above, in order to obtain the desired trajectories $(\theta_d, \dot{\theta}_d)$ for AMBER2, both $\xi_{1,v}$ and $\xi_{2,v}$ for each domain must be computed based on the current state. However, as the velocity term $\xi_{2,v}$ is associated with multiple encoders, the actual $\xi_{2,v}$ will accumulate the signal errors of all its contributing encoders. The end result will be inaccurate velocity data. To bypass this shortcoming, we solve the ODE shown in (62) explicitly as follows:

$$\xi_1(t) = v^*_{hip} t + \frac{(1 - \exp(-\varepsilon t))}{\varepsilon}(v^0_{hip} - v^*_{hip}) + \delta p^0_{hip}, \tag{68}$$

$$\xi_2(t) = v^*_{hip} + \exp(-\varepsilon t)(v^0_{hip} - v^*_{hip}), \tag{69}$$

where δp^0_{hip} and v^0_{hip} are the initial hip position and hip velocity at the beginning of the step; v^*_{hip} is the optimized desired hip velocity.

Instead of using time t, we replace it with the parameterized time $\tau(\theta)$ to achieve state based tracking. The more detailed implementation on the physical robot will be discussed later with pseudo code. Note that, even though the velocity modulating output is not tracked in the under-actuated domain, the use of this method is reasonable to achieve an approximation of the desired trajectory considering the short duration of the domain[3]. For the other two domains v^+ and v^i, the desired trajectory are computed with minor modifications.

4.3.1 Post-Impact Domain

As the post-impact domain is over-actuated, AMBER2 has 5 DOF but is actuated with 6 independent motors. In simulation, the redundant actuation is constrained by the holonomic constraints. This technique, however, is not applicable for a physical robot using pure PD control. Therefore, instead of using all of the angles computed from (64) directly, a geometric constraint is applied to update the redundant joint angle. By tracking the updated desired trajectory, both the stance heel and swing

[3]The reason is that the ankle joint motor can not provide enough torque (hardware limitations) in the under-actuated domain to rotate the weight of the robot around the pivot point at the toe.

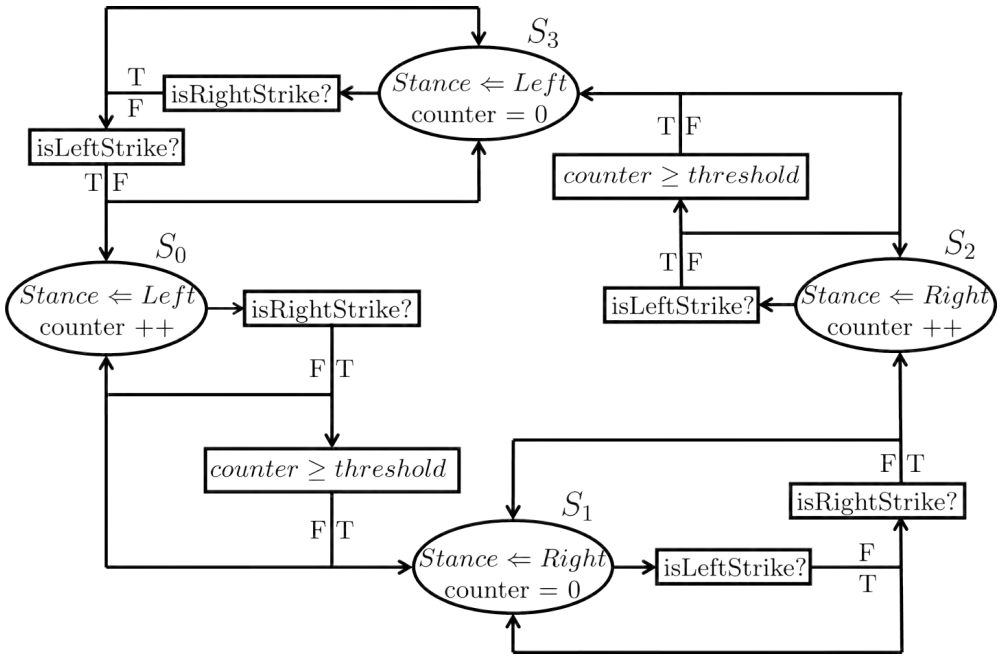

Figure 13: State machine showing the foot contact logic used to determine the stance leg.

toe will remain on the ground, therefore satisfying the holonomic constraints.

4.3.2 Intermediate Domain

With the intermediate domain being fully-actuated, all the extended coordinates should be **0** with the stance foot being flat on the ground throughout the domain. More importantly, the output θ_{sa} is not tracked. Therefore, the linear form of the outputs can be reformulated as:

$$c_{v_i} = \begin{bmatrix} -(L_c + L_t) & -L_t & 0 & 0 & 0 & 0 \end{bmatrix}, \quad H_{v_i} = \begin{bmatrix} 0 & 1 & 0 & 0 & 0 & 0 \\ 0 & 0 & 0 & 0 & 1 & 0 \\ 0 & 0 & 1 & -1 & 0 & 0 \\ 1 & 1 & 1 & 0 & 0 & 0 \\ 1 & 1 & 1 & -1 & -1 & -1 \end{bmatrix}.$$

With this modification, the ψ_0 term has been removed from the output matrix and only the body coordinates θ_b are considered. Note that, removal of the output θ_{sa} allows us to eliminate the control's redundancy.

4.4 Experiment Implementation

To realize real world walking on the physical robot AMBER2, Lab-View2011 is used as the integrated development environment (IDE) to develop the code and control the robot. The controller for AMBER2 has two levels: high-level controller, which is realized by Real-Time (RT) module, and low-level controller realized by Field-Programmable Gate Array (FPGA). The objective of this section is to introduce the control scheme of AMBER2 and its realization in experiments.

4.4.1 Control Architecture

4.4.1.1 High-Level Controller

The Real Time high-level control is in charge of the following major functionalities incorporated as:

1. Interface with FPGA, including: read joint angles and angular velocities, send torque command to low level controller, enable/disable motors.
2. Compute the time parameter τ, determine current system domain.
3. PHZD reconstructon and geometric reconstructon to find desired joint angles.
4. Compute torque command by applying PD control law to corresponding motors, which is fed into the FPGA.

Note that for AMBER2, the sample rate and command rate are both 200Hz. The high level controller is coded into shared libraries to interface in C++ to improve the efficiency of execution. The NI9144 EhterCAT Slave chassis is connected to the cRIO to increase the capacity. For this configuration, each chassis is in charge of one leg. The pseudo-code running in RT is shown in Algorithm 1.

4.4.1.2 Low-Level Controller

The low-level controller is coded to the FPGA with on board clock running at 40MHz, which serves the following major functionalities:

Algorithm 1 Real Time Module

Input: AMBER2 Parameters: Calf Length(L_c), Thigh Length(L_t);
Input: Optimizated trajectory parameters: $\delta p_{\text{hip}}(\theta^+), \text{v}_{hip}, \alpha$;
Input: PD Controller Gain: K_p, K_d
Input: $\theta_{La}, \theta_{Lk}, \theta_{Lh}, \theta_{Rh}, \theta_{Rk}, \theta_{Ra}, \dot{\theta}_{La}, \dot{\theta}_{Lk}, \dot{\theta}_{Lh}, \dot{\theta}_{Rh}, \dot{\theta}_{Rk}, \dot{\theta}_{Ra}$;
Input: Feet States; Encoder Status; Drive Status;
Output: Enable/Disable Motor Drives;
Output: Desired Torque for FOC;
Enable Motor Drives;
repeat
    Wait till all motor drives are Enabled
until (Drive-Status == Enable)
while (¬ Stop-RT) **do**
    Reform $\theta, \dot{\theta}$ from Left/Right(θ_{LR}) to Stance/nonStance(θ_{SnS});
    Calculate time threshold for different domians $\tau_1,\ \tau_2,\ \tau_3$;
    Calculate actual time parameter τ_a ;
    if *real time* $\leq \tau_1$ **then**
        $domain \Leftarrow 1$;
        Desired $\tau_d = real\ time$;
    else
        if $\tau_a > \tau_2$ **then**
            $domain \Leftarrow 2$;
        else
            $domain \Leftarrow 3$;
        Desired $\tau_d = \tau_a + \delta T$;
    Calculate($\xi_1,\ \xi_2$);
    Calculate($y_d,\ \dot{y}_d$) based on τ_d;
    if $domain == 1$ **then**
        Calculate($\theta_d,\ \dot{\theta}_d$) via PHZD reconstruction and Geometric Reconstruction;
    else if $domain == 2$ **then**
        Calculate($\theta_d,\ \dot{\theta}_d$) via PHZD reconstruction;
    else
        Calculate($\theta_d,\ \dot{\theta}_d$) via PHZD reconstruction;
    Apply PD Control law:
    $\tau_{PD}^f = K_p(\theta_a - \theta_d) + K_d(\dot{\theta}_a - \dot{\theta}_d)$;
    Reform τ_{PD}^f from Stance/nonStance to Left/Right;
    Sending Torque Command to FPGA;
    Log Data into Remote Desktop;
Disable Motor Drives;
Report Errors and Stop the Real Time VI;

1. Measure angular velocity by the single-ended incremental quadrature encoders attached to every rotor. Measure joint angle by integrating velocity data. In particular, the incremental encoders operate at 40MHz.
2. Detect stance foot by the heel and toe contact switches. Foot logic is shown in the state machine Figure 13.
3. Torque control. Field-oriented control (FOC) is employed at the motor level.

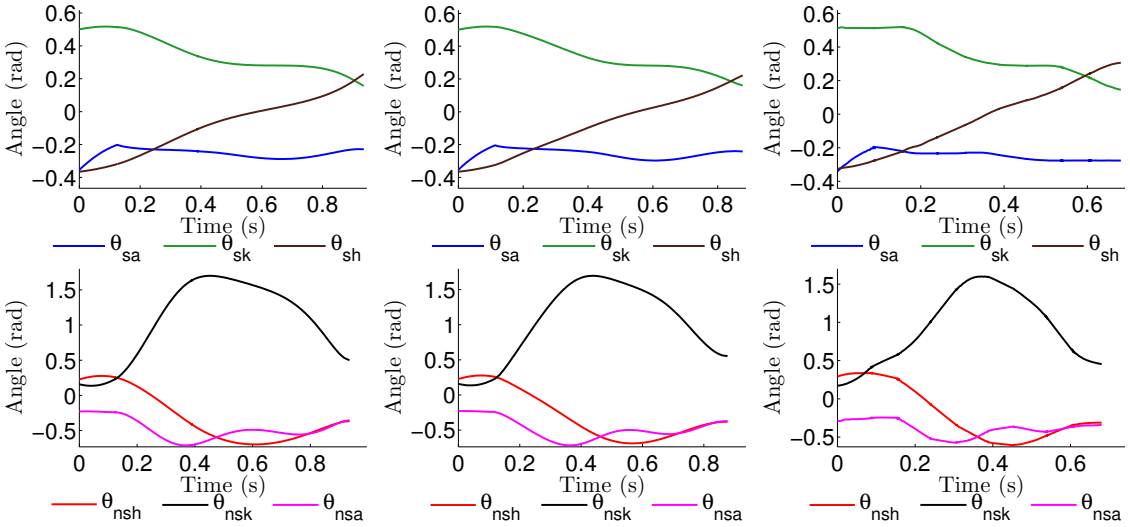

(a) IO control in simulation (b) PD control in simulation (c) PD control in experiment

Figure 14: Comparison of actual joint angles between simulation and experimental results logged during AMBER2 walking.

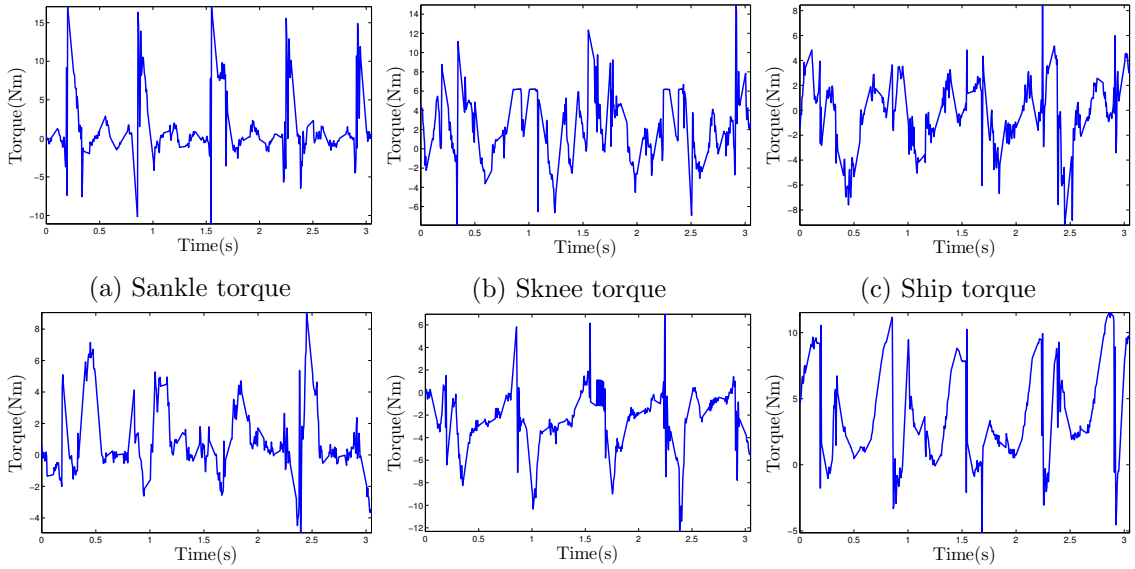

(a) Sankle torque (b) Sknee torque (c) Ship torque

(d) NShip torque (e) NSknee torque (f) NSankle torque

Figure 15: Torque inputs of each motor during the experimental multi-contact robotic walking of AMBER2

The torque is translated to current command. Then a PI controller is applied on the quadrature and direct current for the motor control.

Pseudo-code running in FPGA is shown in Algorithm 2.

Algorithm 2 FPGA Module

Input: PWM Pulses from Absolute Encoders ;
Input: Hall Sensor Signal, Incremental Encoder Signal;
Input: Status of Foot Contact Switches;
Input: Auto-phasing results: Hall Angle, Index Angle;
Input: Hardware Setup: Sample Rate, Current Limitation, FOC Gains;
Input: Enable/Disable Motor Drives;
Input: Three Phase Current From BLDC motors;
Input: Torque Command from RT;
Output: Three Phase PWM Signals to Motor Drives;
Output: $\theta_{abs}, \dot{\theta}_{incremental}$;
Output: L/R Stance Foot; Encoder Status; Drive Status;

loop
    Absolute Encoder Reading logic(10MHz); ▷ Refer to data sheet of absolute encoder, US digital MAE3 kit
    if (Signal low for 2 periods of encoder pulse) **then**
        Encoder Not Working ← 1;
    else
        Encoder Not Working ← 0;
    Incremental Quadrature Encoder Reading Logic(40MHz);
loop
    Compute Desired Current from Torque Command from RT;

    if (Joint Angle exceeds Workspace and Torque Command not trying to stop it) **then**
        Reset Desired Current to 0;
    Compute Three Phase Voltage through Field-oriented Control Logic; ▷ Operation Frequency: 40MHz
    PWM signal Generation logic;
loop
    Guard and Stance Leg Detection Logic using foot contact switches (shown in Figure 13);
    if (Left Leg stance) **then**
        L/R stance ← 0;
    else if (Right Leg stance) **then**
        L/R stance ← 1;

4.4.2 Experiment Results

With the desired joint profile obtained from the PHZD reconstruction, PD controllers are then used to track the angles and velocities:

$$\mu_{PD} = -K_p(\theta^a - \theta^d) - K_d(\dot{\theta}^a - \dot{\theta}^d), \tag{70}$$

where K_p and K_d are proportional and derivative gain matrices, respectively. Before implementing the controller on the physical robot, the proposed PD controller with PHZD reconstruction trajectories was first verified in simulation. Comparing with the simulation results generated using the human-inspired controller as seen in Figure 14a,

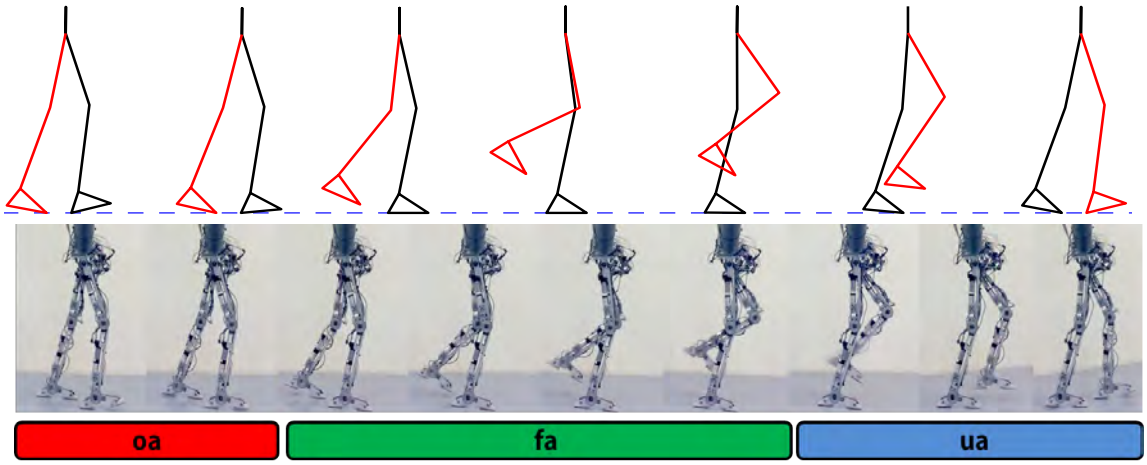

Figure 16: Comparison of walking tiles of the simulated and experimental walking with PD control.

we can see that the PD controller with the reconstruction strategy has achieved similar performance as seen in Figure 14b.

By applying a PD controller to track the reconstructed joint trajectories, AMBER2 has achieved sustainable human-like multi-domain walking. From the attached video [10], the multi-domain walking of AMBER2 displays all the key features of human-like locomotion: toe strike, heel lift and heel strike. Particularly, AMBER2 has continuously walked for 45mins with an approximated 1100m traveling distance. The test ended due to the mechanical failure of a chain. The commanded joint torques for each motor are shown in Figure 15. The comparison between the experimental gait tiles and the simulated gait tiles is shown in Figure 16. The actual joint angles of one step are shown in Figure 14c to compare with the simulated results. These two comparisons show that the robot replicates the formal result very well, i.e., good agreements between practice and theory. The robustness tests are also conducted on AMBER2, showing that AMBER2 can sustain unintended pushes and overcome big obstacles. The details can be seen in video [9].

Also of note is that the system is developed with minimum sensing requirements by only using foot contact switches and incremental encoders. The inherent advantages imbibed in the ECWF (simpler form and better behavior outside of the nominal

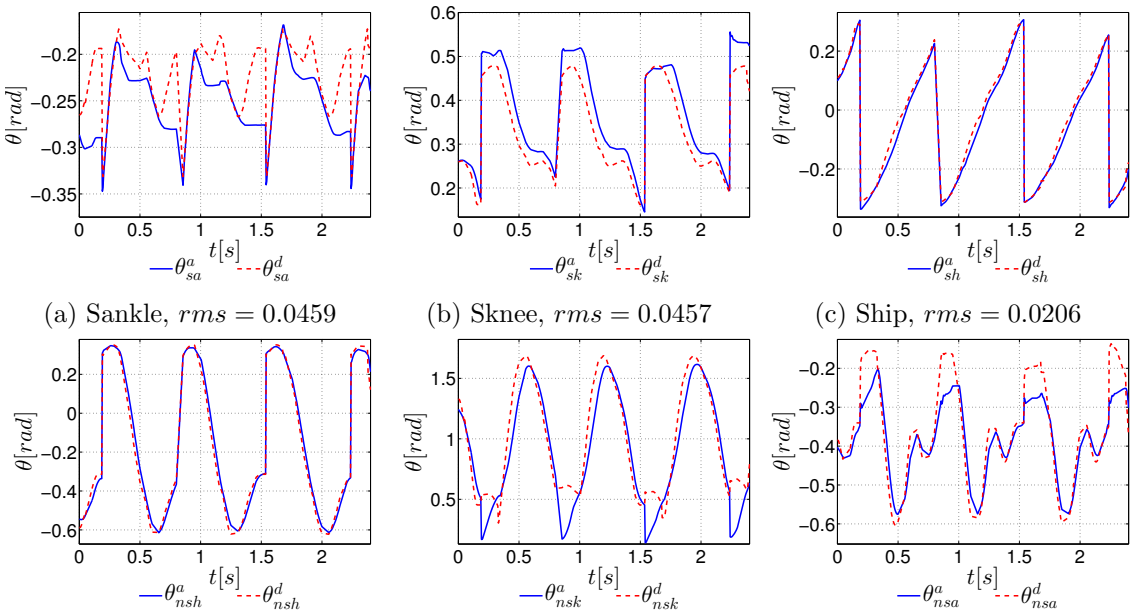

(a) Sankle, $rms = 0.0459$ (b) Sknee, $rms = 0.0457$ (c) Ship, $rms = 0.0206$

(d) NShip, $rms = 0.0435$ (e) NSknee, $rms = 0.2033$ (f) NSankle, $rms = 0.0567$

Figure 17: Actual vs. desired joint angles logged during AMBER2 walking with the PD control law, with rms the root mean square of tracking error.

operation window, see [143] for more details), as well as the robot's design methodology, facilitated the ease of applying such simple control laws to realize walking, which also result in low torque consumption throughout the step. The actual joint angles of multiple steps along with the reconstructed desired joint trajectories are shown in Figure 17.

In conclusion, based on the framework of Chapter 3, this chapter presented an example of the robot model AMBER2. Detailed hybrid system construction along with the PHZD constraints development was discussed explicitly. By using the PHZD reconstruction method for computing desired trajectories, we have successfully implemented the designed gait on the robot AMBER2 with achieving sustainable multi-contact robotic walking.

CHAPTER V

PROSTHETIC CONTROLLER DESIGN

This chapter begins by briefly introducing the framework of variable impedance control. This traditional prosthetic control approach is utilized as a feed-forward term in the development of a novel *control Lyapunov function* (CLF) [18] based *model independent quadratic program* (MIQP) controller for prosthetic joints. Before testing on real human subjects, the proposed novel prosthetic controller is verified in both simulation and experiment on a robotic platform: AMBER1, showing that it can reduce parameter tunning effort and achieve better tracking performance.

5.1 Impedance Control

Based on the notion of impedance control in [56], the torque at each joint during a single step can be represented in a piecewise fashion by a series of passive impedance functions [112] of the form:

$$\mu^{imp} = k(\theta - q^e) + b\dot{\theta}, \tag{71}$$

where, k, q^e and b represent for stiffness, equilibrium angle and damping, respectively, which we refer to as impedance parameters. The phase separation are usually divided based on analysis of human locomotion data, particularly the profile of the knee and ankle joint angles [12], [112].

5.1.1 Example of Impedance Control with AMBER1

We use the robotic model of AMBER1 as an example to describe the impedance control architecture used in the control of lower-limb prosthetic devices [112]. In the context of impedance control, one gait cycle of AMBER1 walking can be divided into four phases, which are demonstrated in Figure 18. We denote the phases as $p = 1, ..., 4$, the separation criteria of which is presented as the following:

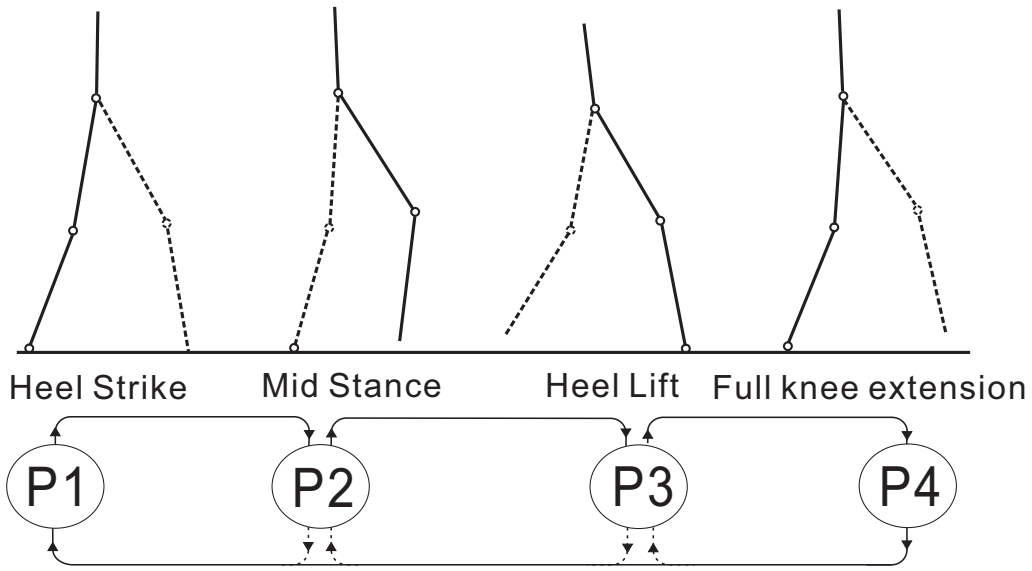

Figure 18: Separation of gait into four phases. The leg with dash line is assumed to be the prosthetic leg. The body segments with solid line is considered as healthy body.

1. P1 from heel strike to mid stance denoted by passing a threshold $\theta_{sf} < thr$ [112],
2. P2 from mid stance to heel lift,
3. P3 from heel lift to full knee extension (i.e. $\dot{\theta}_{nsk} < 0$),
4. P4 from full knee extension to heel strike.

Within each phase, a unique impedance controller for each joint is used to produce control inputs. The commanded torque of an impedance controller at joint i during a phase $p \in \{1, 2, 3, 4\}$ can be represented by the following equation

$$\mu_i^{imp}(t) = k_i(\theta_i(t) - \theta_{i,e}) + b_i\dot{\theta}_i(t), \tag{72}$$

where $\mu_i^{imp}(t)$ denotes the input torque, $\theta_i(t)$ is the angle and $\dot{\theta}_i(t)$ denotes the angular velocity of joint i at time t. The impedance parameters consist of k_i, b_i and $\theta_{i,e}$ representing the stiffness, damping and equilibrium angle for each phase. Note that, these parameters are constant within each phase of the gait and need to be determined specifically with fine tuning.

While impedance control with a finite state machine is one of the most widely used algorithms suggested to date [32], [112], one main challenge is that it requires

the choice of the control parameters (including both impedance parameters and phase switching parameters) for each phase. Currently, clinicians and prosthetic researchers often choose these parameters by trial and error hand tuning for each patient as noted in [112]. Because of its tuning nature and linear formula, it's also hard to guarantee optimality with respect to control performance such as energy consumption. Motivated by these issues, an innovative controller that combines the control Lyapunov functions (realized with a quadratic program) with impedance control (used as a feed-forward term) is proposed with the goal of achieving reduced parameter tuning, better tracking and improved energy efficiency on prosthesis.

5.2 Control Lyapunov Function (CLF)

For nonlinear systems such as manipulators and legged robots, Lyapunov function has been the *gold standard* for establishing stability properties of equilibrium points [19]. For various nonlinear controllers, the asymptotic or exponential stability in the sense of Lyapunov is established based on the existence of a Lyapunov function under specific conditions [103], [111]. In particular, with the ground-breaking work of Artstein [24] and Sontag [110], for a general nonlinear system $\dot{x} = f(x, u)$, a positive definite function $V(x, u)$ is a control Lyapunov function (CLF), if for $\forall x \neq 0$, there exists control input u such that

$$\dot{V}(x, u) = \frac{\partial V(x, u)}{\partial x} f(x, u) \leq 0. \tag{73}$$

Inspired by the advantages such as stability establishment and domain of attraction analysis, this CLF approach has become central to feedback control design. The application includes nonlinear adaptive control [71], robust nonlinear feedback design [90], receding horizon control of nonlinear systems [64] and stabilization of hybrid systems [102]. Recently, the CLF method has been extended to a class of hybrid systems with impulse effects [19]. In this section, we are going to first review this method (as discussed in [19]) with a special focus on bipedal robots.

5.2.1 Exponentially Stabilizing CLF (ES-CLF)

In this section, we discuss the conditions for establishing exponential stability of a periodic orbit of a system on the basis of two lower-dimensional systems. The objective is to lay the foundation framework for more advanced results. We begin by considering the affine control system that can be represented in the zero dynamics form in (40).

Definition 2. *(Based on the Definition 1 in [19]) For system represented as* (39) *and* (40)*, a continuously differentiable function* $V : X_z \to \mathbb{R}$ *is an* **exponentially stabilizing control Lyapunov function (ES-CLF)** *if there exists positive constants* $c_1, c_2, c_3 \geq 0$ *such that*

$$c_1||\eta||^2 \leq V(\eta) \leq c_2||\eta||^2 \tag{74}$$

$$\inf_{u \in U}[L_b V(\eta, \xi) + L_a V(\eta, \xi)u + c_3 V(\eta)] \leq 0 \tag{75}$$

for all $(\eta, \xi) \in X_z \times Z$.

L_b and L_a are the Lie derivatives based on the system (39). Motivated by the constructions in [44], [97], we define the set

$$\mathcal{K}(\eta, \xi) = \{u \in U : L_b V(\eta, \xi) + L_a V(\eta, \xi)u + c_3 V(\eta) \leq 0\} \tag{76}$$

consisting of the control values that result $\dot{V}(\eta, \xi, u) \leq c_3 V(\eta)$. Therefore, when V is an ES-CLF, for any locally Lipschitz continuous feedback control law $u(\eta, \xi)$ satisfies $u(\eta, \xi) \in \mathcal{K}(\eta, \xi)$, the solutions of (39) satisfy:

$$||\eta(t)|| \leq \sqrt{\frac{c_2}{c_1}} e^{-\frac{c_3}{2}t} ||\eta(0)||. \tag{77}$$

Additionally, *Theorem 1* in [19] guarantees that with the assumption that $\mathscr{O}_{\mathbf{Z}}$ is an exponentially stable periodic orbit for the zero dynamics, if there exists an ES-CLF V for all locally Lipschitz continuous feedback $u(\eta, \xi) \in \mathcal{K}(\eta, \xi)$, $\mathscr{O} = \iota_0(\mathscr{O}_{\mathbf{Z}})$ is an exponential stable periodic orbit for (40). This results provides conditions under which the exponential stability of a periodic orbit of a system can be determined based on two lower-dimensional systems, i.e., the controlled dynamics (39) (or transverse dynamics as stated in [19]) and zero dynamics (40). The explicit theorem and detailed proof are omitted here and can be referred to [19].

5.2.2 Rapidly Exponentially Stabilizing CLF (RES-CLF)

In the context of bipedal locomotion with impulses, there exists impacts every step that will push solutions alway from the desired orbit. Therefore, a stronger notion of convergence is required for the controlled dynamics such that it will still be stable, in the sense of Lyapunov, even with persistent disturbance of impacts. The need for a strong form of convergence to tolerate the reset dynamics (i.e., impacts) lead to the notion of a rapidly exponentially stabilizing CLF. With this focus in mind, we introduce the second main result in [19].

Definition 3. *For system represented as* (39) *and* (40)*, a one-parameter family of continuously differentiable functions* $V_\varepsilon : X_z \to \mathbb{R}$ *is said to be a* **rapidly exponentially stabilizing control Lyapunov function (RES-CLF)** *if there exists positive constants* $c_1, c_2, c_3 \geq 0$ *such that for all* $0 < \varepsilon < 1$ *and for all* $(\eta, \xi) \in X_z \times Z$

$$c_1||\eta||^2 \leq V_\varepsilon(\eta) \leq \frac{c_2}{\varepsilon^2}||\eta||^2 \tag{78}$$

$$\inf_{u \in U}[L_b V_\varepsilon(\eta, \xi) + L_a V_\varepsilon(\eta, \xi)u + \frac{c_3}{\varepsilon}V_\varepsilon(\eta)] \leq 0 \tag{79}$$

for all $(\eta, \xi) \in X_z \times Z$.

In the context of RES-CLF, the set $\mathcal{K}$ introduced in (76) becomes

$$\mathcal{K}_\varepsilon(\eta, \xi) = \{u \in U : L_b V_\varepsilon(\eta, \xi) + L_a V_\varepsilon(\eta, \xi)u + \frac{c_3}{\varepsilon}V_\varepsilon(\eta) \leq 0\}, \tag{80}$$

which consists of control values that result in $\dot{V}_\varepsilon(\eta, \xi, u) \leq \frac{c_3}{\varepsilon}V_\varepsilon(\eta)$. It easily to reveal that for any locally Lipschitz continuous feedback control law $u(\eta, \xi)$ satisfies $u(\eta, \xi) \in \mathcal{K}_\varepsilon(\eta, \xi)$, the solutions of (39) satisfy:

$$||\eta(t)|| \leq \frac{1}{\varepsilon}\sqrt{\frac{c_2}{c_1}}e^{-\frac{c_3}{2\varepsilon}t}||\eta(0)||. \tag{81}$$

Def 3 extends the result of Def 2 to provide a means of directly adjusting the rate of exponential convergence with the constant ε through $\frac{c_3}{\varepsilon}$.

With the "sufficiently rapid" convergence rate in hand, *Theorem 2* in [19] extends the result of *Theorem 1* to the case of hybrid system with impacts. With the condition: a) $\mathscr{O}_{\mathbf{Z}}$ is an exponentially stable periodic of the hybrid zero dynamics; b) there

exists a RES-CLF V_ε for the continuous dynamics of (39), then there exists an $\bar{\varepsilon}$ such that for all $0 < \varepsilon < \bar{\varepsilon}$ and for all Lipschitz continuous $u(\eta, \xi) \in \mathcal{K}_\varepsilon(\eta, \xi)$, $\mathscr{O} = \iota_0(\mathscr{O}_{\mathbf{Z}})$ is an exponentially stable hybrid periodic orbit. The explicit theorem statement and the detailed proof can be referred to [19].

In practical applications, different methods can be used to select the control value that is in the set of $\mathcal{K}_\varepsilon(\eta, \xi)$. With the objective of obtaining optimal torque [44], the locally Lipschitz continuous *pointwise min-norm control law* with the following form

$$m(\eta, \xi) = \text{argmin}\{||u|| : u \in K_\varepsilon(\eta, \xi)\} \tag{82}$$

can be used as one good option. More detailed discussion can be found in [19].

Note that, it can be approved that the human-inspired feedback linearization controllers discussed in Chapter 3 fall into the category of RES-CLF, i.e., with $u_v^\varepsilon(\theta, \dot{\theta}, \alpha_v)$ in (37) and (33), $u_v^\varepsilon(\theta, \dot{\theta}, \alpha_v) \in \mathcal{K}_\varepsilon$. The derivation is irrelevant to the discussion of this section and we refer the readers to Section 3 in [19] for more detail.

5.3 RES-CLF based Model Independent Control

As a means for stabilizing hybrid systems undergoing impacts, the RES-CLFs as introduced above can be implemented to yield controllers with stronger convergence guarantee. For practical application, quadratic programs can be used to realize RES-CLFs via inequality constraints. This section will introduce the framework of a RES-CLF based quadratic programming controller. When combined with impedance control (implemented as a feed-forward term), the result is a novel model independent control methodology that can be applied to powered prosthesis control, which yields reduced effort of parameters tuning and improved energy efficiency.

5.3.1 RES-CLF Construction

With the human-inspired outputs defined in (25), the dynamics in (5) can be reformulated as the output dynamics as in (83). We restate it here for easy reference

$$\begin{bmatrix} \dot{y}_1 \\ \ddot{y}_2 \end{bmatrix} = \underbrace{\begin{bmatrix} L_f y_1(\theta, \dot{\theta}) \\ L_f^2 y_2(\theta, \dot{\theta}) \end{bmatrix}}_{L_f} + \underbrace{\begin{bmatrix} L_g y_1(\theta, \dot{\theta}) \\ L_g L_f y_2(\theta, \dot{\theta}) \end{bmatrix}}_{A} u. \tag{83}$$

By picking a general feedback linearization controller:

$$u = A^{-1}(L_f + \mu), \tag{84}$$

equation (83) becomes:

$$\begin{bmatrix} \dot{y}_1 \\ \ddot{y}_2 \end{bmatrix} = \mu. \tag{85}$$

μ can be designed properly such that one can drive both $y_1 \to 0$ and $y_2 \to 0$ exponentially. For example, one can choose the human-inspired feedback linearziation controllers defined in (33) and (37), which will guarantee "sufficiently rapid" exponential convergence [19]. However, due to the lack of model information, it is not possible to realize this feedback linearization controller on prostheses. As a result, traditional PID control or variable impedance control are typically seen as a more favorable option since it does not require model information and can be applied in a decentralized way. However, PID controllers (same as impedance controllers) lack formal guarantees (when applied to nonlinear systems) and require hand tuning [25]. This motivates the need to find a new control strategy that overcomes the weaknesses of PID control while maintaining model insensitivity.

By defining the vector $\eta = (y_1, y_2, \dot{y}_2) \in \mathbb{R}^{n_1+2\times n_2}$ with n_1, n_2 denoting the numbers of relative degree one virtual constraints and relative degree two virtual constraints, respectively, equation (85) can be written as a linear affine control system:

$$\dot{\eta} = \underbrace{\begin{bmatrix} 0_{n_1\times(n_1+n_2)} & 0_{n_1\times n_2} \\ 0_{n_2\times(n_1+n_2)} & I_{n_2\times n_2} \\ 0_{n_2\times(n_1+n_2)} & 0_{n_2\times n_2} \end{bmatrix}}_{F} \eta + \underbrace{\begin{bmatrix} I_{n_1\times n_1} & 0_{n_1\times n_2} \\ 0_{n_2\times n_1} & 0_{n_2\times n_2} \\ 0_{n_2\times n_1} & I_{n_2\times n_2} \end{bmatrix}}_{G} \mu, \tag{86}$$

where clearly (F, G) is controllable. Considering the Continuous Algebraic Riccati Equations (CARE) with $Q = Q^T > 0$:

$$F^T P + PF - PGG^T P + Q = 0, \tag{87}$$

we can obtain a point-wise optimal solution $P = P^T > 0$.

Letting

$$\gamma := \frac{\lambda_{min}(Q)}{\lambda_{max} P} > 0, \tag{88}$$

where $\lambda_{min}(.)$ and $\lambda_{max}(.)$ represent the minimum and maximum eigenvalues of a given symmetric matrix, we could apply the Rayleigh-Ritz inequality [101] to obtain

$$Q \geq \gamma P. \tag{89}$$

Therefore, an exponential stabilizing Lyapunov function can be defined as

$$V(\eta) = \eta^T P \eta \tag{90}$$

that satisfies

$$\dot{V}(\eta) \leq -\lambda V(\eta) \tag{91}$$

Note that, it is a direct result from the construction of $V(\eta)$ that $V(\eta)$ also satisfies

$$\lambda_{min}(P)||\eta||^2 \leq V(\eta) \leq \lambda_{max}(P)||\eta||^2. \tag{92}$$

With the motivation to construct a RES-CLF [19] for hybrid bipedal systems, we take a further step by defining

$$\eta_\varepsilon = \begin{bmatrix} y_1 \\ \frac{1}{\varepsilon} y_2 \\ \dot{y}_2 \end{bmatrix} = \underbrace{\begin{bmatrix} 0_{n_1 \times (n_1+n_2)} & 0_{n_1 \times n_2} \\ 0_{n_2 \times (n_1+n_2)} & \frac{1}{\varepsilon} I_{n_2 \times n_2} \\ 0_{n_2 \times (n_1+n_2)} & 0_{n_2 \times n_2} \end{bmatrix}}_{M_\varepsilon} \eta \tag{93}$$

with convergence rate $\varepsilon > 0$. The parameter ε can be viewed as time scale, which has the effect of speeding up the rate of convergence. More detailed discussion can be found in [19]. Additionally, letting $P_\varepsilon := M_\varepsilon P M_\varepsilon$, one can show that (87) implies

$$F^T P_\varepsilon + P_\varepsilon F - \frac{1}{\varepsilon} P_\varepsilon G G^T P_\varepsilon + \frac{1}{\varepsilon} M_\varepsilon Q M_\varepsilon = 0, \tag{94}$$

By defining $V_\varepsilon(\eta) = \eta^T P_\varepsilon \eta$, with dynamics (86), we have

$$\dot{V}_\varepsilon(\eta, \mu) + \frac{\gamma}{\varepsilon} V_\varepsilon(\eta, \mu) \leq \eta^T P_\varepsilon G(\frac{1}{\varepsilon} G^T P_\varepsilon \eta + 2G\mu), \tag{95}$$

from which it follows that

$$\inf_{u \in U} [\dot{V}_\varepsilon(\eta, \mu) + \frac{\lambda}{\varepsilon} V_\varepsilon(\eta)] \leq 0. \tag{96}$$

Note that, following the coordinate transformation (93), we also have

$$\lambda_{min}(P)||\eta||^2 \leq V_\varepsilon(\eta) \leq \frac{1}{\varepsilon^2} \lambda_{max}(P)||\eta||^2, \tag{97}$$

the details of which can be referred to [19]. Therefore, $V_\varepsilon(\eta)$ is a RES-CLF with $c_1 = \gamma_{min}(Q)$, $c_2 = \gamma_{max}(P)$ and $c_3 = \lambda$.

5.3.2 RES-CLF Quadratic Program

With the RES-CLF $V_\varepsilon(\eta)$ in hand, we introduce a quadratic program method to solve for control input μ practically. We begin by differentiating this function with respect to the linearized system (86), which yields:

$$\dot{V}_\varepsilon(\eta) = L_F V_\varepsilon(\eta) + L_G V_\varepsilon(\eta)\mu, \tag{98}$$

where $L_F V_\varepsilon(\eta) = \eta^T (F^T P_\varepsilon + P_\varepsilon F)\eta$, $L_G V_\varepsilon(\eta) = 2\eta^T P_\varepsilon G$.

In order to exponentially stabilize the system, we want to find μ such that we have:

$$L_F V_\varepsilon(\eta) + L_G V_\varepsilon(\eta)\mu \leq -\frac{\gamma}{\varepsilon} V_\varepsilon(\eta). \tag{99}$$

Therefore, a locally point-wise optimal μ could be found by solving the following quadratic program (QP):

$$m(\eta) = \underset{\mu \in \mathbb{R}^{n_1+n_2}}{\operatorname{argmin}} \ \mu^T \mu \tag{100}$$

$$\text{s.t} \quad \varphi_0(\eta) + \varphi_1(\eta)\mu \leq 0, \tag{CLF}$$

where $\varphi_0(\eta) = L_F V_\varepsilon(\eta) + \frac{\gamma}{\varepsilon} V_\varepsilon(\eta)$ and $\varphi_1(\eta) = L_G V_\varepsilon(\eta)$. It's important to note that solution of this QP problem is also the solution of the min-norm controller (82). By

solving this quadratic program, we have a piecewise locally optimal control input $\mu =: m(\eta) =: m(\theta, \dot{\theta})$ in (CLF), which can be put back to the feedback linearization controller (84) to obtain rapidly exponential convergence for the original system [19].

$$u(\theta, \dot{\theta}) = A^{-1}(\theta, \dot{\theta})(L_f(\theta, \dot{\theta}) + m(\theta, \dot{\theta})). \tag{101}$$

To take a further step, we could intentionally relax the CLF constraints such that torque bounds can be imposed in this QP. In particular, this is realized by penalizing for this relaxation with a penalty constant $p > 0$. We consider the relaxed QP as:

$$\begin{aligned} \underset{(\delta,\mu)\in\mathbb{R}^{n_1+n_2+1}}{\operatorname{argmin}} \quad & p\delta^2 + \mu^T\mu && (102)\\ \text{s.t} \quad & \varphi_0(\eta) + \varphi_1(\eta)\mu \leq \delta, && \text{(CLF)}\\ & A^{-1}(-L_f + \mu) \leq u_{MAX}, && \text{(Max Torque)}\\ & -A^{-1}(-L_f + \mu)\mu \leq u_{MAX}. && \text{(Min Torque)} \end{aligned}$$

where u_{MAX} are the admissible torque values, usually determined by the actuators. While the min-norm controller can be solved in closed form [19], the immediate advantage of this QP approach is that torque bounds can be directly implemented in this formulation where the optimal control value that respects the torque bounds can be found [20].

5.3.3 Model Independent QP (MIQP)

With the μ solved from (102) and the locomotion controller (101), the end result is an piece-wise optimal controller that respects torque bounds at the same time. However, as mentioned at the beginning, control of prosthetic devices suffers from the fact that it is impossible to get accurate model information (i.e., $L_f(\theta, \dot{\theta})$ and $A(\theta, \dot{\theta})$ in (84)) for the amputee-prosthesis system. Therefore, instead of substituting μ to (84), we propose the idea of applying μ directly as the control input

$$u(\theta, \dot{\theta}) = \mu(\theta, \dot{\theta}), \tag{103}$$

where μ is solved with the following quadratic program.

$$\underset{(\delta,\mu)\in\mathbb{R}^{n_1+n_2+1}}{\operatorname{argmin}} \quad p\delta^2 + \mu^T\mu \tag{104}$$

$$\text{s.t} \quad \varphi_0(\eta) + \varphi_1(\eta)\mu \leq \delta, \tag{CLF}$$

$$\mu \leq \mu_{MAX}, \tag{Max Torque}$$

$$-\mu \leq \mu_{MAX}. \tag{Min Torque}$$

Similarly, μ_{MAX} are the admissible torque values. The end result of solving this *model independent quadratic program* (MIQP) is a controller that does not require model information.

More explicitly, the main principle of the MIQP algorithm is to construct a linear control system (86) that only focuses on the errors between the actual outputs and desired outputs, while not requiring any information about the original model. This QP problem yields the control input μ that regulates the errors of the output dynamics in a rapidly exponentially stable fashion while simultaneously guaranteeing the resulting torque is physically applicable. Note that, the control system (86) can also be considered as the affine form of the simplest trajectory tracking problem with $\ddot{y} = \mu$. Therefore, the controller discussed in this section can potentially be implemented on a more general spectrum.

5.3.4 MIQP+Impedance Control

While MIQP control method benefits from model independence, torque solutions are not necessarily unique (i.e. the controller will generate an identical torque for two different systems with the same tracking error). Consequently, the controller will be less responsive to the actual system and will tend to have overshooting problems. Therefore, model information is added in the form of impedance controllers to achieve a more responsive system; this motivates the introduction of MIQP+Impedance control. With the impedance controller μ^{imp} added as a feed-forward term, the desired torque μ^d of the prosthetic joints can be stated as:

$$\mu^d = \mu^{qp} + \mu^{imp}, \tag{105}$$

where μ^{qp} is the torque computed from the MIQP problem. Taking this idea further, we add the impedance term μ^{imp} into the MIQP construction for the total hardware torque bounds, which yields the following MIQP+Impedance formula as follows:

$$\underset{(\delta,\mu^{qp})\in\mathbb{R}^{n_1+n_2+1}}{\operatorname{argmin}} \quad p\delta^2 + \mu^{qpT}\mu^{qp} \tag{106}$$

$$\text{s.t } \varphi_0(\eta) + \varphi_1(\eta)\mu^{qp} \leq \delta - \varphi_1(\eta)\mu^{imp}, \tag{CLF}$$

$$\mu^{qp} \leq \mu^{qp}_{MAX}, \tag{Max QP Torque}$$

$$-\mu^{qp} \leq \mu^{qp}_{MAX}, \tag{Min QP Torque}$$

$$\mu^{qp} \leq \mu_{MAX} - \mu^{imp}, \tag{Max Input Torque}$$

$$-\mu^{qp} \leq \mu_{MAX} + \mu^{imp}. \tag{Min Input Torque}$$

By adding the impedance control as a feed-forward term into the input torque, the model independent dynamic system (86) gathers proper information about the system. It can, therefore, adjust μ^{qp} accordingly to accommodate for the feed-forward term to achieve good tracking. By setting the QP torque bounds μ^{qp}_{MAX}, problems with overshoot will be eliminated. We also set the total input torque bounds for the QP problem such that the final optimal input torques (105) will satisfy the hardware torque bounds μ_{MAX} and allow the control to be implemented practically on the robots or prosthetic devices.

Note that, different from the pure variable impedance controller (as discussed in Sec. 5.1), the MIQP+Impedance control uses the impedance control only as a feed-forward term. Therefore, the impedance parameters do not need to be fine tuned precisely. One of the author's former work took a different approach in [12] to learn the impedance parameters for a lower-limb prosthesis based on the human-inspired optimization and the observation of unimpaired human walkers (details can be referred to [12]). The results have been validated in both simulation and experiment with a transfemoral prosthetic device by using the learned impedance parameters for the pure impedance control. While this impedance parameter learning method can not extend to more complex bipedal models that are more than five links, the learned impedance

parameters are sufficient for being used as a feed-forward term. Therefore, by utilizing the impedance learning algorithm discussed in [12], the MIQP+Impedance control can eliminate the tuning of impedance parameters.

Remark. In order to make the MIQP controller work properly, there are three parameters to be determined, which are ε, p and the torque bounds μ_{MAX}^{qp}, μ_{MAX}. Specifically, ε determines the outputs convergence rate; p is the CLF penalty term that regulates the wellness of the tracking performance and $\mu_{MAX}^{qp}, \mu_{MAX}$ are defined based on the hardware limitation. If ε or p are increased (corresponding to quicker convergence and heavier penalty for bad tracking), the controller will attempt to match the desired trajectories more closely but may begin to violate μ_{MAX}^{qp} due to increased torque demands, causing the QP to fail. More detailed discussion about the feasibility of the QP can be referred to [92]. To summarize, the unique merit of the MIQP controller is that it only requires the output error as the input and stabilizes the output dynamics in a rapidly exponentially convergent manner. As a result, given that μ_{MAX}^{qp} is sufficiently large, the MIQP controller will maintain the ability to adapt to different systems without requiring accurate model information.

5.4 Verification on Robot AMBER1

Before implementing the optimization-based controller on a prosthetic device with actual human subjects, the controller is verified on a bipedal robot: AMBER1 in both simulation and experiment. The results are discussed in this section.

5.4.1 AMBER1 Test Platform

AMBER1 is a planar bipedal robot with 5 links (one torso, two thighs and two calves, see Figure 19). AMBER1 is powered by four DC motors and is under-actuated at the ankle due to a point-foot interaction with the ground. In previous work, AMBER1 has achieved stable and human-like walking experimentally using a proportional voltage controller [133]. The work in this dissertation will use AMBER1 as the platform to test the proposed prosthetic controller. In particular, the right calf is

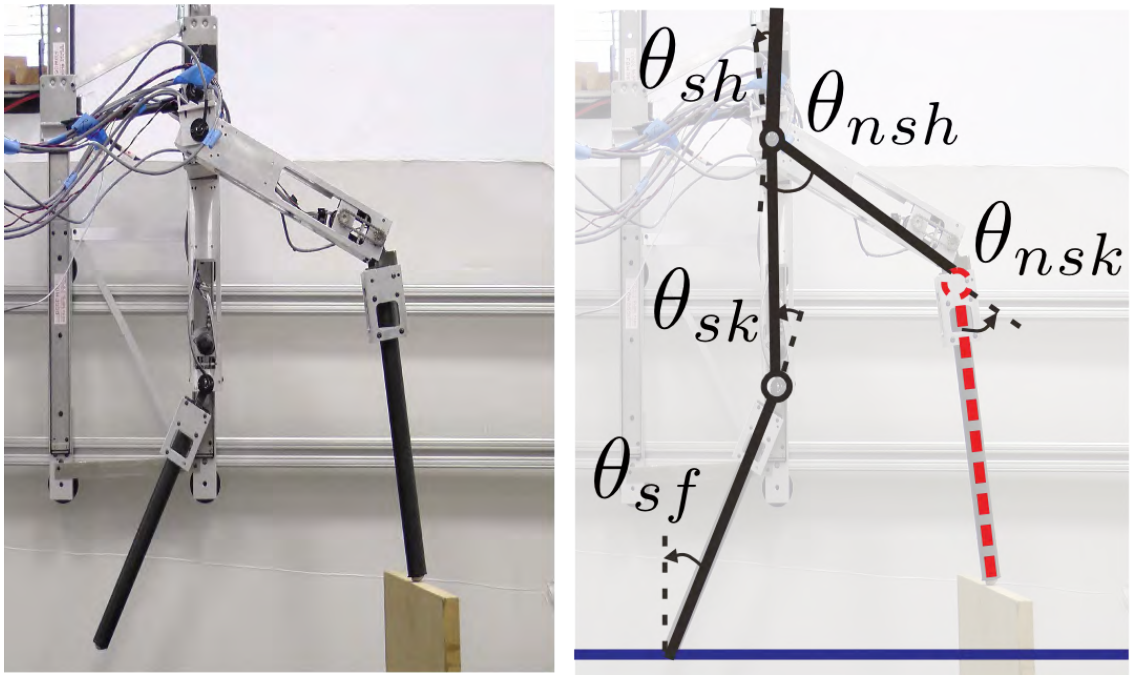

Figure 19: The biped robot AMBER1 (left) and the angle conventions (right). The right leg with red dash line denotes the prosthetic device; the red dash circle represents the prosthesis joint that will be controlled using prosthetic controllers.

assumed to be the "prosthetic device" which has the same length and mass configuration of the left calf that is marked as the "healthy leg". The proposed controller will be implemented on the prosthetic joint, i.e., on the right knee joint. The controller for the remaining actuators will still be the original voltage controller discussed in [133].

The configuration of the AMBER1 model is pictured in Figure 19 and given by the coordinates $\theta = (\theta_{sa}, \theta_{sk}, \theta_{sh}, \theta_{nsh}, \theta_{nsk})^T \in Q \subset \mathbb{R}^5$. With the mass and length properties corresponding to the physical robot AMBER1, the equations of motion for the robot can be obtained with equation (5). Note that, since AMBER1 has DC motors with small inductances, the electromechanical system with voltage inputs has the following form:

$$V_{in} = R_a i_a + K_\omega \omega, \tag{107}$$

where $V_{in} \in \mathbb{R}^{4\times 1}$ is the vector of voltage inputs to the motors, $i_a \in \mathbb{R}^{4\times 1}$ is the vector of currents through the motors, $R_a \in \mathbb{R}^{4\times 4}$ is the resistance matrix, and $\omega \in \mathbb{R}^{4\times 1}$ is

the vector of motor speed which has the relation as $\omega = r_m\dot{\theta}$ with $r_m \in \mathbb{R}^{4\times4}$ denoting the total reduction of the system. Since the motors are controlled individually, with the torque constant $K_\varphi \in \mathbb{R}^{4\times4}$, the applied inputs are:

$$u = K_\varphi R_a^{-1}(V_{in} - K_\omega\omega). \tag{108}$$

Therefore, the impedance torque and QP torque discussed in Sec. 5.1 and Sec. 5.3 will be replaced with impedance voltage V^{imp} and QP voltage V^{qp}, respectively [141].

5.4.2 Simulation Verification with AMBER1

With the model in hand, the robotic gait can be obtained using the optimization problem as discussed in Chapter 3 with outputs specific to the model of AMBER1 (details can be found in [141]). The simulation results of AMBER1 is then discussed. Tracking performance of various controllers on the joints of the prosthesis are compared. Robustness tests are also performed and compared for various controllers.

5.4.2.1 Tracking Performance with Different Controllers

With the exception of the prosthesis joint, on which different controllers will be implemented, the remaining joints will be controlled with the proportional voltage control. Three different controllers are tested as the prosthetic controller: proportional control, impedance control and MIQP+Impedance control. Figure 20 shows the tracking performances of the prosthesis knee joint using these three controllers. Using the tracking results of proportional control as the nominal reference as shown in Figure 20a, we can see that the MIQP+Impedance control shown in Figure 20c improves the tracking performance significantly for both stance and non-stance phases w.r.t the *RMS* error, while impedance control shown in Figure 20b yields worse tracking results.

5.4.2.2 Stability Testing

In additional to tracking performance, the demonstration of stability and robustness are of high importance on a prosthesis controller. Two robustness tests are applied to the robot in simulation; one is to add an instantaneous push and another

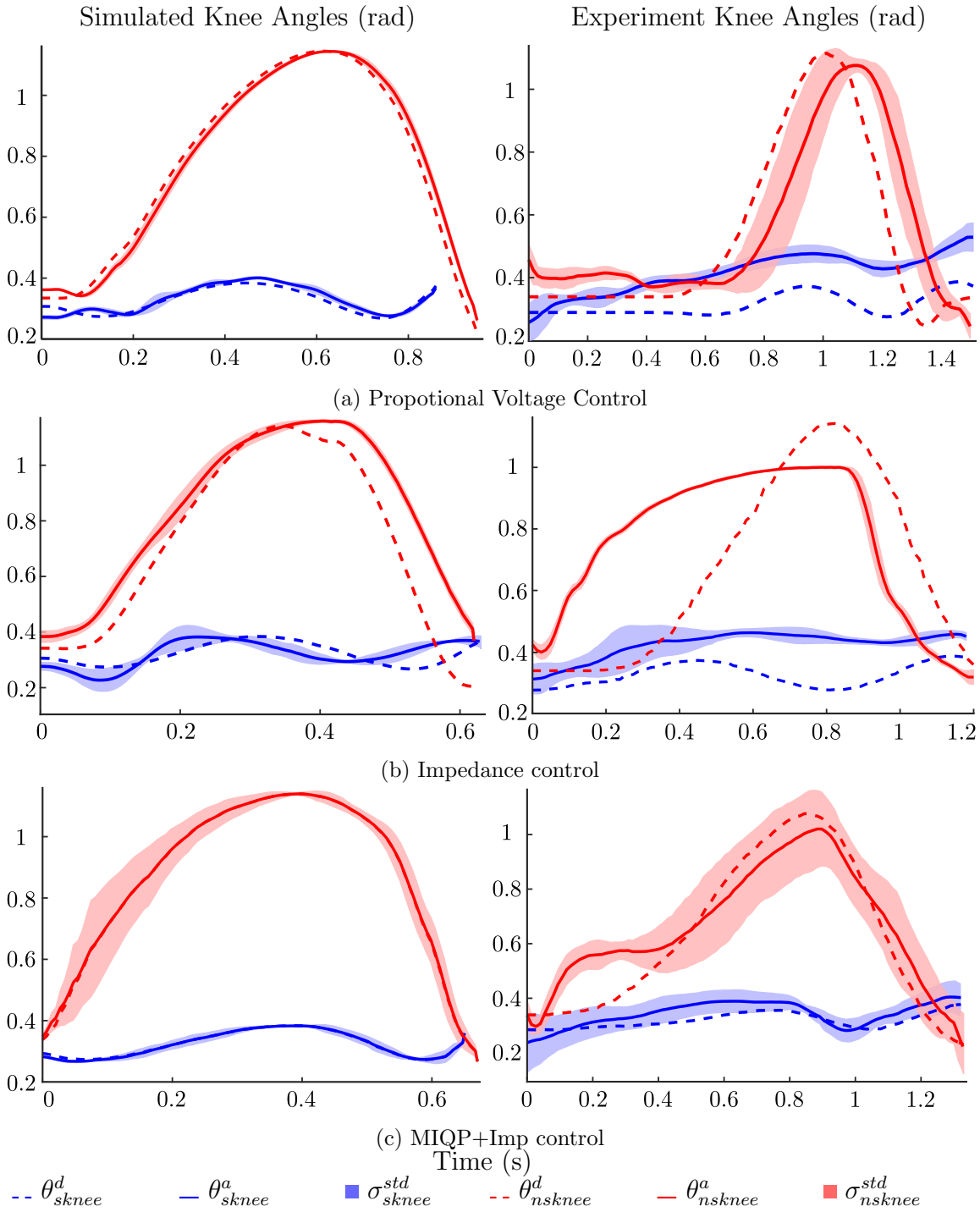

Figure 20: The averaged actual and desired outputs of the prosthesis knee joint along with the one standard deviation over 20 steps with different controllers in both simulation (left) and experiment (right).

one is to let the robot walk above an unforeseen obstacle. In particular, a $2N$ impulse force (lasting for $0.05s$) has been applied to the prosthetic leg while in swing phase. The results show that the prosthetic device with the proposed controller can tolerate

this disturbance and maintain good tracking. The same disturbance was also tested using only the impedance controller; the tracking error becomes bigger due to the disturbance and the robot falls after 6 steps. For the obstacle test, we let the robot walk over a $20mm$ high obstacle. The gait tiles of the simulation can be seen in Figure 22, showing that the robot can overcome the obstacle smoothly. A similar test is also conducted with only impedance control. While the robot can walk over the obstacle, tracking performance is degraded.

5.4.3 Experimental Verification on AMBER1

Starting with the estimated impedance parameters obtained from the simulation discussed above, we are able to tune the parameters within a small range and get sustainable walking by only using the impedance controller. The tracking results of using impedance control can be seen in Figure 20b. Compared to the tracking of proportional control as shown in Figure 20a, the impedance control shows worse tracking performance.

Using the impedance parameters from the previous section, we apply impedance control as the feed-forward term while using the MIQP as the feedback term to correct the tracking errors and reject the disturbances. From Figure 20c, we can see the tracking with using the MIQP+Impedance controller is the best among the three methods in both stance phase and non-stance phase (RMS error reduced by more than 50% for both phases). The detailed comparisons of both the simulation and experimental results are shown in Table 2. One thing the readers may notice is

Table 2: Simulation and Experiment Results Comparison of AMBER1 Using Different Controllers over 20 Steps.

Control		**Simulation** $[rad]$			**Experiment** $[rad]$		
		e_{rms}	e_{max}	σ_{rms}^{std}	e_{rms}	e_{max}	σ_{rms}^{std}
P	**sknee**	0.0155	0.0355	0.0028	0.1098	0.1563	0.0105*
	nsknee	0.0355	0.0738	0.0018*	0.1594	0.3823	0.0112*
Imped	**sknee**	0.0401	0.0780	0.0144	0.1060	0.1706	0.0172
	nsknee	0.1403	0.3036	0.0129	0.2740	0.4770	0.0255
MIQP	**sknee**	0.0014*	0.0109*	0.0014*	0.0355*	0.0637*	0.0148
+Imp	**nsknee**	0.0037*	0.0220*	0.0037	0.1017*	0.2220*	0.0283

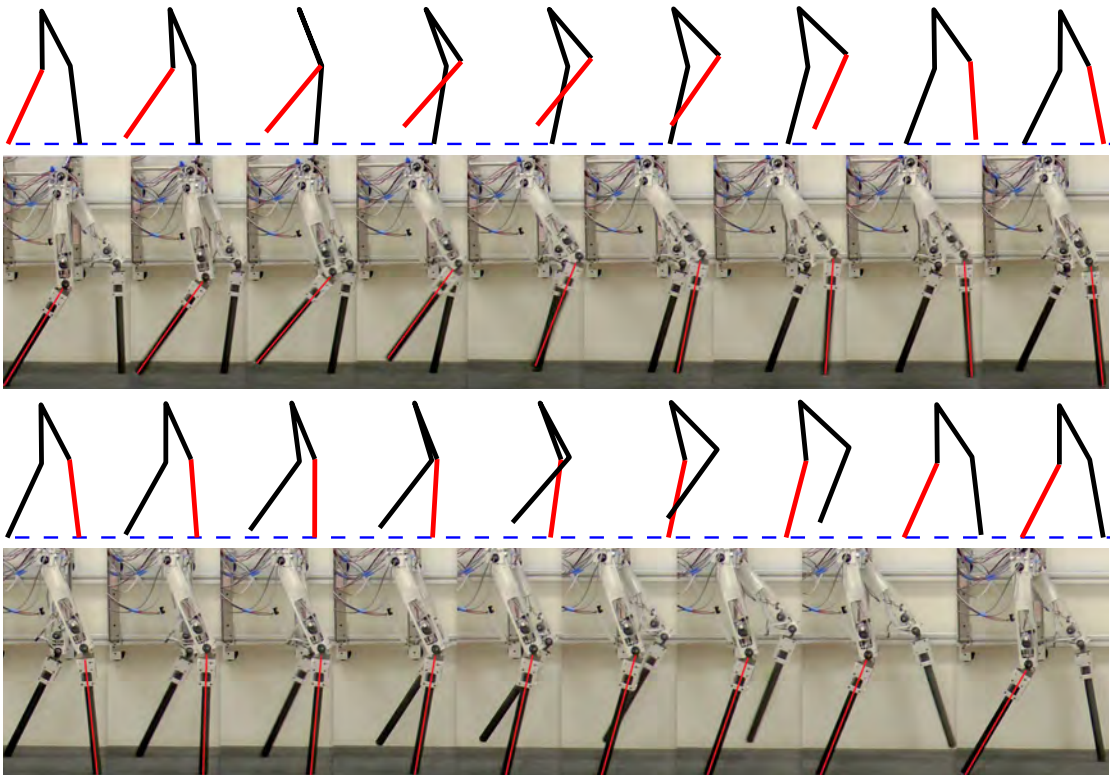

Figure 21: Experimental and simulation gait tiles using MIQP + Impedance control. Red line indicates the prosthesis.

that the MIQP+Impedance controller tends to have larger tracking variance in both the simulation and experiment, which can be seen in Figure 20. Similar results can also be seen in Table 2, in which the lowest one standard deviations of rms error are found in the tests with proportional or impedance control. Particularly, with a set of fixed controller gain, i.e., fixed control parameters, the proportional controller or impedance controller can not adjust tracking performance during the tests. On the other hand, the MIQP+Impedance controller can achieve good tracking performance in a more dynamic way even with asymmetric gaits. The gait tiles of two step walking by using MIQP+Impedance control can be seen in Figure 21.

Robustness of walking with MIQP+Impedance control was also tested, demonstrating the ability to overcome a $40mm$ block and withstand large pushes applied to the prosthetic leg. Note that, with impedance control, the robot can only overcome a $20mm$ block. The experiment obstacle walking gait tiles are compared with the simulated gait tiles, as shown in Figure 22.

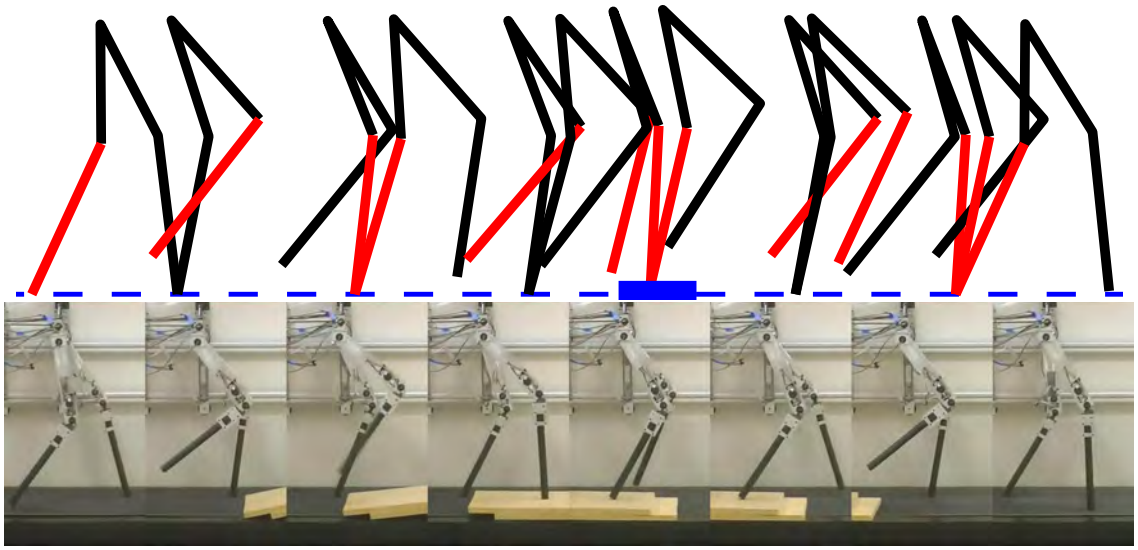

Figure 22: Gait tiles of walking over an obstacle with MIQP+Impedance control in both simulation (top) and experiment (bottom).

With the verification in both simulation and experiment as discussed above, one can conclude that the proposed optimization-based nonlinear controller shows improved tracking performance and demonstrates the ability to be more robust to disturbances and obstacles than the traditional approaches.

CHAPTER VI

REALIZATION ON A PROSTHESIS AMPRO1

With the systematic methodology including gait generation and controller implementation verified on the robot platform, we now have the framework to experimentally realize it on a powered transfemoral prosthesis: AMPRO1. The experiment setup including the design of the prosthesis AMPRO1 and the testing subjects is introduced first. Based on the invariant human trajectory and the IMU motion capture systems, an optimization method for prosthetic gait design is discussed explicitly. Finally, the results of using the MIQP+Impedance controller along with other controllers for achieving stable prosthetic walking are analyzed in a comparative study.

6.1 Experiment Setup of AMPRO1

The design of AMPRO1 and the testing subjects are introduced fist in this section. We also present the detailed control architecture of the embedded software for the experimental validation.

6.1.1 Design of AMPRO1

AMPRO1 is designed to be a high powered, compact and structurally safe device. The device uses a roller chain drive train consisting of a 374 W brushless DC motor (Moog BN34 silencer series) and a harmonic gearhead to actuate both the ankle and knee joints in the sagittal plane. This design utilizes two incremental encoders (US Digital E5) for each motor and is designed to incorporate absolute encoders at the joints. Two ELMO motion controllers (Gold Solo Whistle) are used for low-level torque control purposes. Additionally, two FlexiForce (Parallax 30056) force sensors are located at the base of the foot (mounted at the toe and heel separately) to measure the normal reaction forces which are used for the purpose of contact point switch. The prosthetic device is powered by a 8-cell LiPo battery with 4000 mAh capacity.

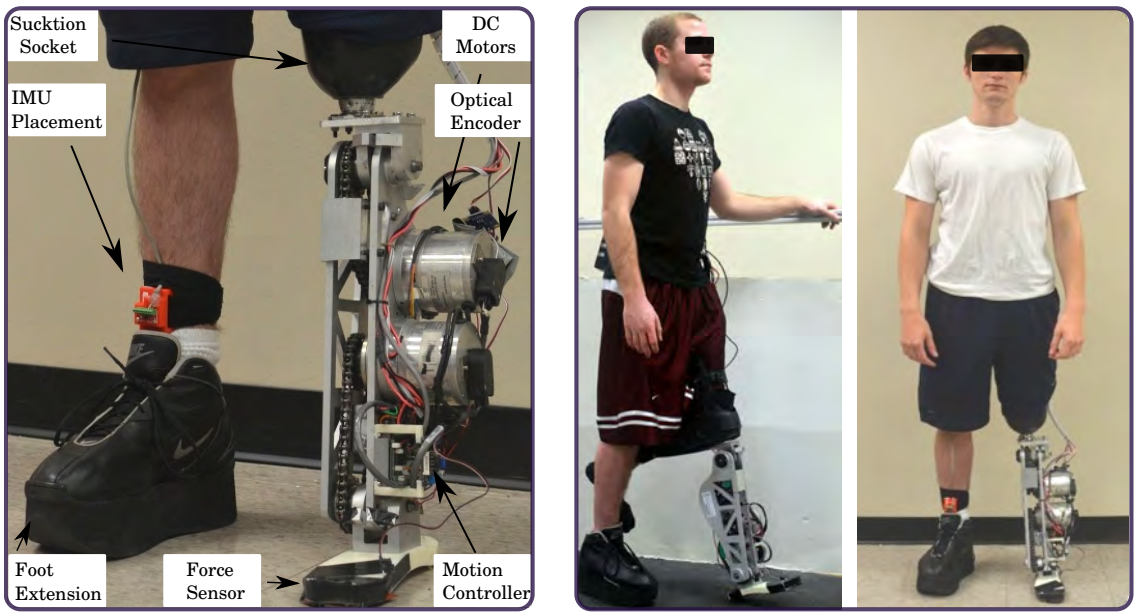

Figure 23: Components diagram of the prosthesis AMPRO1 (left) and the testing subjects (right, one impaired subject and one transfemoral amputee).

The technical diagram can be seen in Figure 23 and the design specifications are listed in Table 3.

6.1.2 Testing Subjects

The testing amputee subject in this study has been a unilateral amputee of three years due to osteosarcoma. The subject is a 19-year-old male that utilizes a passive knee prosthesis (Ossur Total Knee 2100) for daily-use paired with a Ossur K2 Sensation foot. For the conducted experiments, the test subject's daily-use suction socket was connected to AMPRO1 using a standard pyramid connector. Some of the important parameters for the test subject were measured and are located in Table 3. The residual limb of the subject was measured from the approximate location of the lateral condyle to the true ankle joint and from the true ankle joint to the base of the foot (for the calf and foot measurements respectively). During the experimental trials, the test subject used a custom made shoe that features a small extension of the sole of the shoe. This extension was required in order to have the subject's residual limb of equal length to the combination of AMPRO1 and the subject's suction socket connection.

An unimpaired subject, which shares similar anthropomorphic parameters (limb length and mass) as the amputee subject is also considered in the experimental testing. The reasons of considering a secondary unimpaired subject are twofold. The first reason is for collecting healthy human locomotion data, which will be utilized as a reference database when designing various gaits (such as level-ground and stair ascending walking gaits) for the amputee subject. The second reason is that the participated amputee subject in this dissertation is volunteered for testing. As an undergraduate student, the available testing time is limited considering the heavy course load. Therefore, the unimpaired subject is considered as the initial testing subject for various controllers and motion types.

6.1.3 Control Architecture

The architecture of the control scheme for the transfemoral prosthesis includes three hierarchical levels, the pseudo-code diagram of which can be seen in Figure 24. In particular, a low-level controller is realized in a closed-loop by the ELMO motion drive, which is able to compensate for friction, damping effects and transmission dynamics of the motors. The two encoders are connected directly to the ELMO drives for the purposes of both motor control and joint feedback information. The mid-level controllers generate the input torques for the joints using various controllers. The high-level controller is in charge of the interaction between the robot and human,

Table 3: Specifications of the AMPRO1 and the Subject.

Specifications	**AMPRO1**	**Amputee Subject**
Total Weight (Kg)	8.1	62
Total Height (cm)	56.3	173
Socket Length (cm)	8.8	*
Calf Height (cm)	40.7	41.6
Foot Height (cm)	6.8	9
Shoe Extension (cm)	*	5.7
Ankle Range of Movement(deg)	-20 $\sim$ 30	*
Knee Range of Movement(deg)	0 $\sim$ 70	*
Max Joint Velocity (rpm)	81.25	*

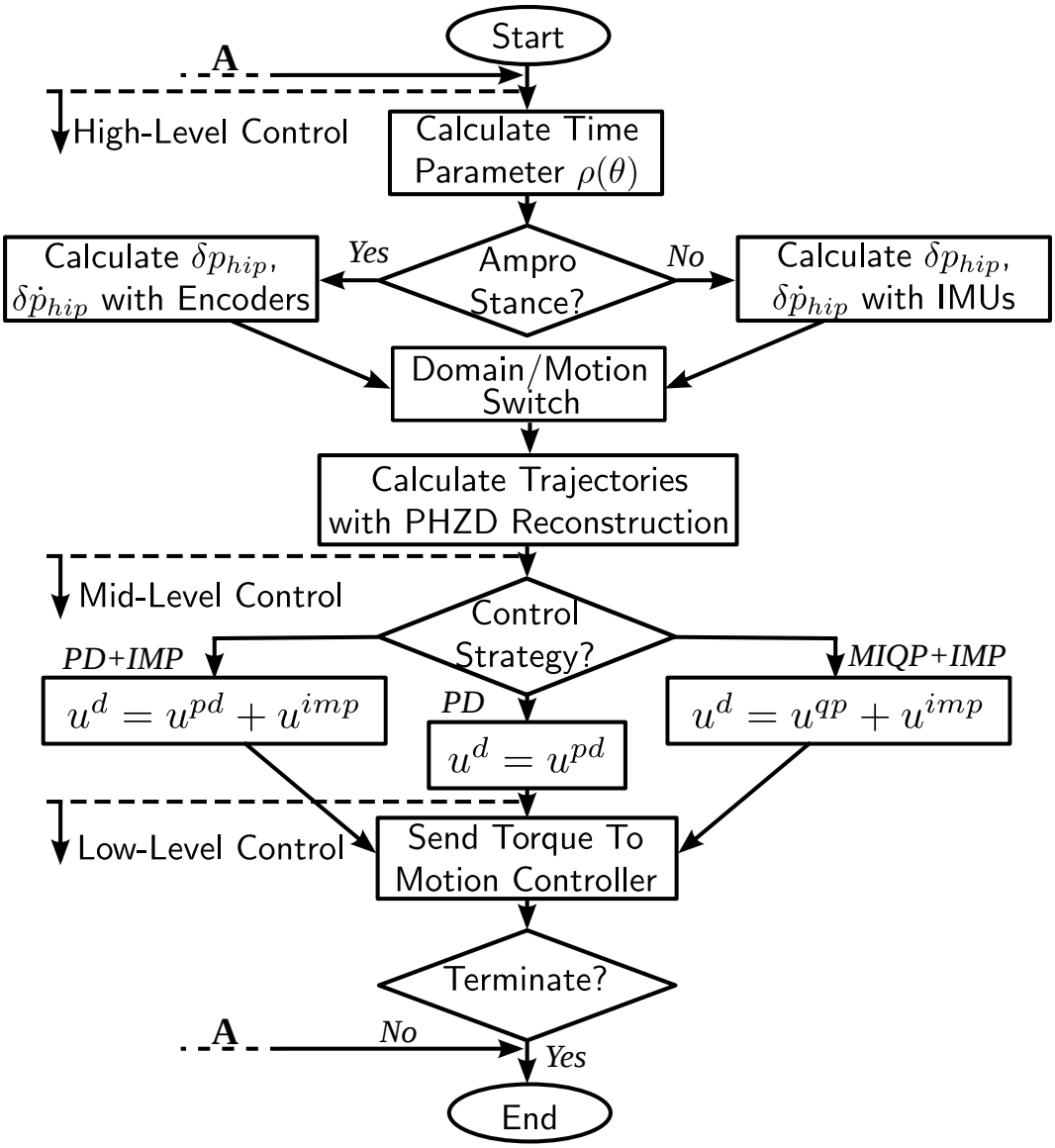

Figure 24: Flow chart of the pseudo-code.

which includes switching to different domains (for example, from hl domain to hs domain) or motion types (for example, level-ground walking or stair climbing) based on specific criteria and computing the desired trajectories for the domain. Both the high-level controller and the mid-level controller of AMPRO1 are coded into C++ packages and run on the Robot Operating System (ROS). The complete code is realized independently with a low-power single-board computer: Beaglebone Black (BBB) at 200 Hz. CAN bus is used as the communication protocol between the BBB and the ELMO. A custom PCB: AMPRO1 board as shown in Figure 25 is designed

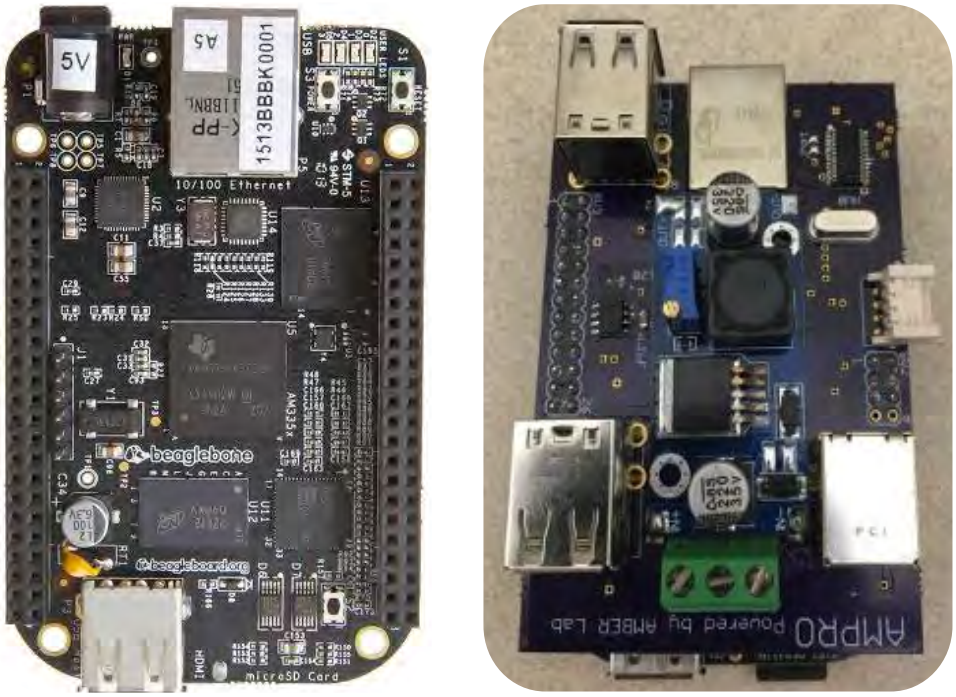

Figure 25: BBB (left) and AMPRO board (right).

specifically using a freeware Eagle to expand functionality of the BBB (including enabling the CAN port).

To provide a point of human-robotic interaction for high-level control, two IMUs are mounted on the shin and thigh of the human leg. An EKF internal model for each IMU, which will be discussed later, is used to obtain relative orientation and velocity for both the knee and ankle. In particular, while the human leg is in stance, IMU readings are utilized to compute the forward hip position ξ_1 and forward hip velocity ξ_2. The desired swing trajectories of the prosthetic can then be calculated accordingly using the PHZD reconstruction method discussed previously in Section 4.2.1. For hardware implementation, one BBB is dedicated to run the EKF algorithms which will be introduced in the following section. The communication to the main BBB which runs the primary code is achieved over a networked crossover cable.

The instrumentation of the human leg with IMUs are not necessary for achieving stable prosthetic walking with the framework in this dissertation. Instead of having a state-base prosthetic swing phase, a time-base swing phase can be implemented without the requirement of the IMUs, which is also a common practice for prosthetic

control as discussed in [81, 112]. However, one of the main benefits with using the IMUs is that the prosthetic leg is able to react to the human body directly. For example, the prosthetic leg can stop if the human stops during walking while the prosthetic leg is in the swing phase. More importantly, with the augmentation of the IMUs, the amputee can start, stop and change the walking cadence easily and smoothly without requiring any extra effort, which, can benefit the prosthetic walking greatly.

6.2 Prosthetic Gait Design

One of the main contributions of this dissertation is the translation of the methodology previously utilized for designing multi-contact walking gaits for the bipedal robot AMBER2 to design walking gaits for prostheses in an automatic fashion. In particular, a multi-domain bipedal hybrid system with anthropomorphic parameters is considered to be a "human" model for the purpose of prosthetic gait design. Based on this model and the reference human locomotion data, the multi-domain optimization (HIO) is implemented to generate a human-like prosthetic gait that (a) yields theoretically provable stability, (b) captures the essential behaviors of healthy human walking, (c) suits the specific test subject wearing the prosthetic device and (d) can be implemented on the prosthetic device directly. The invariant human trajectory is analyzed first, followed by which, the IMU system is introduced briefly. Finally, the detailed implementation of the optimization problem is discussed.

6.2.1 Invariant Human Trajectory

Reproducing the multi-contact behavior of human gaits in prosthetic walking is important for symmetric, natural and efficient walking on an amputee. One obvious problem encountered when designing such a gait is the lack of a nominal gait reference specific to the amputee. Human gait researchers and biomechanists have found that humans share a common pattern of joint trajectories during locomotion [130]. Therefore, a feasible approach is to use the nominal trajectories obtained from healthy subjects as the initial test gait for the amputee. While this is a common practice for

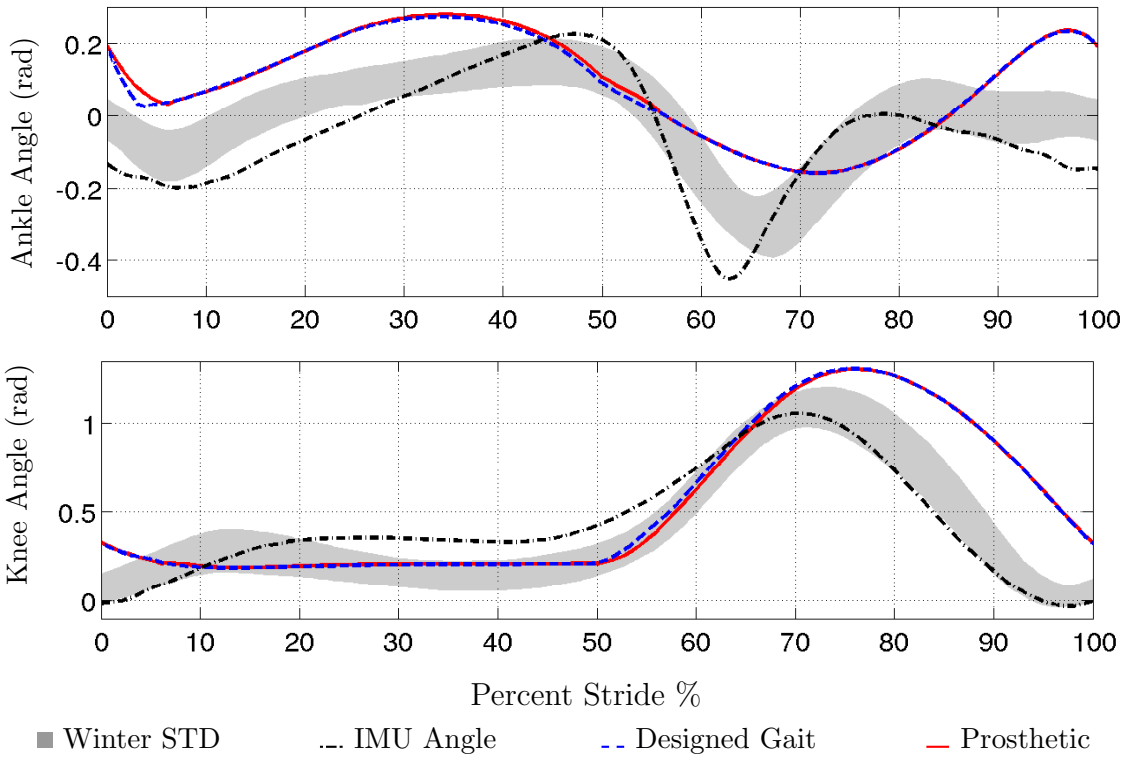

Figure 26: Joint angles for human subject collected with IMUs, the designed prosthetic gait and the simulated prosthetic walking joint trajectories compared to Winter [130]. The trajectories (i.e., Winter data) are used as a comparison to show that the subject is walking with qualitatively human-like trajectories for use as a seed in the trajectory optimization.

prosthesis researchers and clinical physicians [28, 112], this approach requires hand tuning and heuristic experience. This motivates the proposed approach of formulating an optimization problem to formally design a gait for the amputee automatically. Building upon previous work on bipedal robots, we propose a method to utilize the reference gait from an unimpaired subject that has similar anthropomorphic parameters (w.r.t. limb length) to the amputee as the reference for automatic prosthetic gait design.

6.2.2 IMU Motion Capture

There have been many methods proposed for ambulatory measurement of human joint angles. In particular, Luinge and Veltink [78] proposed a Kalman filter which

integrates the 3D angular velocity while applying heading corrections based on accelerometer readings. This approach is prone to integration drift of the gyroscope for systems which need to operate for long durations of time such as prostheses. A more advanced kinematic filtering method was proposed by Roetenberg et al. [100] for the XSens MVN motion capture suit. This approach uses a kinematic model of the individual body segments which is used to update a Kalman filter and provide the positions of each joint and segment of the body. Motion capture systems have also been shown to be effective for robotic teleoperation such as the method proposed by Miller et al. [86] in which an inertial motion capture system was successfully used to teleoperate the NASA Robonaut. This system used a complementary filter to fuse accelerometers, gyroscopes, and magnetometers to estimate poses which were then used to compute an inverse kinematic relationship for pose recreation on the robot.

The algorithm used for motion capture in this work is a planar modification of the model-based Extended Kalman Filter (EKF) first presented by Šlajpah et al. [109]. In this approach, the human extremities are modeled as a kinematic chain built from a location of negligible acceleration. The concept is based on a kinematic relation similar to a series of inverted pendula, where the acceleration of any point B on a rigid body can be determined if the angular velocity, angular acceleration and linear acceleration of other point A on the body are known through the relation:

$$a_B = a_A + \omega \times (\omega \times r_{AB}) + \dot{\omega} \times r_{AB}, \tag{109}$$

where r_{AB} is the distance from point A to point B and ω is the angular velocity of the link. The algorithm used in this work is different in two aspects: the kinematic model of the human legs is assumed to be composed of joints with ranges of motion limited to flexion/extension, and the kinematic chain is built from the hip. Since AMPRO has restricted actuation in solely the saggital plane and because joint variations in the coronal plane are not used in the proposed control approach, only measurements resulting in joint flexion and extension are used in the model update. To express the segment estimation in terms of the available joint mobility of AMPRO, the measurements from the IMUs are projected onto the saggital plane at each time step before

they are passed to the filter. Additionally, we assume that the forward velocity of the hip is constant [143] and that sinusoidal movement of the hip in the vertical direction will yield negligible acceleration in comparison to walking dynamics.

An EKF is instantiated for each segment in the model and updated sequentially along the kinematic chain from the hip. More specifically, the hip joint is instantiated as a base in which the acceleration and angular velocity are zero. Each distal joint in the chain is then treated as a moving base, where the base acceleration and angular velocity are provided by the previous link. Each EKF update estimates the states $x_k = [\omega^S,\ \dot{\omega}^S, q^E,\ \dot{q}^E]^T$, with $\dot{\omega}^S$ the first time derivative of the angular velocity in the segment (S) frame and $\dot{q}^E$ the first time derivative of the earth-frame (E) quaternion. The measurements for each link are $z_k = [\omega_k^S,\ \dot{\omega}_k^S,\ a_k^S]$ with a_k^S the linear acceleration of the link, which is the primary measurement coupled to the previous link. Specifically, the acceleration from the previous joint is used in the estimation model as (109) where a_B is the expected accelerometer reading, and a_A is passed from the previous link. The estimation then proceeds through each joint according to the method detailed in [109].

Finally, the estimated orientations from the multi-body EKFs are then used to extract the joint configuration using each link's quaternion attitude in the global frame ${}^E q$, from which the joint rotations used in the overall model q_j can be found as:

$$q_j = q_P^* \otimes q_D, \tag{110}$$

where q_P^* denotes the quaternion conjugate, $\otimes$ is the quaternion product, q_D is the distal segment orientation and q_P is the proximal segment orientation.

During the experiment, the unimpaired subject was asked to walk along a straight line with a self-selected cadence for several steps. The joint angles and velocities are estimated and collected from the EKF algorithm, and then several steps are averaged to yield their unique trajectories for optimization. These captured trajectories by the IMUs are compared with the nominal human trajectories obtained from Winter's data [130]. The results in Figure 26 indicate that the IMU system is able to capture

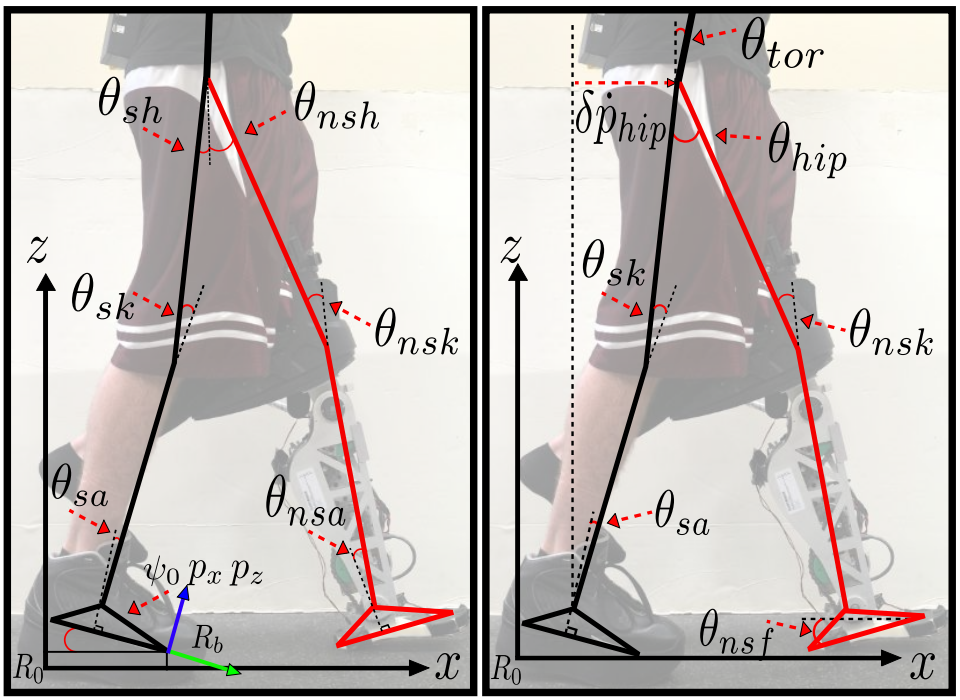

Figure 27: Coordinates (left) and outputs configuration (right) of the multi-contact human-prosthesis robotic model.

the human locomotion trajectory quantitatively.

Note that, we did not perform a multi-subject validation of this estimation algorithm as it is not central to the topic of this dissertation. Since the authors in [109] validated the 3D filtering method, this work is assuming that a planar projection of the method will capture the information we seek accurately. Specifically, the captured data of our single user is not statistically relevant for the purposes of claiming a validation of the method. Instead, the aim of Figure 26 is to show that the saggital plane trajectories are qualitatively human-like through a comparison of the data to a widely used dataset [130]; therefore, the captured data can be used as a reasonable seed for the prosthetic gait design.

6.2.3 Optimization for Prosthetic Gait Design

For the purpose of prosthetic gait design, we consider a multi-domain bipedal hybrid system with anthropomorphic parameters to be a "human" model. Similar as the model of AMBER2, the multi-contact amputee-prosthesis system is modeled as a

seven link bipedal robot with 3 domains. The definition of model configuration and outputs are shown in Figure 27. The high-level hybrid system can be constructed similarly as the discussion of AMBER2. For the gait design optimization, the PHZD constraints are considered also with the goal to generate a stable gait. Particularly, the three sets of PHZD constraints can be stated implicitly as:

$$\Delta_{v^+\to v^i}(S_{v^+\to v^i} \cap \mathbf{PZ}_{\alpha_{v^+}}) \subseteq \mathbf{PZ}_{\alpha_{v^i}}, \tag{PHZD1}$$

$$\Delta_{v^i\to v^-}(S_{v^i\to v^-} \cap \mathbf{PZ}_{\alpha_{v^i}}) \subseteq \mathbf{PZ}_{\alpha_{v^-}}, \tag{PHZD2}$$

$$\Delta_{v^-\to v^+}(S_{v^-\to v^+} \cap \mathbf{PZ}_{\alpha_{v^-}}) \subseteq \mathbf{PZ}_{\alpha_{v^+}}. \tag{PHZD3}$$

The detailed construction of these constraints is similar to as the discussion of AMBER2 in Section 4.2.

Enforcing the PHZD constraints above, a multi-domain optimization is utilized to design stable human-like prosthetic gaits automatically. For the system of a lower-limb prosthesis interacting with humans in a safety critical fashion, physical constraints incorporating (a) hardware limits (torque limits and joint movement range), (b) safety concern (foot clearance and impact velocity) and (c) user comfort (user preferred trajectory profile) are explicitly considered during the gait design optimization. Note that, the physical constraints can be constructed similarly as the discussion of AMBER2 in Section 4.2. These specifications yield the optimization problem subject to both the PHZD constraints and the physical constraints as follows:

$$\begin{aligned} \alpha^* = \underset{\alpha\in\mathbb{R}^{43}}{\text{argmin}} \ & \text{Cost}_{\text{HD}}(\alpha) \\ \text{s.t} \quad & \text{(PHZD1)} - \text{(PHZD3)}, \\ & \text{Physical Constraints}, \end{aligned} \tag{111}$$

where the cost function is the least-square-fit error between the IMU recorded unimpaired human reference data and the ECWF representations in (20). The end result of this optimization problem is the outputs parameter set α that renders an optimal (w.r.t. torque, foot clearance, joint position and velocity) and provably stable subject-like multi-contact prosthetic gait, which at the same time can be implemented

directly on the prosthetic device. The desired joint angles and angular velocities for the prosthetic device can be obtained via the technique of PHZD reconstruction by only knowing the actual forward hip position δp_{hip} and the corresponding hip velocity $\delta \dot{p}_{hip}$, which correspond to ξ_1 and ξ_2, respectively. In particular, the hip position δp_{hip} is used for the desired position calculation and the $\delta \dot{p}_{hip}$ will be used for desired velocity calculation based on the derivation of (20) and (22). With this PHZD reconstruction methodology, the designed trajectories of both the ankle and knee joint, shown in Figure 26, are obtained and compared with the nominal human locomotion data obtained from Winter [130]. Both the knee and ankle angles have a similar pattern as the nominal locomotion data.

Utilizing the joint trajectories of an unimpaired subject as reference, this optimization problem is subject to both the PHZD and physical constraints such that the generated gait is smooth, user-friendly and applicable for direct implementation on the prosthetic devices. While there is no clear evidence showing that a particular gait is more comfortable or performant, the goal of the proposed methodology is that with the automation of the gait generation, hand tuning can potentially be reduced or done in a more high-level manner. For example, for the experimental walking trajectories used in this work, the initial gait was designed with more stance knee movement, i.e., the stance knee angle was more human-like with bigger knee bent. However, the test subject prefers less stance knee movement, which was reported to feel more comfortable and safer (large stance knee movement may increase the possibility of buckling during stance phase for some extreme situations). Therefore, this preference can be easily added into the optimization, the end result of which is the stance knee angle being more flat compared to the nominal human trajectory (see Figure 26).

6.3 Preliminary Testings with Flat-Foot Assumption

In order to verify the proposed methodology, this dissertation first considered a simple case by restricting the subject walking with flat-foot. Importantly, there is only one domain for flat-foot walking, which allows us to focus more on the implementation

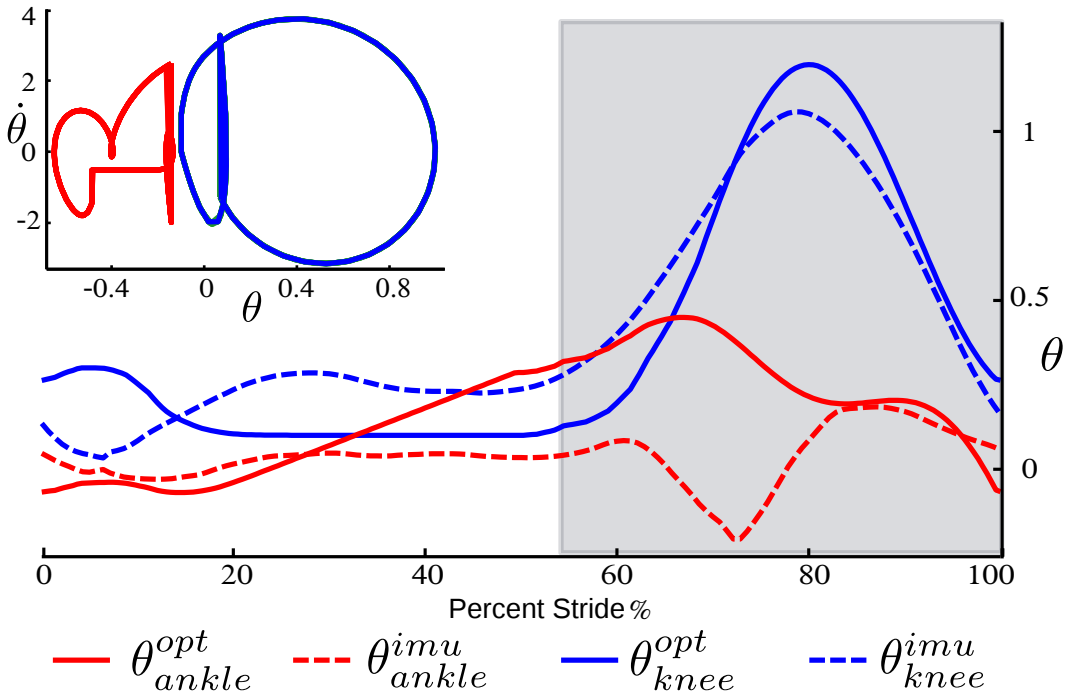

Figure 28: Limit cycles for both the ankle and knee joints of flat-footed walking (upper left) and the comparison between the collected healthy human flat-foot walking data (IMU) and the joint angles optimized via (HIO); the shadowed region represents the swing phase.

without worrying complexities brought by multi-domain gaits generation or multi-domain switches. Flat-foot walking is a simplification of human walking. We realize that it introduces limitations on both the procedure of reference trajectory recording and the prosthetic gait optimization problem. However, it captures the essential behavior of human walking that suits the preliminary testing purposes. Multi-contact gaits will be addressed in the following section.

In particular, the IMU motion capture system discussed above is utilized to collect the flat-foot trajectory of a healthy subject. Using this trajectory set as the reference, and subject to both the PHZD constraints and physical constraints, the human-inspired optimization problem is leveraged to design a stable gait for the specific amputee subject. Note that, in the context of bipedal walking, a mathematically stable limit cycle implies stable walking. The limit cycles pictured in Figure 28 are closed, indicating that they result in stable walking. The optimized trajectories along with the IMU motion capture data are also shown in Figure 28. We can see that

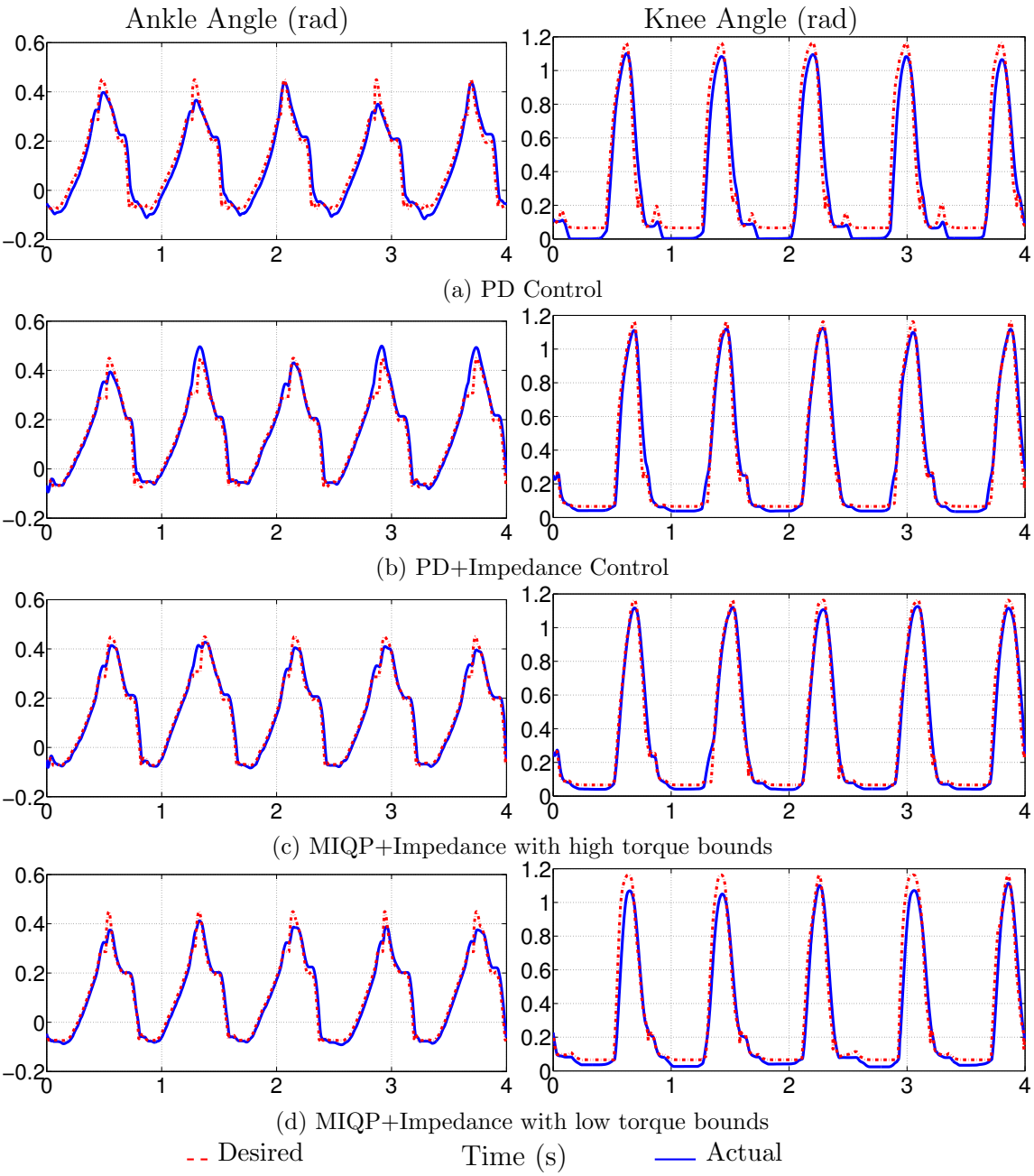

Figure 29: Tracking comparison for different controllers.

the optimized knee angle follows a similar pattern as the healthy subject. However, the optimized ankle angle is different from the reference human trajectory especially in the late stance and swing phase. This mismatch is mainly due to the flat-foot walking assumption considered in this preliminary work. This assumption constrains the reference subject to walk cautiously with a flatter ankle pattern, while on the other hand, the optimization problem could achieve a faster walking speed with more

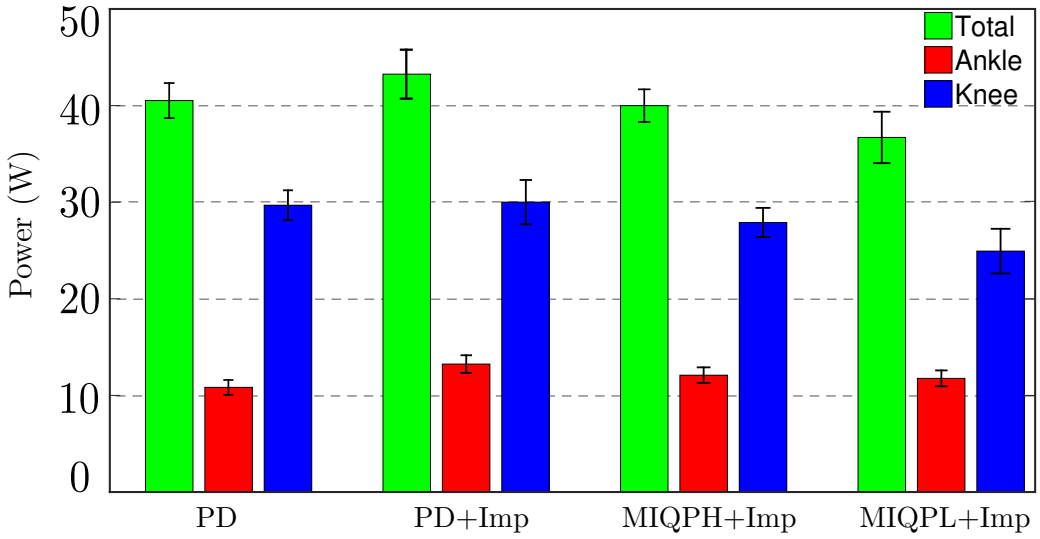

Figure 30: Net mechanical power comparison for the prosthetic joints of one flat-foot step (including stance phase and swing phase) averaged over 32 steps with using different controllers.

dynamic ankle trajectory.

6.3.1 Experiment Results

Before the implementation of MIQP+Impedance control on the prosthesis, a proportional-derivative (PD) controller:

$$\mu^{pd} = -K_p(\theta - \theta_d(\xi_1)) - K_d(\dot{\theta} - \dot{\theta}_d(\xi_1, \xi_2)), \tag{112}$$

is first realized to track the designed trajectories to achieve stable walking. The PD gains $K_p \in \mathbb{R}^{2\times 2}$ and $K_d \in \mathbb{R}^{2\times 2}$ are tuned based on the feedback from the test subject. Walking trials were performed on a treadmill providing a constant speed of 1.3 mph. With the experimental data of walking with PD control in hand, the impedance parameters are estimated using the least-square-error fitting method. We then apply impedance control as the feed-forward term while using the MIQP control as the feedback term to track the desired joint trajectories. In particular, for the first round of testing, we set both the torque bounds μ^{qp}_{MAX} and μ_{MAX} to be 40 Nm which is determined based on the PD walking experiment data. In order to show the torque optimality of the proposed novel controller, the torque bounds μ^{qp}_{MAX} and μ_{MAX} are reduced to be 20 Nm for the second round of testing. While the novel control contains

both the feedback term and feed-forward term, we also compare it with an augmented control strategy, PD+Impedance:

$$\mu^d = \mu^{pd} + \mu^{imp}, \tag{113}$$

which also includes impedance control as a feed-forward term. In order to show the tracking performance visually, the tracking results of five consecutive steps using different controllers are plotted in a comparative way in Figure 29. For further statistical verification purposes, a total of 32 consecutive steps are considered to compute the performance results for each of the considered controllers. The averaged one step mechanical power consumption along with the corresponding one standard deviation of the prosthetic device is shown in Figure 30. More detailed performance comparisons are listed in the Table 4. The gait tiles of the level walking using the proposed optimization-based controller along with the simulated gaits are shown in Figure 31.

6.3.2 Discussion

A joint tracking comparison is provided in Figure 29 for various controllers on the knee and ankle joints of AMPRO1. It is evident that the tracking performance of both the ankle and the knee are exceptionally good for MIQP+Impedance control. The tracking results with lower torque bounds are shown in Figure 29c. While the tracking performance is not as good as the tracking with higher torque bounds, it is better than using PD control, with a 20.9% improvement on rms error based over 32 steps. More importantly, this improved tracking is achieved with lower torque and less total energy consumption when compared to PD control (9.4% improvement). Similar performance can also be found of MIQPH+Impedance control when comparing to PD+Impe-dance control with less than 5% tracking lose but $3.26W$ (7.5%) reduction on power, which can be seen in Figure 30 and Table 4.

To illustrate the overall control performance more clearly, the experimental results (including tracking errors, maximum torque requirement and average net power consumption) of 32 consecutive steps are listed in Table 4. In particular, the best

Figure 31: Gait tile comparison between the treadmill experimental walking and the simulated prosthetic walking.

performances are highlighted in the table with a * superscript, from which we can see that with the exception of the *rms* knee error (using PD+Impedance) and the minimum ankle power (using PD control), all of the best performances are achieved with the MIQP+Impedance controllers. The low power requirements of the PD controlled ankle are also correlated with the highest tracking errors, indicating that low fidelity tracking performance may be allowing passive motion of the device. To summarize, the experimental results indicate that the MIQP+Impedance controller has the most balanced performance between tracking and power requirements.

The resulting powered prosthetic joint trajectories using the proposed optimization-based controller and the PD controller are compared with the IMUs collected healthy human locomotion data and the passive prosthetic walking data (the amputee walking

with a passive device) in Figure 32. When compared to passive prosthetic walking, we can see that the ankle movement of the powered device is much more dynamic than that of the passive device. In particular, the ankle on the passive device is very rigid and posseses a very small movement range. On the other hand, the powered prosthetic ankle can provide a more dynamic panarflexion throughout the stance phase and dorsiflexion during the swing phase. The human-likeness of the ankle joint will be improved in the future work with multi-contact walking. For the knee joint, we can see that both the passive device and powered device with different controllers have a similar swing pattern compared to the healthy human walking. However, for the stance knee trajectory, both the passive device and the powered device with PD control tend to lock the knee at the last portion of the stance phase. Note that, for both the passive device and powered device, a safety stop is added at the knee joint to prevent hyper-extension, where we define as knee-lock if the knee joint reaches this position. During data collecting, we calibrate this knee-lock position as zero reference point in particular. Alternatively, the powered device with MIQP+Impedance control has better performance with bigger knee bending and no knee locking. A slight delay was also noticed for the powered prosthetic walking when switching from stance phase to swing phase. This was caused by the delay of the force sensor recovering from the loaded status during the stance phase, which will be fixed by considering a load cell in the future design.

Table 4: Experiment Results Comparison of AMPRO1 Using Different Controllers over 32 Steps during Flat-Foot Walking.

Control		e_{rms}	e_{max}	σ_{rms}^{std}	$\tau_{max}[Nm]$	$P[W]$
PD	**Ankle**	0.0388	0.1700	0.0027*	24.749	10.834*
	Knee	0.1059	0.3957	0.0179	41.275	29.686
PD+	**Ankle**	0.0325	0.1860	0.0070	23.787	13.247
Imp	**Knee**	0.0546*	0.3693	0.0148	38.921	30.007
MIQPL	**Ankle**	0.0290	0.1290*	0.0033	19.916*	11.767
+Imp	**Knee**	0.0854	0.3822	0.0155*	20.027*	24.937*
MIQPH	**Ankle**	0.0261*	0.1498	0.0045	22.351	12.094
+Imp	**Knee**	0.0657	0.3002*	0.0213	36.221	27.902

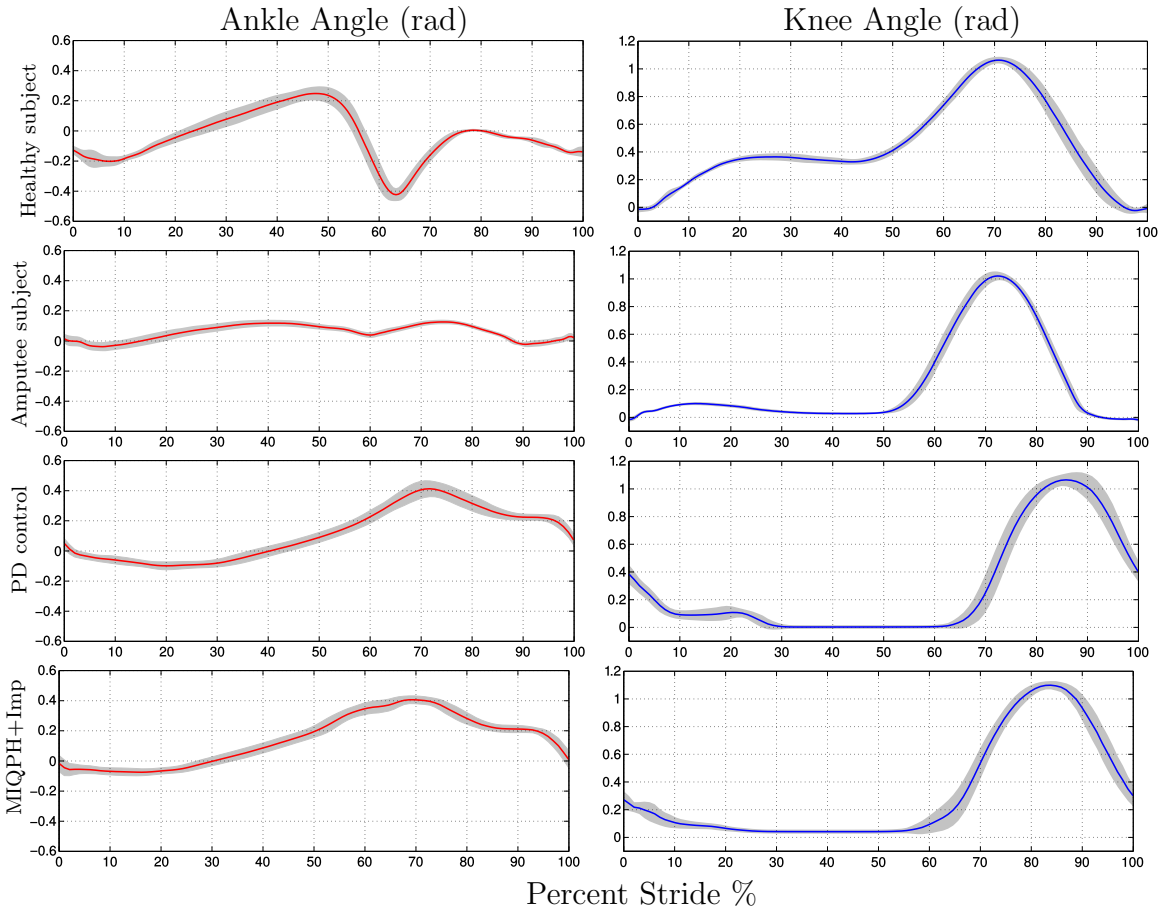

Figure 32: Comparisons of both the ankle and knee joint angles of healthy human walking, passive prosthetic walking and powered prosthetic walking with PD control and MIQPH+Impedance control. The gray area represents one standard deviation of each corresponding trajectory for 32 steps.

6.3.3 Outdoor Testing with An Unimpaired Subject

As an additional form of testing, AMPRO1 was taken out of the lab to walk in various environments with an unimpaired subject. In particular, two tests were performed at the student Recreation Center of Texas A&M University. The first test was carried out using the MIQP+Impedance control with low torque bounds; the test subject was able to walk 30 mins continuously with a total travel distance of 3/4 miles. Testing was prematurely terminated due to an electrical failure on the shin IMU sensor. The battery voltage drop was monitored to estimate the power cost. The voltage drop during the course using the MIQP+Impedance controller for

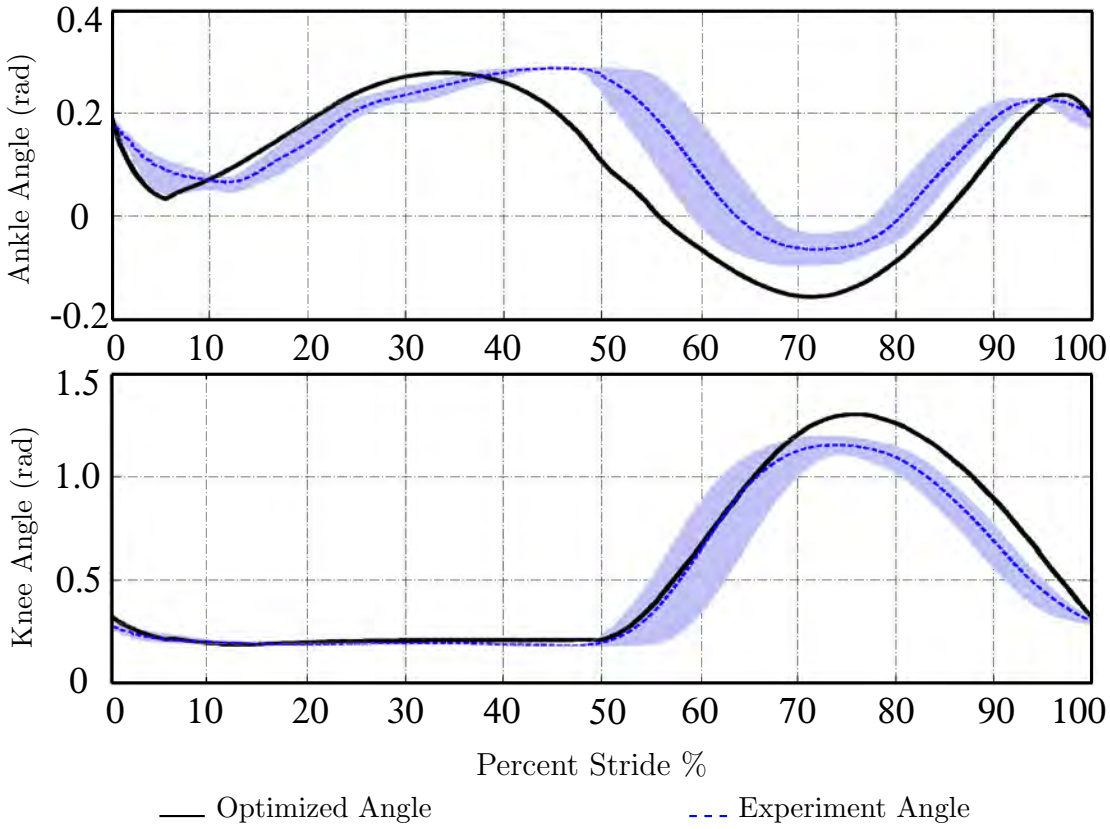

Figure 33: Averaged experimental joint angles compared with the designed joint angles obtained from optimization. Grey area is the standard deviation of the experiment results over 10 steps.

the continuous walking test was 1 V. For comparison purposes, another test was performed employing PD control. The subject successfully finished 1 mile in 40 mins (the average walking speed was similar to the speed of using MIQP+Impedance control) with 1.5 V voltage drop over the course of the continuous walking experiment. From the voltage drop comparison, we can conclude that the MIQP+Impedance controller required less power during the test of walking freely. The experiment video is shown in [2].

6.4 Multi-Contact Prosthetic Locomotion

With the successful implementation experience gained from realizing flat-foot prosthetic walking, we are now ready for implementing the prosthetic gaits designed in Section 6.2 to realize multi-contact prosthetic walking.

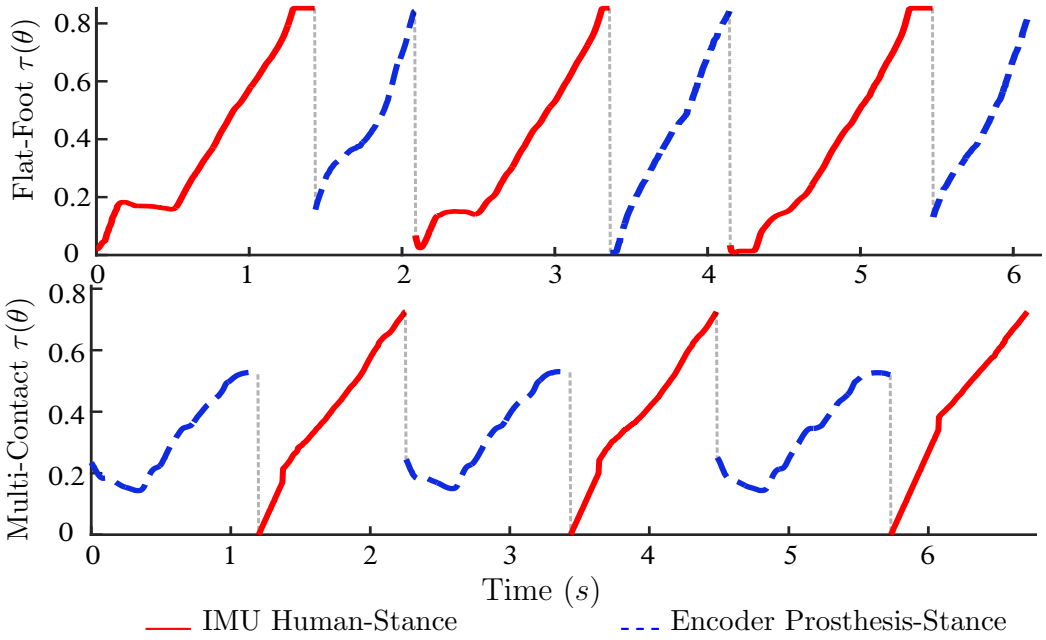

Figure 34: Phase variable $\tau(\theta)$ comparisons between Experimental flat-foot and multi-contact prosthetic walking over 6 steps. The red solid lines represent $\tau(\theta)$ computed by the IMUs during human-stance phase. The blue dash lines represent $\tau(\theta)$ computed by the encoders during prosthesis-stance phase. x-axis is the real-time each step takes.

6.4.1 Domain Switching

As discussed in the implementation of AMBER2, the outputs are synchronized by the phase variable $\tau(\theta)$ (22), by knowing which the desired trajectory can be computed using the PHZD reconstruction strategy as discussed in Chapter 4 (details can also be found in [53, 73, 139]). For the multi-contact walking with multiple domains, different sets of outputs are considered for each domain. Therefore, the desired trajectory needs to be calculated according to the current domain [139]. During the prosthetic-stance phase, the domain switch can be achieved using the two force sensors mounted on the heel and toe of the prosthetic foot. Because the human foot is not instrumented, the domain switch is estimated using the phase variable. In particular, the specific phase variable $\tau(\theta)$, at which moment the domain switches, is recorded during the gait design optimization. These values are then utilized as the thresholds to determine the domain switch during human-stance phase in the experiment.

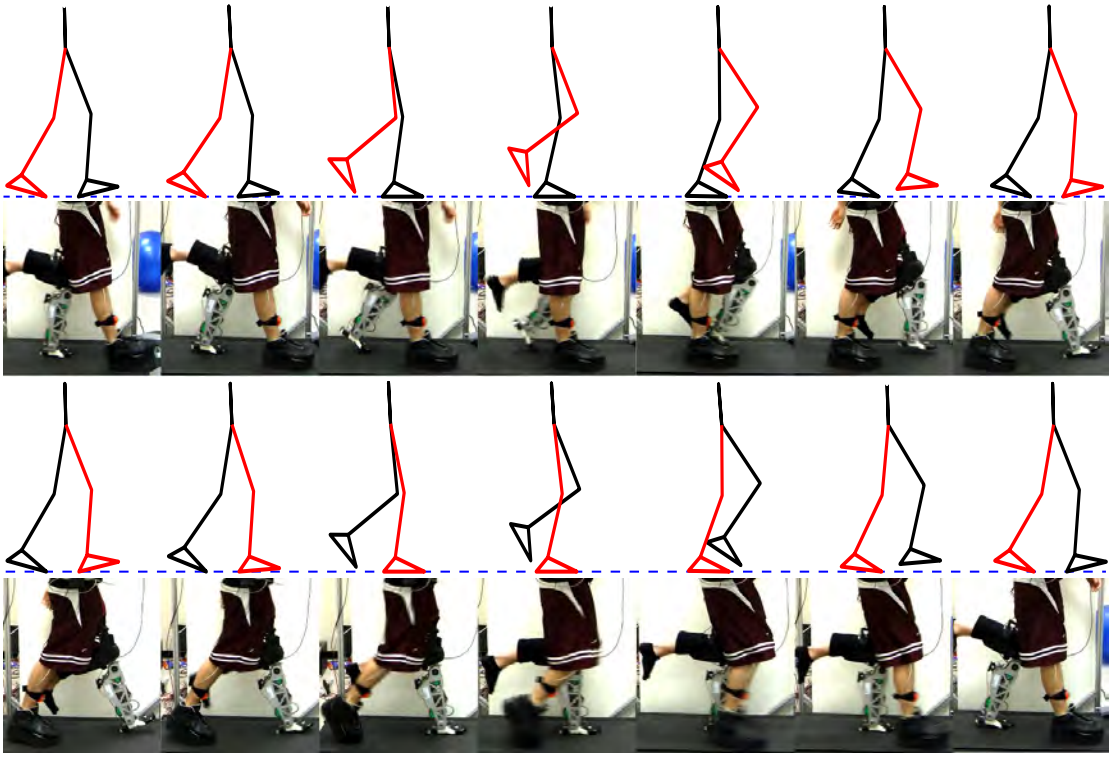

Figure 35: Gait tile comparisons between the simulated and the experimental prosthetic walking using MIQP+Imp control.

6.4.2 Experiment Implementation

Walking trials were performed on a treadmill providing a constant speed of 1.3 mph. A PD controller μ^{pd} is first implemented to achieve stable walking for the purpose of impedance parameter estimation. With the impedance parameters in hand, we apply impedance control μ^{imp} as the feed-forward term while using the MIQP control μ^{qp} as the feedback term to track the desired joint trajectories. The resulting joint trajectories (averaged over 10 steps) are compared with the designed gait in Figure 33, showing that the obtained prosthetic walking is able to realize the designed gait successfully and shares a similar pattern as the healthy human locomotion. The experimental multi-contact phase variable $\tau(\theta)$ is plotted in Figure 34 with the comparison to the flat-foot walking. The experiment gait tiles of the multi-contact level-ground walking using the proposed optimization-based controller along with the simulated prosthetic walking are shown in Figure 35. A video of the resulting multi-contact walking can be seen at [3].

For the purpose of control performance comparison, the PD+Impedance is tested in the experiment. Note that, as mentioned in Section 6.3, the torque bounds can be considered inside the quadratic program, therefore yielding the resulted controller (point-wise) optimally satisfying the torque bounds. In particular, two rounds of test with different torque bounds—100 Nm for high torque bounds (MIQPH+Imp) and 40 Nm for low torque bounds (MIQPL+Imp)—are tested to verify the torque optimality. The tracking rms errors along with the average power consumption of one step using different controllers are compared in Figure 36.

One practical problem during testing is that the subject walking with prosthetic devices will not have the same step posture every step, i.e., each step will be slightly different. Also, asymmetry in the gait in the form of short stepping on one leg can cause variations in the starting $\tau(\theta)$. Therefore, the phase variables $\tau(\theta)$ computed from the IMUs and encoders will not evolve exactly as predefined—from 0 to $\tau_{max}(\theta)$ (which is obtained based on the chosen gait). During the human-stance phase, non-zero initial $\tau(\theta)$ will cause problems with yielding a non-smooth prosthetic-swing trajectory, i.e., there will be jumps of the desired position and velocity at the transition from prosthetic-stance to prosthetic-swing. To overcome this problem in the testing, a time-based $\tau(\theta)$ was used at the beginning of the prosthetic-swing phase, in which way the $\tau(\theta)$ will always start from zero to guarantee the smooth transition. Then the $\tau(\theta)$ will switch to state-based when the state-based value is very close (within 0.02 difference) to the time-based value. During the prosthetic-stance phase, due to a flatter pattern of the trajectory (i.e., both the movement ranges and velocities of both the knee and angle joints are small), the non-zero initial $\tau(\theta)$ was not found to be a problem that affects the overall performance during the prosthetic-stance phase.

6.4.3 Discussion

The experimental results will be analyzed in this section via several comparisons. Different controllers for multi-contact walking will be studied first. Then the multi-contact walking will be compared with flat-foot prosthetic walking showing improvements on several aspects such as gait symmetry and foot push.

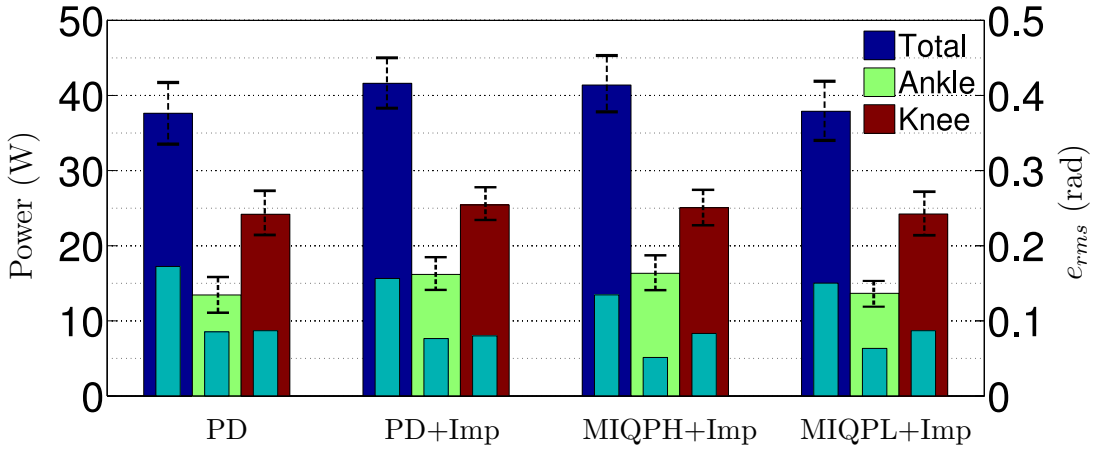

Figure 36: Net power with one standard deviation (thick bar) and *rms* tracking error (thin bar) comparisons of the prosthetic joints of one multi-contact step (including stance phase and swing phase) with using different control methods as averaged over 10 steps.

6.4.3.1 Comparison of Different Controllers

The tracking results plotted in Figure 36 show that the tracking performances of both the ankle and knee are best with MIQPH+Imp control. In particular, we found that with improved tracking performance (12.9% improvement), the MIQPL+Impedance has similar energy consumption (less than 1% difference) when compared with PD control. Similarly, the MIQPH+Impedance outperforms PD+Impedance control in tracking performance (13.9% improvement) while requiring similar power (less than 1% difference). Note that, traditional control approaches (e.g. variable impedance control) to powered prostheses rely on the extensive tuning of control parameters in order to achieve successful operation of the device for a particular subject. Alternatively, we take the position tracking path with the goal of automating both gait generation and controller design for different subjects and various locomotion types. We believe that a well designed gait (w.r.t power, torque, velocity etc) is the first step toward benefiting the amputee when clinical expertise is also considered in future work. More importantly, this process can be done iteratively in an automatic way such that the performance (e.g., comfortability) can be improved with the feedback from the test subjects. Considering the fact that the proposed control method is based on position tracking, the tracking performance is one of the key

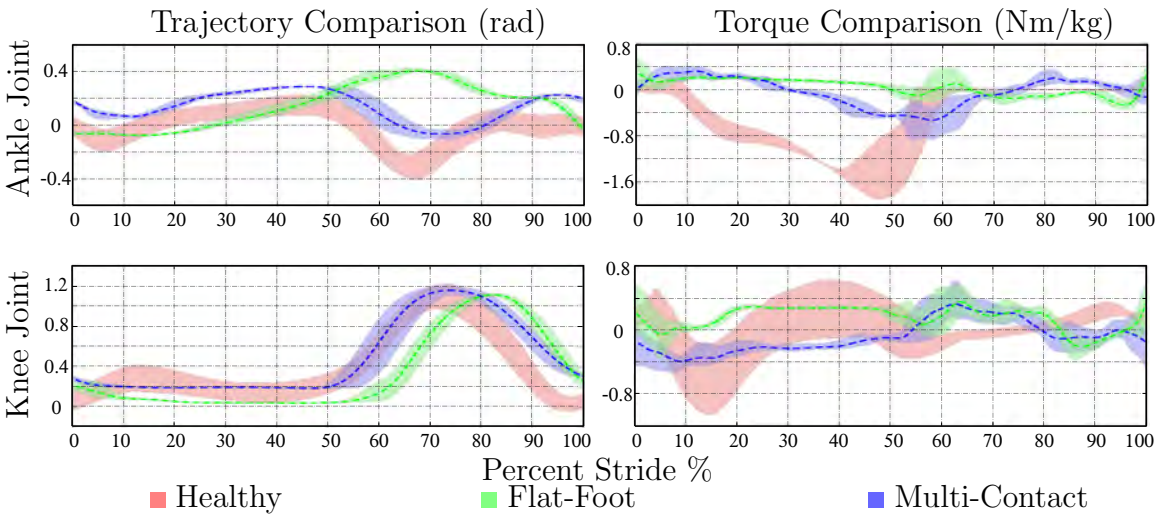

Figure 37: Comparisons of the joint angles and torques of the healthy human walking (obtained from [130]), the experiment flat-foot and multi-contact prosthetic walking. The shade area is the one standard deviation of corresponding data.

aspects for performance comparison. Therefore, to summarize, we can conclude that the MIQP+Impedance controller has a more balanced performance between tracking and power requirements.

6.4.3.2 Comparison With Flat-Foot Walking

To show the improvements of this multi-contact prosthetic walking, we compare it to the flat-foot prosthetic walking explicitly. One important improvement can be seen from Figure 34 by comparing the phase duration symmetry between the multi-contact walking and the flat-foot walking. In particular, during the flat-foot walking, the prosthetic-stance phase duration is $0.65s$, which is much shorter than the $1.33s$ human-stance phase duration (averaged over 5 steps), i.e., the gait is asymmetric w.r.t the phase duration. On the other hand, for the multi-contact walking, the averaged (over 5 steps) prosthetic-stance phase duration is very close to the human-stance phase duration with the time being $1.28s$ and $1.02s$, respectively. Therefore, the multi-contact walking has a much better phase duration symmetry performance than the flat-foot walking.

Due to the flat-foot constraint, the prosthetic ankle movement is limited, therefore yielding a less human-like ankle trajectory. In this work, we explicitly compare the resulting multi-contact joint trajectories with the flat-foot walking along with the

collected unimpaired human locomotion data in Figure 37. From this comparison, we can see that the multi-contact ankle angle has a more human-like curve pattern as the healthy human ankle. The knee trajectory also has more human-like features such as a longer swing phase duration and a bigger stance knee bend when compared to the flat-foot knee trajectory.

Additionally, the most important improvement is achieved with the ankle joint kinetically. The human ankle plays an important role in progressing forward smoothly and efficiently during the stance phase [94]. In particular, the ankle stores the elastic energy in mid-stance phase, which will be utilized to propel the body forward and upward during the foot push off phase [27]. The ankle torque comparison shown in Figure 37 indicates that the ankle joint in multi-contact walking follows a closer pattern of human walking[1], which is not seen in the flat-foot walking. More importantly, the user also reported a significant foot push off from the prosthetic device to help propel forward, which is lacking during the flat-foot walking.

Remark. Note that, human-likeness is not the only requirement of the prosthetic gait generation procedure. User feedback such as foot push at the end of stance phase is also a major consideration during the optimization. Therefore, this dissertation doesn't claim that a gait is better if it is more human-like only. Proposing a common standard to qualify a better prosthetic gait or controller should be an emerging topic for the area of both robotic control and biomechanical research.

6.5 Motion Transition with Neural Networks

Another fundamental advantage of the powered prostheses, when compared to the passive ones, is that the powered devices are capable of interacting with the user in a smart and natural way, while passive devices can only assist the user with a predefined routine, i.e., either bear the weight during the stance phase or bounce forward to finish the swing phase. Therefore, in order to realize the potential of powered prostheses,

[1]Nominal human walking speed is 3 mph, which is much faster than the walking speed considered in this experiment. This may be the reason the ankle push torque for this experiment is smaller than the nominal human data from Winter.

an intention interface is necessary to allow the users to control the device through different motion behaviors, i.e., switching between different motion primitives. Proposed approaches include using mechanical triggers or compensatory body movements [62]. However, more natural and smooth motion switching strategies are found to be when utilizing pattern recognition algorithms. With using mechanical sensor data, the intent recognition algorithms are realized in [121] with a maximum $500ms$ delay and in [136] to achieve transitions between 5 modes with over 93.7% accuracy. Combining residual limb electromyography (EMG) signals and the mechanical sensor information, the method in [58] is able to transition between 5 motion primitives with accuracies above 95%.

Motivated by the goal of making the proposed framework practically applicable to prosthesis users, the work in this dissertation proposed a simple, yet effective motion intent recognition algorithm using a neural network classifier. Exploiting the advantages of an instrumented healthy leg and a switch-score scheme, the method is able to accomplish motion switches between 3 motion primitives (including standing, level walking and stair ascent) naturally with minimum delay. More importantly, for one switch mode, the total time cost from static database training to real-time implementation is less than 30 minutes including minimum tuning on the switch-score scheme. The motion intent algorithm is able to predict the motion transition with 1 failure during the total of 56 switch tests, i.e., the accuracy is above 98%.

6.5.1 High-Level Intent Recognition

The intend recognition is realized using a pattern recognizer that combines the neural network models for classification and a switch-score scheme for on-line switching, which will be briefly introduced in this section.

6.5.1.1 Neural Network Classification

Neural network has been a popular data-driven self-adaptive classification algorithm for nonlinear models [137]. Mature commercial algorithms are available for fast application, which is one of the reasons that the neural network model is chosen

as the classification method for this work. The tan sigmoid is selected as the active function of the neural network. In particular, for the three motion primitives considered in this paper—standing (SD), level walking (LW) and stair ascent (SA)—the following motion transitions are considered for these primitives: the switch from LW to SD, from SA to SD and from SD to LW or SA. All the models will be trained with separate databases; this will be discussed in detail in the following.

6.5.1.2 Switch-Score Scheme

The confidence of the switching algorithm can be greatly improved by adopting a switch-score scheme. In particular, the switch-score scheme includes two steps. For the first step, the phase variable (22), i.e., the forward hip position, is used as a threshold to trigger the motion intent recognition algorithm. For example, the transition from SD to LW or SA will be started only if the hip position is greater than zero. Once the motion switch model is triggered, a switch-score for the model will add up if a particular motion is detected continuously. The motion primitive will switch when the switch-score reaches a threshold and also the phase variable is satisfied. Note that, this strategy both saves computation time (since the intent recognition algorithm runs only when a specific condition is satisfied) and increases the classification accuracy (because the target motion is checked constantly for a customized timing window to guarantee the transition is correct).

6.5.2 Experiment Implementation

For experimentally implementing the proposed motion transition strategy, additional two controllers for standing and stair climbing are introduced. The neural network model are trained off-line. The experimental results show successful automatic motion transitions among standing, level walking and stair climbing.

6.5.2.1 Adaptive Standing Controller

A time-based PD controller with adaptive gains is utilized for the control of the standing mode. For the comfort of the user, it is important to allow the users to adjust the gesture, i.e., the joint angles, slightly while in the standing mode. Therefore,

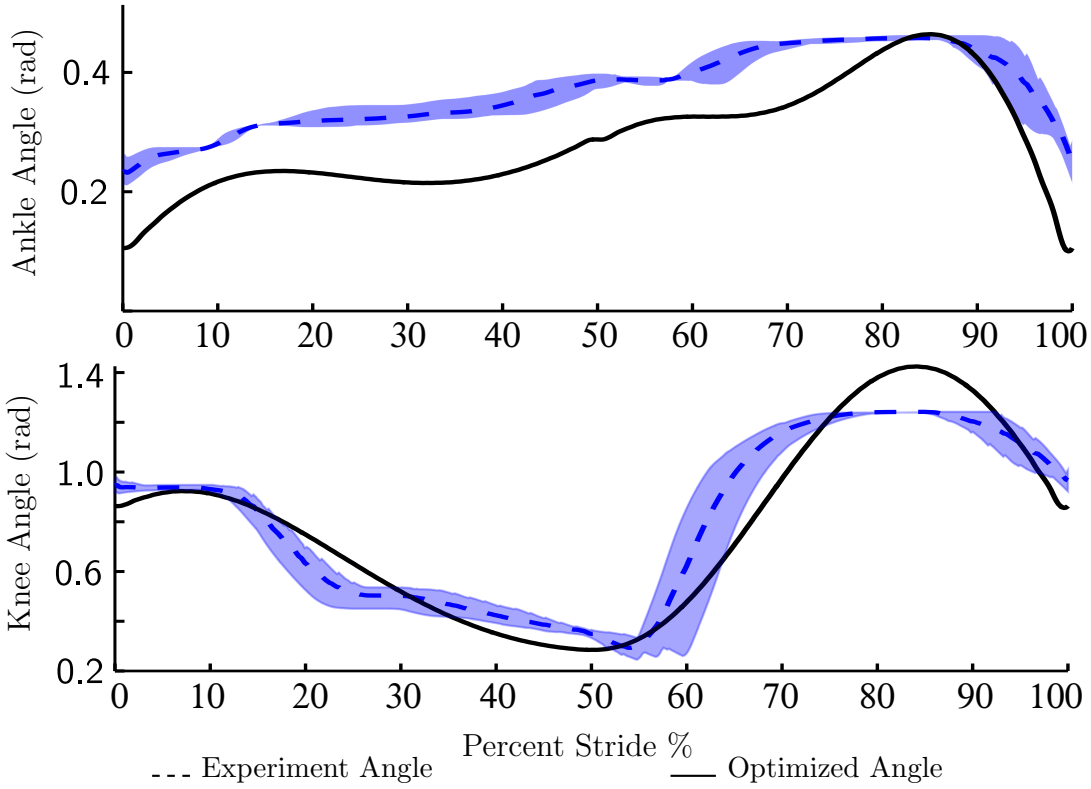

Figure 38: Averaged experimental joint angles of stair climbing compared with the designed joint angles obtained from optimization. Grey area is the one standard deviation of the experiment results.

instead of using fixed gains to restrict the joints to a specific position (e.g., zero position), we apply an adaptive gain schedule for the PD controller. In particular, both the knee and ankle are allowed to move within a small range. The initial PD gains are small when the joint angles are close to the zero positions and will increase exponentially based on the offset when the joint angles approach the joint angle limits, therefore, preventing falling. With this methodology, the user reports a more comfortable and natural standing gesture than using fixed PD gains.

6.5.2.2 Prosthetic Stair Ascending

Similarly as designing level walking gaits, the IMUs system was utilized to collect stair climbing reference data. During the experiments, the subject was asked to walk along a straight line or ascend a staircase (with 10 cm stair height). With the reference trajectory in hand, the same optimization problem is utilized to design stair ascending

gaits for the prosthetic. In the experiments, the MIQP+Impedance control was used to track the designed trajectories. The resulting joint trajectories are averaged and compared with the designed joint angles as shown in Figure 38, from which we can see that the actual prosthetic walking can replicate the designed trajectory very well.

6.5.2.3 Neural Network Model Training

To train the neural network models properly, a database of the mechanical sensor data from both the healthy leg and the prosthetic leg, via IMUs and encoders, respectively, are collected. During the database collection experiment, the test subject was asked to perform ten trials for each task, which include transitions from SD to LW, from LW to SD, from SD to SA and from SA to SD. The data was sampled at 200 Hz, which is the same as the frequency of real-time control implementation. The motion primitive labeling process is supervised by a knee angle threshold of the healthy human leg. In particular, when the swing knee angle is smaller than the threshold, the data is considered to be source motion primitive of the transition. Otherwise, the data is labeled as the target motion primitive of the transition. With the labeled database, the neural network models are trained with the guidance of Occam's Razor principle [137]. With the guarantee that performance is similar between different candidate models, the simplest model is chosen in order to avoid over-fitting. In particular, all the finalized three models are chosen to have only one hidden layer. For the two-class classification models, 4 hidden neurons are used. For the three-class classification model, a total number of 10 hidden neurons is considered. The trained models are then used for real-time motion recognition in the high-level control. The real-time implementation of the switch-score are first estimated from the static training data set and then slightly tunned based on the feedback of the user during experimentation.

6.5.2.4 Motion Transition Implementation

By leveraging the similar methodology of translating robotic walking to prosthesis for level-ground walking, this dissertation also successfully extended this framework to experimentally realize stable prosthetic stair climbing. Similarly, the performance

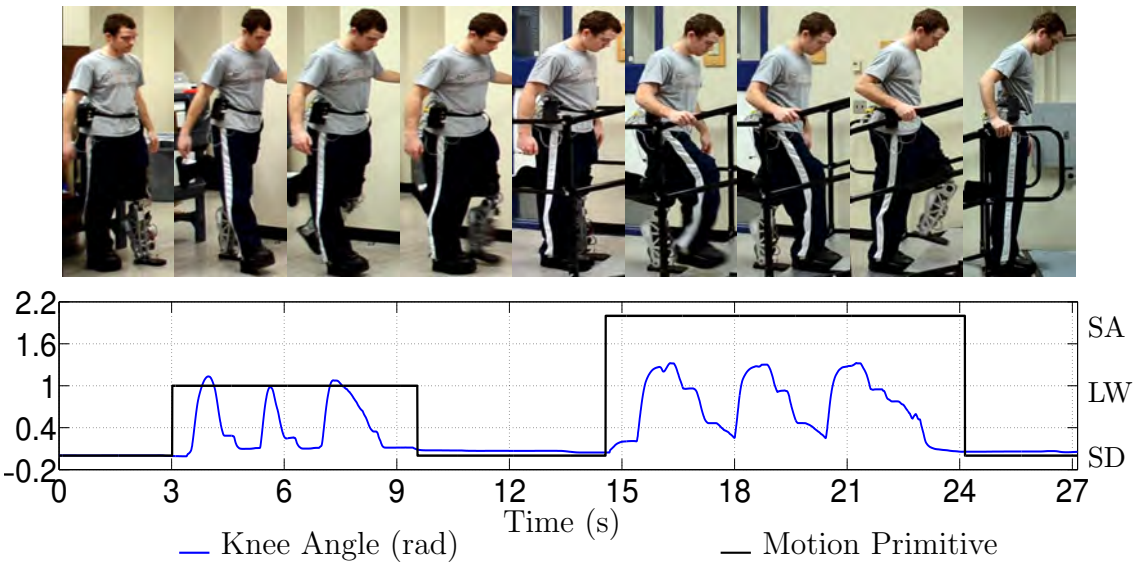

Figure 39: Gait tiles (top) of switching between three motion primitives: standing, walking and stair ascent. The bottom figure illustrates the specific primitive at specific given time (right axis) together with the real-time knee angle (left axis).

of multiple controllers—utilizing the generated robotic walking inspired by the reference IMU recorded trajectories—are compared, with the real-time optimization-based controller resulting in the best overall performance. The averaged experimental joint angles are compared with the designed gaits (utilizing the proposed optimization framework) in Figure 38. The detail discussion is omitted here and can be referred to [145].

With the optimal controller verified for both LW and SA, the pattern recognition algorithm is successfully realized using the optimal controller. To test the effectiveness of the motion intent recognition algorithm, total of 14 tests are carried. In each round of the test, the subject was asked to start from SD, take 3 steps of LW, switch to SD, then continue to SA for 3 steps, finally stopping at SD posture. During the total of 56 switches, only one failed when the subject tried to start from SD to LW. The gait tiles of one round of testing along with the real-time prosthetic knee angle are shown in Figure 39. A video of the resulting behaviors can be seen at [4].

To summarize, in this chapter, we validated the proposed systematic method on the custom transfemoral prosthesis AMPRO1 with achieving multi-contact walking and automatic motion transition. The novel optimization-based controller clearly

outperforms other traditional control such as PD w.r.t tracking performance and energy efficiency. Additionally, compared to the method of variable impedance control, this method requires much less parameter tuning, therefore can potentially benefit future use of amputees.

CHAPTER VII

TWO-STEP OPTIMIZATION FOR 3D PROSTHESES

Virtual constraints have been recognized as an essential bridging tool which has the potential to translate rich nonlinear bipedal control methodologies to the control of prostheses [47], [49], [120], [140]. The previous chapters of this dissertation have shown the successful realization of this concept for different motion types with AMPRO1. Motivated by the fact that most of the virtual constraints based methods are still limited to two basic assumptions: a) human locomotion can be approximated as planar walking and b) amputee-prosthesis system is symmetric, the work of this dissertation take further steps with proposing a hybrid-system-model based two-step direct collocation approach to automatically generate three-dimensional (3D) human-like multi-contact prosthetic gaits (i.e., virtual constraints) for asymmetry amputee-prosthesis systems.

Specific requirements—such as amputee comfortability, human-likeness, gait symmetry, physical limitations for hardware implementation—are discussed explicitly in order to quantify a well-designed prosthetic gait in Section 7.1. A 29 degrees of freedom 3D bipedal robotic model with two passive compliant feet is considered to model the asymmetric amputee-prosthesis system in Section 7.2. A passive spring is considered at the ankle roll joint of the prosthetic legs. Imposing the prosthetic gait requirements as nonlinear constraints and utilizing the asymmetric 3D hybrid system model, a two-step direct collocation optimization method is proposed to generate 3D prosthetic gaits in an optimal fashion automatically. Based on a newly designed 3D prosthetic device, the resulting prosthetic gait is analyzed in detail, showing the designed multi-contact gait is human-like, formally stable and optimal w.r.t the gait design requirements (in Section 7.3). A 3D capable prosthetic device AMPRO3 is designed and built particularly for the purpose of experimental implementation. The experiment results and discussion are presented in Section 7.4.

7.1 Performance Requirements for Prosthetic Gaits Design

The ultimate goal of an active prosthetic controller is to recover full motion capabilities of amputee subjects. The resulting prosthetic walking as discussed in [98] [124] should: a) look as closely like healthy human walking as possible (human-likeness requirement); b) interact with amputee subjects naturally without exerting undesirable forces or torques (comfortability requirement); c) be torque optimal to bear the human weight and at the same time be energy efficient (physical limitation requirement). Bearing these objectives in mind, the multi-contact behavior (heel strike and foot push off) embedded in human locomotion as discussed in Section 3.1 would be an essential term for the 3D prosthetic gait design. Additionally, more detailed performance requirements of a "well-designed" prosthetic gait are considered and discussed explicitly in this section.

7.1.1 "Human-likeness" Requirements

The first term of human-likeness requirements considered is *similarity to unimpaired walking*, which has been previously used in [26] [112]. Motivated by the fact that humans share a common joint pattern during locomoting [130], a nominal human trajectory, collected via the IMU system, can be utilized as a reference for this gait design method. We quantify this term by finding the coefficient of determination (R^2) between the resulting prosthetic knee and ankle trajectories, and the nominal unimpaired trajectories.

As another term of human-likeness performance, we evaluate the *measure of symmetry* between the prosthetic leg and the amputee's unimpaired leg [65]. To do so, the coefficient of determination (R^2) of the trajectories between the prosthetic joints (i.e., the ankle and knee joints) and the corresponding unimpaired joints is computed.

7.1.2 Comfortability Requirements

The undesired pressure of amputee-prosthesis system mostly come from the socket adapters during the stance phase and the improper landing when the prosthetic leg

strikes the ground [39]. Therefore, the first term we considered for this requirement group is the *reaction wrenches* exerted in the connection socket between the prosthetic leg and amputee subject. While there is no reference about a realistic optimal value, we believe that lower values are positively related to better user experiences with the assumption that prosthetic devices can still perform safely.

Velocity matching has been a known term in bipedal robotics aiming to reduce impact forces during foot landing. Therefore proper landing velocity could potentially reduce uncomfortable forces exerted during the foot impact. In particular, we consider the absolute *impact heel velocity* of the prosthetic leg as the second term of the comfortability requirements. It is reasonable to assume that amputees will feel better if the landing velocity is within certain range.

7.1.3 Physical Limitation Requirements

Powered-prosthetic devices are required to be light-weight and compact, therefore, yielding hardware limitations on various aspects. For example, the maximum applicable torques and velocities are limited by the size of the motor and the transmission systems. Operation duration of prosthetic devices (i.e., actively walking time) is limited by the battery pack, the size and weight of which are a big concern during the prosthetic hardware design. Therefore, energy consumption and torque requirement are always among the primary concerns when designing and controlling powered prostheses.

As the first term of physical limitation requirements, we consider the *mechanical cost of transport* (CoT) defined as

$$\Phi_{CoT} = \frac{P_{total}}{W * v}, \tag{114}$$

where P_{total} is the total mechanical power, W is the subject weight and v is the average walking speed during one complete step cycle [37].

Additionally, to guarantee that the designed gaits are feasible for implementation on hardware devices, *maximum torques*, *maximum velocities* and *joint movement ranges* are considered as the other three terms of physical requirements.

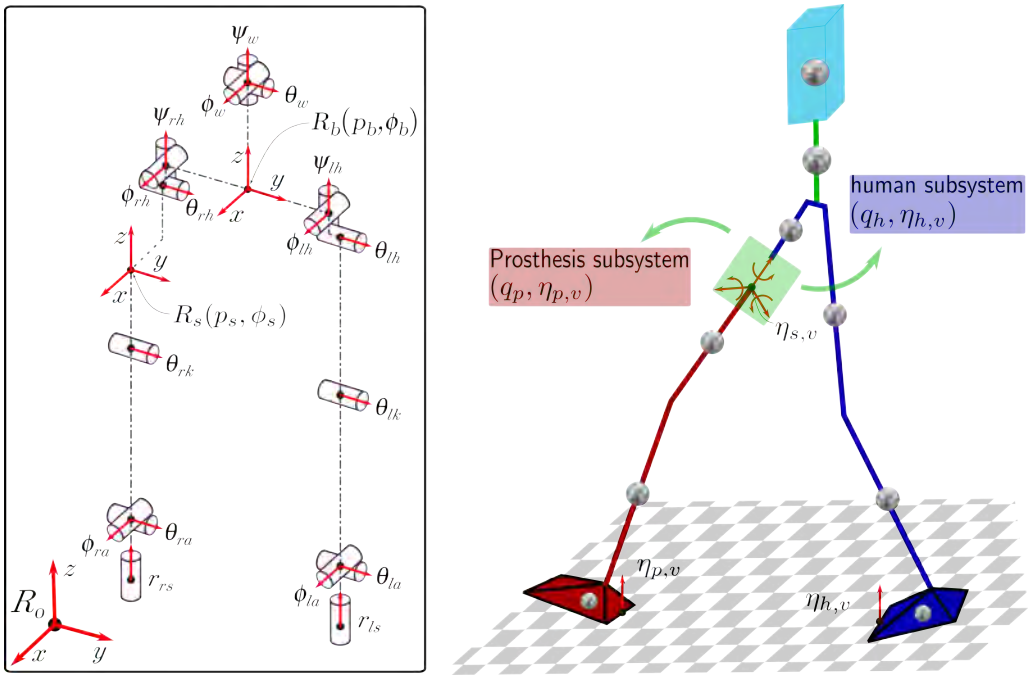

Figure 40: Joint configuration (left) and model (right) of the asymmetric amputee-prosthesis system

7.2 Asymmetry Amputee-Prosthesis System

An amputee-prosthesis system is asymmetric in natural considering it includes two different sub-systems. To be more specific, the mass, length and actuation types are different between the prosthesis sub-system and the amputee sub-system. With the goal of capturing this property during gait design process, a 3D asymmetric humanoid robot model is considered for modeling purpose.

7.2.1 Subsystems of Amputee and Prosthesis

The amputee (or human) sub-system is modeled as a kinematic chain with an inertial reference frame $R_b = \{p_b, \varphi_b\} \subset \mathbb{R}^6$ attached at the center of the hip as shown in Figure 40. As illustrated in the left plot of Figure 40, the kinematic chain of body coordinates consists of three branches: waist joints $q_w = [\psi_w, \varphi_w, \theta_w]^T$, left leg (which is assumed to be the unimpaired leg) joints $q_l = [\psi_{lh}, \varphi_{lh}, \theta_{lh}, \theta_{lk}, \theta_{la}, \varphi_{la}, r_{ls}]^T$ and the right amputated hip $q_{rh} = [\psi_{rh}, \varphi_{rh}, \theta_{rh}]^T$, respectively.

Therefore, we define the configuration space of the human sub-system as $\mathcal{Q}_h$:

$\theta_h = \{R_b, q_w, q_l, q_{rh}\} \subset \mathbb{R}^{19}$ with 13 degrees of actuation (6 actuators at the two hips, 3 at the waist, 1 at the knee and 2 at the ankle). Note that, we model the rubber shoes as stiff passive spring ($k_{stiffness} = 60000N/m, b_{damping} = 600Ns/m$) on both legs as a prismatic joint in between the calf and ankle to better capture the compliance characteristics of both the human sole and springy prosthetic foot. The spring constants are estimated based on the research in [22]. With the anthropomorphic mass, inertia and length properties of each link estimated based on Winter's method in [130] of a real subject, the equation of motion (EOM) along with the holonomic constraints for a given domain D_v is given as:

$$D_h(\theta_h)\ddot{\theta}_h + H_h(\theta_h, \dot{\theta}_h) = B_{h,v}u_{h,v} + J_{h,v}^T(\theta_h)F_{h,v}, \tag{115}$$

$$J_{h,v}(\theta_h)\ddot{\theta}_h + \dot{J}_{h,v}(\theta_h, \dot{\theta}_h)\dot{\theta}_h = 0. \tag{116}$$

Each of the terms is defined similarly as in Chapter 3.

The similar method is used to model the prosthesis sub-system. Considering the fact that the prosthetic device will be connected to the amputee at the amputated thigh by using a socket adapter, we choose to place the base frame for prosthesis leg $R_s = \{p_s, \varphi_s\} \subset \mathbb{R}^6$ at the location where the socket adapter is, which is shown in the right plot of Figure 40. The prosthetic leg is assumed to have 4 degrees of freedom $q_{rp} = [\theta_{rk}, \theta_{ra}, \varphi_{ra}, r_{rs}]^T$ but only actuated at the joints of knee pitch and ankle pitch. In particular, both the ankle roll joint and the spring foot are not actively controlled and only regulated by passive springs. With configuration space $\mathcal{Q}_p : \theta_p = \{R_s, q_{rp}\} \subset \mathbb{R}^{10}$ and mass, inertial properties obtained from the SolidWork design, the constrained dynamics can be obtained as:

$$D_p(\theta_p)\ddot{\theta}_p + H_p(\theta_p, \dot{\theta}_p) = B_{p,v}u_{p,v} + J_{p,v}^T(\theta_p)F_{p,v}, \tag{117}$$

$$J_{p,v}(\theta_p)\ddot{\theta}_p + \dot{J}_{p,v}(\theta_p, \dot{\theta}_p)\dot{\theta}_p = 0, \tag{118}$$

where $F_{p,v} : T\mathcal{Q}_p \times U_{p,v} \to \mathbb{R}^{n_{p,v}}$, with $n_{p,v}$ the number of total holonomic constraints of the prosthetic device. The rest of the terms are defined similarly as in Chapter 3.

7.2.2 Combined Humanoid Amputee-Prosthesis System

With the dynamic sub-systems of both the amputee and prosthesis in hand, we are now ready to connect these two sub-systems into a complete bipedal model via enforcing holonomic constraints at the socket. Particularly, for the combined bipedal system, the configuration space can be defined as $\mathcal{Q} : \theta = \{\theta_h, \theta_p\} \subset \mathbb{R}^{29}$; holonomic constraints are grouped as $\eta_v = \{\eta_{h,v}, \eta_{p,v}, \eta_{s,v}\}$ (corresponding to $F_v = \{F_{h,v}, F_{p,v}, F_{s,v}\}$) with $\eta_{s,v}$ ($F_{s,v}$) is the set of holonomic constraints imposed by the socket. In particular, the holonomic constraints $\eta_{s,v}$ ($F_{s,v}$) guarantee that the prosthesis sub-system is rigidly connected to the amputee sub-system, which is a reasonable assumption and also a necessary requirement during realistic daily use. Therefore, based on the new complete coordinates, the general dynamics for D_v can be given as:

$$D(\theta)\ddot{\theta} + H(\theta, \dot{\theta}) = B_v u_v + J_v^T(\theta) F_v, \tag{119}$$

$$J_v(\theta)\ddot{\theta} + \dot{J}_v(\theta, \dot{\theta})\dot{\theta} = 0. \tag{120}$$

Note that, while the rest of this work will be based on this combined model, different constraints (for example, torque limits of $u_{p,v}^{max}$ and $u_{h,v}^{max}$, connection forces $F_{s,v}$) will be considered separately for the two sub-systems.

Due to this asymmetric model construction, one human stance step (HS) and one prosthesis stance step (PS) are necessary to form a complete two-step cycle, therefore, resulting a directed graph with 8 domains as shown in Figure 41. For notation simplicity, each domain is named with a combination of the stance leg type (i.e., HS or PS) and domain trigger type (e.g., *hs* or *tl*). For example, the heel strike domain during PS phase is notated as *phs*. Therefore, the directed graph Γ can be explicitly stated as:

$$V = \{htl, hhl, hhs, hts, ptl, phl, phs, pts\}, \tag{121}$$

$$E = \{htl \to hhl, hhl \to hhs, hhs \to hts, hts \to ptl, ptl \to phl, phl \to phs, phs \to pts\}. \tag{122}$$

As illustrated in Figure 41, the foot contact holonomic constraints for each domain are straightforward (which can also be referred to the holonomic constraints definition

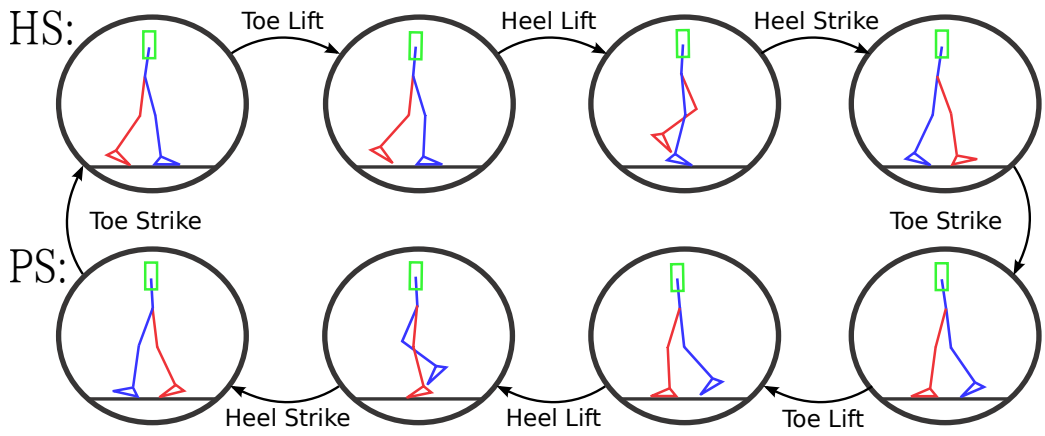

Figure 41: Two-step domain graph of the asymmetric amputee-prosthesis gait.

of AMBER2 as discussed in Chapter 4), therefore we omitted this part here for simplicity. Similar discussion can also be found in [51].

With notation $x = (\theta; \dot{\theta})$, the affine control system for each domain D_v can be obtained as $\dot{x} = f_v(x) + g_v(x)u_v$ by reformulating (119) and (120) [128]. The discrete behavior, Δ_e, of impacts is modeled with the assumption of perfectly plastic impacts as discussed in Chapter 3.

7.3 3D Prosthetic Gait Optimization

In this section, we emphasis the computationally effective nonlinear optimization that generates periodic two-step asymmetric amputee-prosthesis gaits subject to the particular requirements discussed in Section 7.1. More specifically, the goal is to determine a set of virtual constraints parameters $\{\alpha_v\}_{v \in V}$ so that the resulting gait satisfies the PHZD condition and various gait design constraints.

7.3.1 Two-Step Direct Collocation Optimization

As discussed in Section 7.2, a periodic two-step gait cycle of the amputee-prosthesis walking consists of 8 continuous domains in the order shown in Figure 41. Using traditional single shooting optimization as in Chapter 4 for AMBER2 would be extremely difficult to numerically generate optimal gaits for such a complicate system. Therefore, a direct collocation based multi-domain HZD gait design approach introduced in [51] is applied with particular modifications for the two-step hybrid system. Note that,

the general multi-domain optimization framework discussed in Chapter 3 still applies here. In the following discussion, we apply the direct collocation method, which is a computationally efficient tool, to solve this 8-domain optimization problem.

Here, we simply introduce the main idea of the direct collocation optimization. In the *direct collocation* formulation, system states, x, over a continuous domain is discretized first and then the solution of the dynamical system between discrete nodes is approximated (collocation) by specific polynomials. By driving the defects, or differences, between the slope of approximated solution and the exact closed-form first order dynamics, $\dot{x}$, to zero we implicitly enforce the approximated solution to the dynamics of the system. As a result, the time-marching forward integration of the dynamics is replaced by algebraic equality constraints at collocation points. In particular, the solution of each domain, D_v, is discretized based on the time discretization

$$0 = t_0 < t_1 < t_2 < \cdots < t_{N_v} = T_{I,v_i}, \tag{123}$$

assuming $T_{I,v^i} > 0$ is the time at which the system reaches the guard associated with a given domain. Let x^i and $\dot{x}^i$ be the approximated states and first order derivatives at node i, the defect constraints are defined at each odd node as:

$$\dot{x}^i - 3(x^{i+1} - x^{i-1})/2\Delta t_v^i + (\dot{x}^{i-1} + \dot{x}^{i+1})/4 = 0, \tag{124}$$

$$x^i - (x^{i+1} + x^{i-1})/2 - \Delta t_v^i(\dot{x}^{i-1} - \dot{x}^{i+1})/8 = 0, \tag{125}$$

where $\Delta t_v^i = t_{i+1} - t_{i-1}$ is the time interval. Moreover, the first order derivatives must satisfy the system dynamics, i.e., $\dot{x}^i = f_v(x^i) + g_v(x^i)u_v^i$. In particular, the control inputs u_v^i at each node is enforced to be the feedback linearization controllers discussed in Section 7.2. Further, the domain admissible constraints and guard condition are also imposed accordingly. The system states between two continuous domains are connected by enforcing the discrete dynamics, Δ_e, of each associated edge.

Followed from the general construction of the multi-domain HZD gait optimization in [51], we state the two-step amputee-prosthesis gait optimization to minimize the

mechanical CoT of the gait, given as:

$$\underset{\mathbf{z}^*}{\text{argmin}} \ \Phi_{CoT}(\mathbf{z}) \tag{126}$$

$$\text{s.t} \quad \mathbf{z}_{\min} \leq \mathbf{z} \leq \mathbf{z}_{\max}, \tag{127}$$

$$\mathbf{c}_{\min} \leq \mathbf{c}(\mathbf{z}) \leq \mathbf{c}_{\max}, \tag{128}$$

where $\mathbf{z}$ is the set of all decision variables, and $\mathbf{c}(\mathbf{z})$ is a collection of necessary constraints presented in [51]. In the case of two-step gait optimization, the parameters consistency constraints are enforced between domains of one step. The step lengths and widths of two steps, which are normally different from each other, are incorporated into the desired positions of the feet as holonomic constraints respectively. Due to the page limit, the detailed construction of the optimization is omitted here. For more details, we refer the readers to [51].

As discussed in Chapter 3, the main purpose of the optimization problem is to design a proper set of virtual constraints, which are characterized by the parameter set α. Another major modification of the direct collocation optimization method—compared to the single shooting method of AMBER2—is that the desired position-modulating outputs are given in term of a Bézier polynomial of degree M (instead of ECWF), determined by $M+1$ coefficients [128]:

$$y_2^d(\tau, \alpha_o) := \sum_{k=0}^{M} \alpha_o[k] \frac{M!}{k!(M-k)!} \tau^k (1-\tau)^{M-k}, \tag{129}$$

for all $o \in \mathcal{O}_v$ with $\mathcal{O}_v$ be an indexing set of outputs, and α_o is a vector of Bézier polynomial coefficients. The particular reason of choosing Bézier polynomial function over the ECWF is that the Bézier polynomial function has simple derivation terms, which allows for more efficient computation. Note that, the explicit discussion of outputs set for each domain is omitted here as the major focus of this work are the ankle and knee joints. $\tau(\theta)$ is the phase variable as defined (22).

7.3.2 Prosthetic Gait Design Constraints

Based on the general multi-domain HZD gait optimization in (HIO), we primarily focus on specific performance requirements of the amputee-prosthesis gaits discussed

in Section 7.1.

Human-likeness Constraints. With the goal of designing human-like prosthetic gaits, a strong focus is put on the ankle and knee joints via constraining the differences between the optimized trajectories and the reference unimpaired walking trajectories to be bounded. Let $\theta_p^i = (\theta_{ra}^i, \theta_{rk}^i)$ be the prosthesis joint angles and $\theta_h^i = (\theta_{la}^i, \theta_{lk}^i)$ be amputee joint angles at node i, then for two positive constants $\delta_p > 0$ and $\delta_h > 0$, we impose the *human-likeness* constraints as:

$$\|\theta_r(\tau(\theta^i)) - \theta_p^i\| \leq \delta_p, \qquad \text{(Gait Similarity)}$$

$$\|\theta_r(\tau(\theta^i)) - \theta_h^i\| \leq \delta_h, \qquad \text{(Gait Symmetry)}$$

where θ_r is the reference ankle and knee trajectories that scaled on the interval of $[0, 1]$ and then interpolated by the phase variable, τ. Note that, due to the concern of computation efficiency, we do not directly constrain the coefficient of determination in the optimization. Instead, these two constraints guarantee that the designed gaits are within a small boundary of the desired values. The coefficient of determination will be examined in simulation. As (Gait Similarity) constrains the prosthetic trajectory to be human-like, (Gait Symmetry) guarantees the amputee trajectory is also close to the reference trajectory, therefore resulting in gait symmetry.

Comfortability Constraints. As discussed in Section 7.1, two comfortability constraints—reaction wrenches at the socket adapter and impact velocities at the landing foot—are considered in our two-step gait optimization. As discussed in Chapter 4, the heel strike is the major impact during human locomotion, therefore, we only consider the impact velocities during the heel landing.

To impose these requirements, we consider admissible boundary sets $\{F_{s,v}^{\min}, F_{s,v}^{\max}\}$ with $v \in V$ and $\{v_{hhs}^{min}, v_{hhs}^{max}\}$ for each of them. Note that, the boundaries of reaction wrenches will be different depending on the specific domain $v \in V$, therefore, the connection wrench constraints are enforced in a general form as:

$$F_{s,v}^{\min} \leq F_{s,v}^i \leq F_{s,v}^{\max}. \qquad \text{(Connection Wrench)}$$

In addition, the heel impact velocity constraints in all x, y, and z directions are imposed at the end of the human-stance heel strike domain (hhs) with $i = N$, which

is given as:

$$v_{hhs}^{\min} \leq \dot{p}_{rh}(\theta^N, \dot{\theta}^N) \leq v_{hhs}^{\max}. \qquad \text{(Impact Velocity)}$$

where $p_{rh}(\theta)$ is the three dimensional Cartesian position the prosthesis heel (i.e., right heel in our construction).

Physical Limitation Constraints. Considering that the cost function (or objective function) of the gait optimization is defined as the mechanical cost of transport, it is only required to apply constraints for the admissible joint torques, $u_j^{\max}$, admissible velocities, $\dot{\theta}_j^{\max}$ and admissible positions, $\{\theta_j^{\min}, \theta_j^{\max}\}$ which are introduced by the prosthetic hardware limitations. Hence, at each node i for all domains, we have:

$$-u_j^{\max} \leq u_j^i \leq u_j^{\max}, \qquad \text{(Admissible Torque)}$$

$$-\dot{\theta}_j^{\max} \leq \dot{\theta}_j^i \leq \dot{\theta}_j^{\max}. \qquad \text{(Admissible Velocity)}$$

$$-\theta_j^{\min} \leq \theta_j^i \leq \theta_j^{\max}. \qquad \text{(Admissible Position)}$$

In addition to the major constraints discussed above, other auxiliary constraints (for example, foot clearance, step length and step width) are also considered in this optimization. Due to the discretization of states and the particular defect variables formulation, all of these constraints can be directly applied on the boundary values of corresponding decision variables or the functions of the decision variables. Incorporating the above constraints in (126), the end result is a large-scale nonlinear programming (NLP) problem with over $40,000$ optimization variables and $40,000$ constraints.

Remarks. Combined with the asymmetric hybrid system model in Section 7.2, the main power of the proposed two-step direct collocation method is that it embeds the model asymmetry directly into the gait design and can impose explicit constraints separately on every node of each domain. Benefiting from the highly computationally effective direction collocation method, this optimization problem can be solved in 20 mins using IPOPT with linear solver $ma57$ on a laptop computer with an Intel Core i7 $-$ 2700QM processor (2.2 GHz) and 24 GB of RAM. More importantly, the

general formulation of this problem allows this method to be implemented onto other asymmetric robot platforms, which are common in many real-world systems.

7.4 Experiment Realization of AMPRO3

To experimentally validate the gait generation method discussed above, a new powered transfemoral prosthesis AMPRO3 is designed and built. The mechanical design of AMPRO3 is discussed first. A hybrid system model is constructed, the model parameters of which are based on the AMPRO3 and the testing subject. The simulation results are presented first and the preliminary experimental results are discussed at the end.

7.4.1 Design of AMPRO3

The design of AMPRO3 provides the convenience of on-board power alongside the advantages of highly dynamic motion and sensing capabilities, all in a compact design. This device has two 206 W brushless DC motors (MOOG BN23) for actuating knee and ankle flexion/extension joints, which both contain a torsion spring [61] between the harmonic gearbox and joint to form a series elastic actuator (SEA). Importantly, compared to AMPRO1 for which the motor is connected directly to the harmonic gear box, the design of AMPRO3 separates the motor and the gear box, and adds a pulley-belt driven transmission system in between. This design has two important advantages. First, more gear reduction ratio can be obtained by using different size pulleys, which allows us to choose smaller and lighter harmonic gear box. Additionally, the belt-driven system brings compliance to the system, which can isolate the motors from direct impact shocks. Both joints have an incremental encoder monitoring the motor side of the compliance, and an absolute encoder measuring the joint output. Two ELMO motion controllers (Gold Solo Whistle) are used for motor driving and low-level torque control purposes. A 9-cell Lipo battery (ThunderPower) is used to power the whole system. The total weight of AMPRO3 without considering the knee adapter is 5.4 Kg and the total height is 442 mm.

Motivated by the fact that the lateral ankle movement plays an important roll

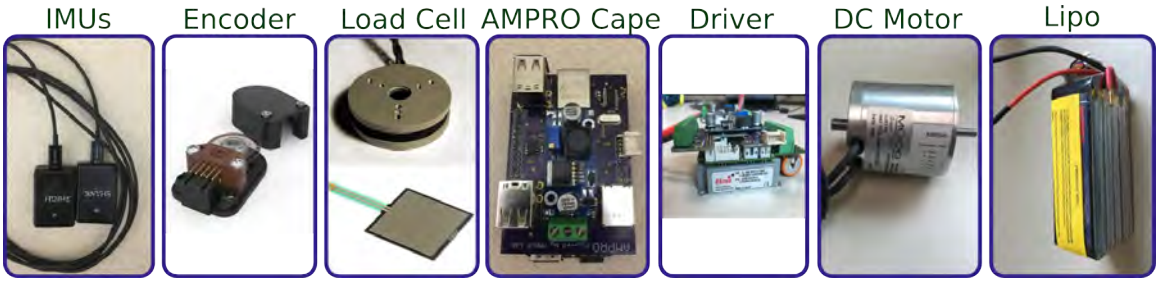

Figure 42: Electric components of 3D prosthesis AMPRO3

for amputees' comfortability during standing and walking (for example, walking on uneven terrains), the device also incorporates a stiff, yet passive ankle roll joint, allowing the user to perform a more natural 3D gait style. The spring components design of AMPRO3 incorporates with the Control-in-the-Loop method for spring constants selection. In particular, different spring constants were tested in simulation and the final parameters were chosen with regard to performance parameters such as the joint torques and CoT. A 6-axis load cell is mounted in serial in between the calf and the foot to provide the ground reaction information during locomotion. Two flex force sensors can also be mounted at the heel and toe of the foot to provide on-and-off condition for more complex foot motion (e.g., multi-contact with heel strike and toe off).

To expand the functionality of the BeagleBone Black (BBB) micro-controller board, a custom printed circuit board (PCB): AMPRO Cape is designed with adding a CAN bus chip (for communicating with ELMO drives), 4 USB ports (for communicating with load cell and IMUs) and a 5 V voltage regulator (for power supply of the BBB and USB ports). The shape and layout of the board are designed in particular with considering the hardware design of AMPRO3 with the goal of maximizing mechanical space usage, therefore, minimizing the weight and height. For the purpose of better wire organization, we also designed a custom PCB for the ELMO motion driver. This ELMO board contains a) a voltage converter to power the logic board of the ELMO; b) CAN bus connectors and power connectors to allow multiple ELMOs to be connected in serial. The result is a much more organized wiring system for AMPRO3. The major electric components are shown in Figure 42 and the complete

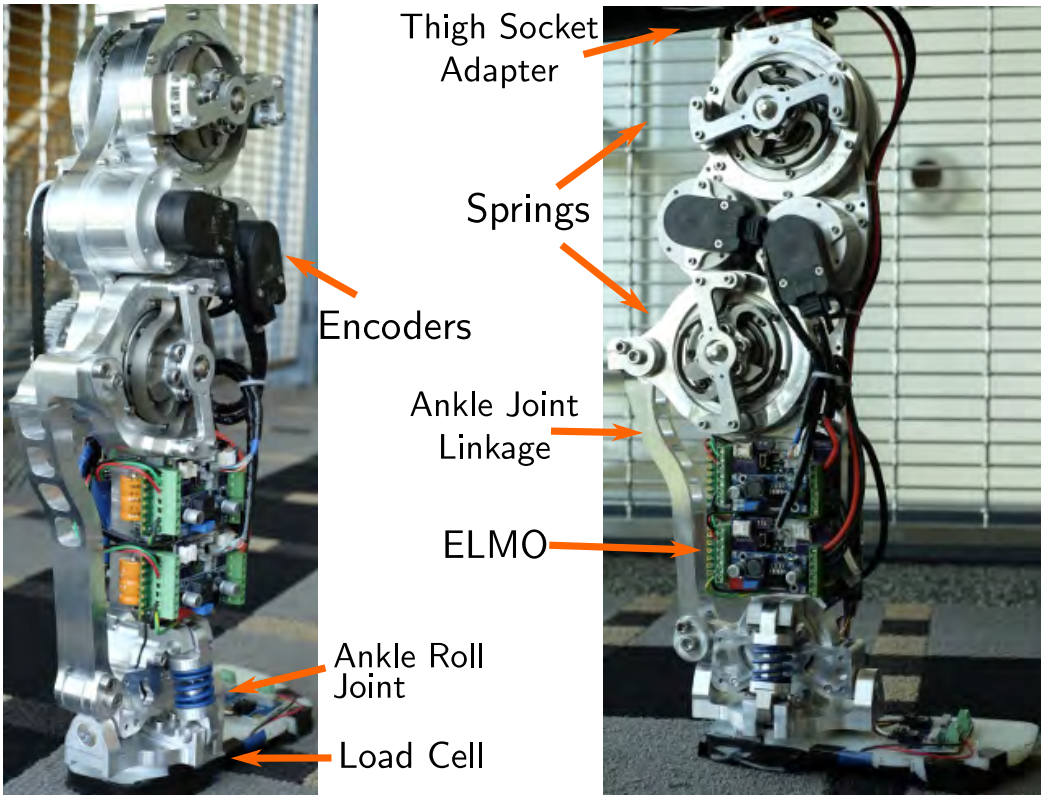

Figure 43: Diagram of 3D prosthesis AMPRO3

hardware diagram of AMPRO3 is shown in Figure 43. The control architecture of AMPRO3 is similar as AMPRO1, which has three levels. The detailed discussion is omitted here and can be referred to the discussion of AMPRO1.

7.4.2 Simulation Results

For the purpose of modeling and simulation, the prosthetic leg parameters are obtained from the AMPRO3 SolidWorks model and the amputee parameters are calculated from the testing subject's body segment properties. In particular, the shank and foot masses of the amputee are computed to be 3.36 Kg and 1.32 Kg compared to 4.42 Kg and 1.02 Kg of the prosthetic device, respectively. Note that, the inertias for two legs are also different in the model and the total mass of the amputee-prosthesis system is 75.4 Kg.

For the connection force constraints, even though we impose constraints on all three terms of the socket reaction wrenches, the discussion would mainly focus on

the z direction force and y direction torque, which are the two biggest and most critical terms among all the forces and torques. In particular, based on research that shows the nominal ground reaction force is around 10 times (which is close to the gravity constant g) of human mass, we constrain the z direction force to be smaller than 700 N and the y direction torque to be smaller than 100 Nm, which is based on the maximum admissible joint torque. For other comfortability constraints, we also put particular focus on the z direction impact velocity, which is constrained to be less than 2 m/s. Note that, this number is estimated based on the forward walking speed, which we designed to be less than 2 m/s. The admissible torques for both the prosthetic ankle joint and knee joint are set to be 120 Nm, which are calculated based on the transmission design of AMPRO3. The joint velocities (6 rad/s for the knee joint and 4 rad/s for the ankle joint) and position limits ($0° \sim 74°$ and $-40° \sim 40°$ degree for the knee and ankle joint, respectively) are also considered explicitly for both amputee-subsystem and prosthesis sub-system in the optimization problem.

The resulting prosthetic trajectories after solving the two-step direct collocation optimization problem are shown in Figure 44 with comparisons to both the simulated human side trajectories and the nominal human data from Winter [130]. From this figure, we can see that both the knee and angle joints share a similar pattern as the nominal human locomotion. The determinations (R^2) for both gait similarity to unimpaired walking and gait symmetry between the two legs are presented in Table 5, which also includes the step size and step velocity for the amputee stance phase and prosthesis stance phase. As shown in Table 5, the walking velocity during prosthesis stance phase is slightly slower with a shorter step size, which is reasonable considering that stricter constraints are imposed on the prosthetic leg during prosthesis stance.

Table 5: Performance of Designed Gait.

	Gait (R^2_{ankle}, R^2_{knee})		Step		
Stance Leg	Symmetry	Similarity	Clearance	Length	Velocity
Human	(0.96, 0.99)	(0.32, 0.94)	$0.02m$	$0.477m$	$0.515m/s$
Prosthesis	(0.96, 0.99)	(0.41, 0.97)	$0.03m$	$0.476m$	$0.483m/s$

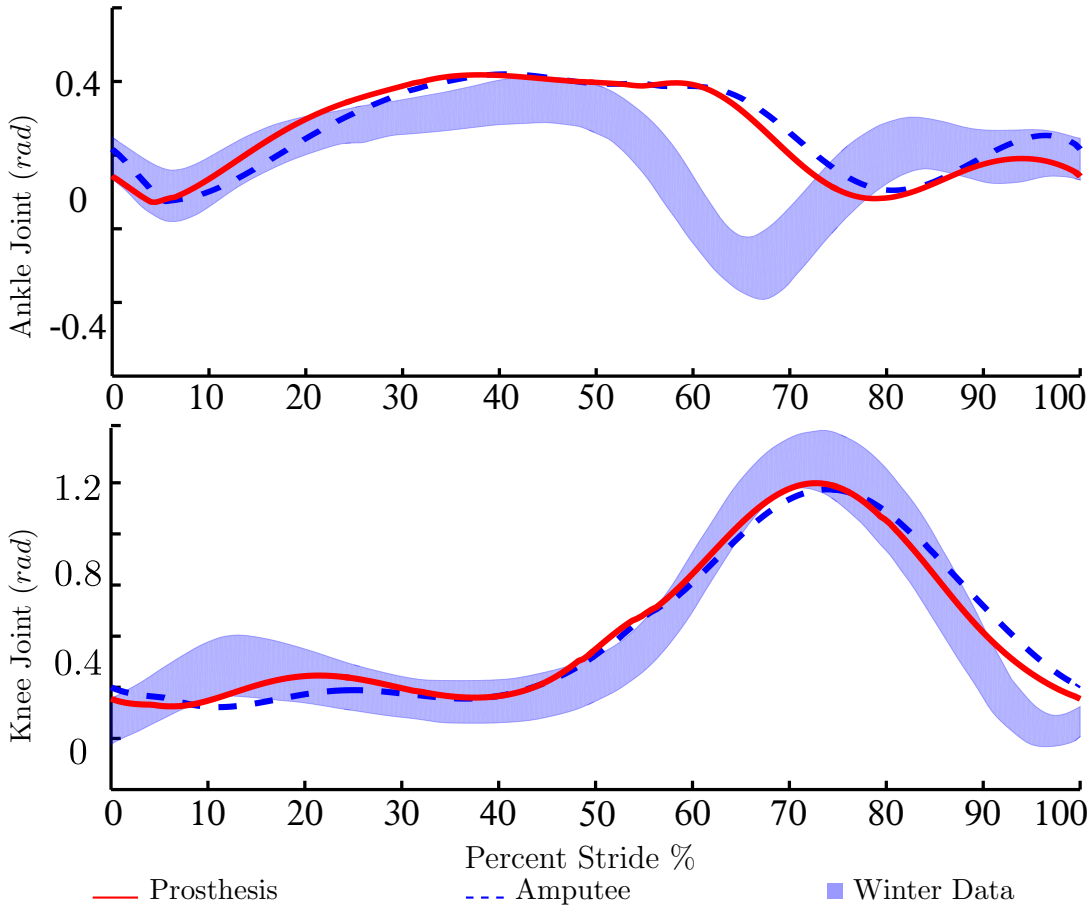

Figure 44: Trajectory comparisons between the simulated amputee-prosthesis joints and the nominal human locomotion trajectory from Winter data [130].

We also imposed a higher foot clearance constraint for the prosthetic leg to give a bigger safety margin to avoid stumble. As a result, this constraint yields a higher maximum flexion for the prosthetic leg during the swing phase as shown in Figure 44. The resulting gait satisfies the maximum connector wrench constraints. In particular, we were able to reduce the maximum z direction force from 1200 N (without constraints) to under 700 N. The y direction torque in the connection adapter also satisfies the bound. The CoT of the designed gait in simulation is 0.25, which is close to the nominal human locomotion with CoT of 0.2 as reported in [37].

As the PHZD constraints guarantee stability formally, the phase portraits of both the knee and ankle joints for 20 steps are plotted in Figure 45. In this figure, we can clearly see two-phase limit cycles for each joint since the system is asymmetric. Numerical evaluation shows the maximum eigenvalue is $2e^{-4}$, indicating stability of

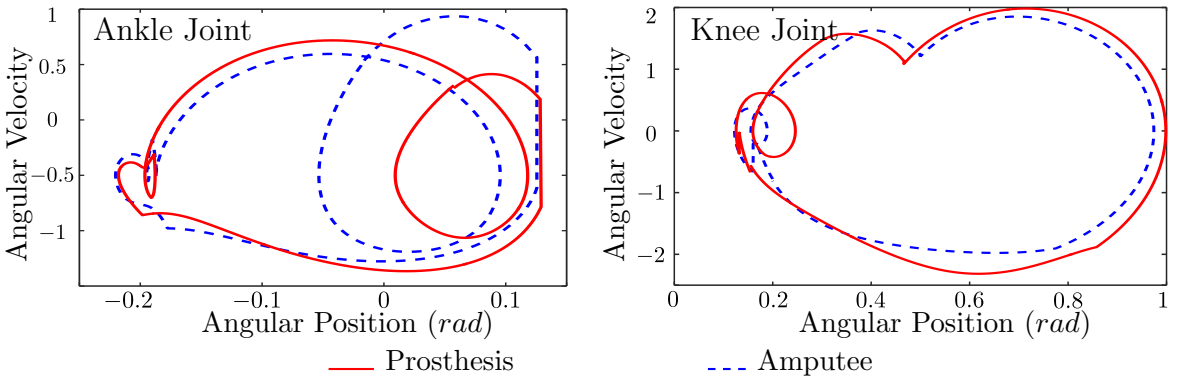

Figure 45: Phase portraits of the ankle and knee joints of both the amputee and prosthesis over 20 steps.

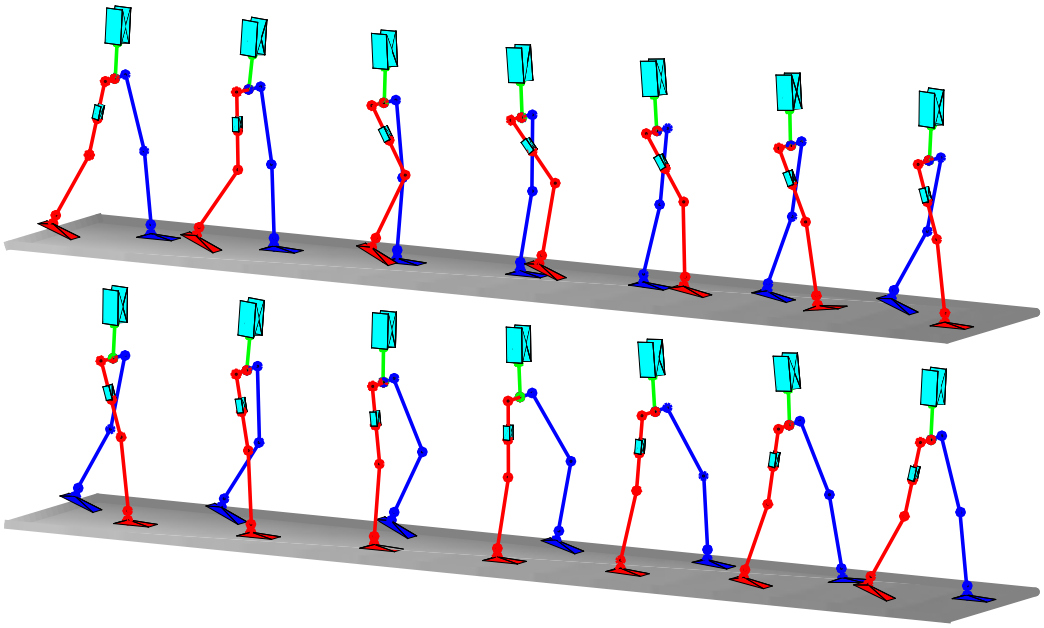

Figure 46: 3D view of the simulated gaits tiles.

this gait [127]. Gait tiles of two steps are shown in Figure 46, implying well human-likeness of the designed multi-contact gait. A simulation video can be seen in [5] for better illustration of the prosthetic walking from different view angles.

7.4.3 Experiment Setup

An unimpaired subject (who is the author of this dissertation) is considered for the preliminary experimental testing of AMPRO3. A commercial available hand-free knee scooter (iWalk 2.0) is modified and used as the knee adapter for the unimpaired subject. A shoe balancer (Evenup) that features a small extension (3.45 cm) of the

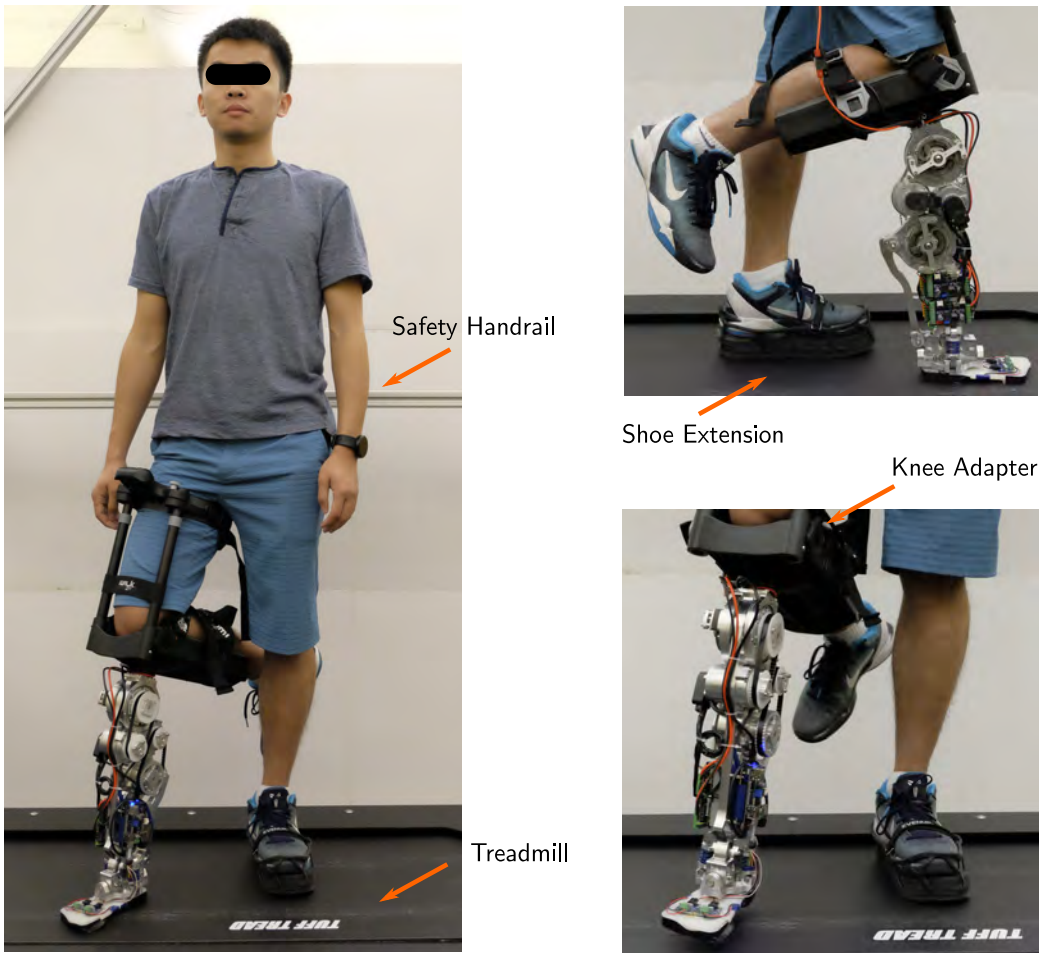

Figure 47: Experiment setup of AMPRO3

shoe was utilized in order to have the subject's residual limb of equal length to the combination of AMPRO3 and the subject's suction socket connection. The subject was instructed to walk on a treadmill with a constant speed. There are handrails on both sides for safety purposes. The detailed experiment setup of the testing is shown in Figure 47.

Trajectory Playback. Different from the 2D case of AMPRO1, the output combination of AMRPO3 includes nonlinear outputs. Additionally, there are more than 3 degrees of underactuation in the system. Therefore, it is not practical to use the PHZD reconstruction strategy as we did for AMPRO1. Instead, both the knee and angle joint trajectories, along with the corresponding phase variable τ, are recorded during simulation. In the experiment, the actual τ, which is computed either based

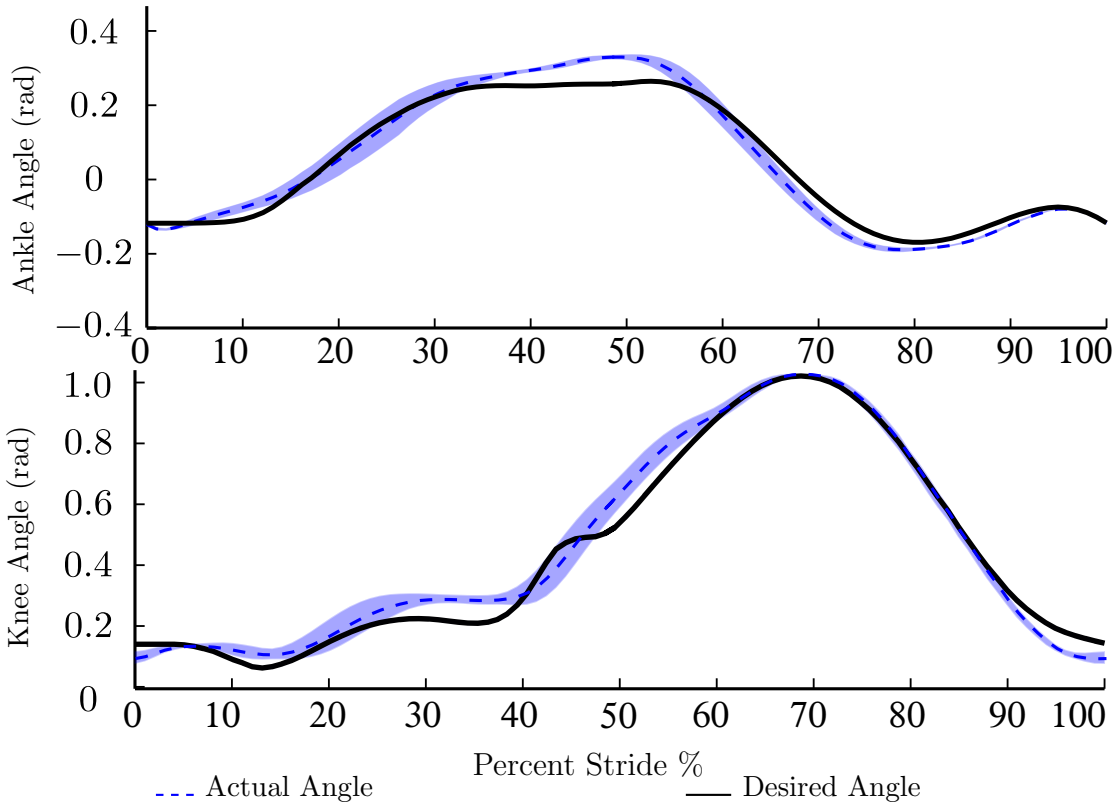

Figure 48: Averaged experimental joint angles of 3D multi-contact prosthetic walking compared with desired trajectory. Grey area is the one standard deviation of the experiment results.

on the states (during PS phase) or time (during HS phase), will be compared with the recorded values. Linear interpolation method is utilized to compute the desire trajectories for a specific τ. This method has been implemented successfully on several humanoid robots, for example 2D PROXI in [52] and 3D DURUS in [51].

7.4.4 Experimental Results

Walking trials were performed on a treadmill with a constant speed of 1.4 mph. A PD controller μ^{pd} is implemented first to achieve stable walking for the purpose of impedance parameter estimation. With the impedance parameters in hand, we apply impedance control μ^{imp} as the feed-forward term while using the MIQP control μ^{qp} as the feedback term to track the desired joint trajectories. The resulting joint trajectories (averaged over 20 steps) are compared with the designed gait in Figure 48,

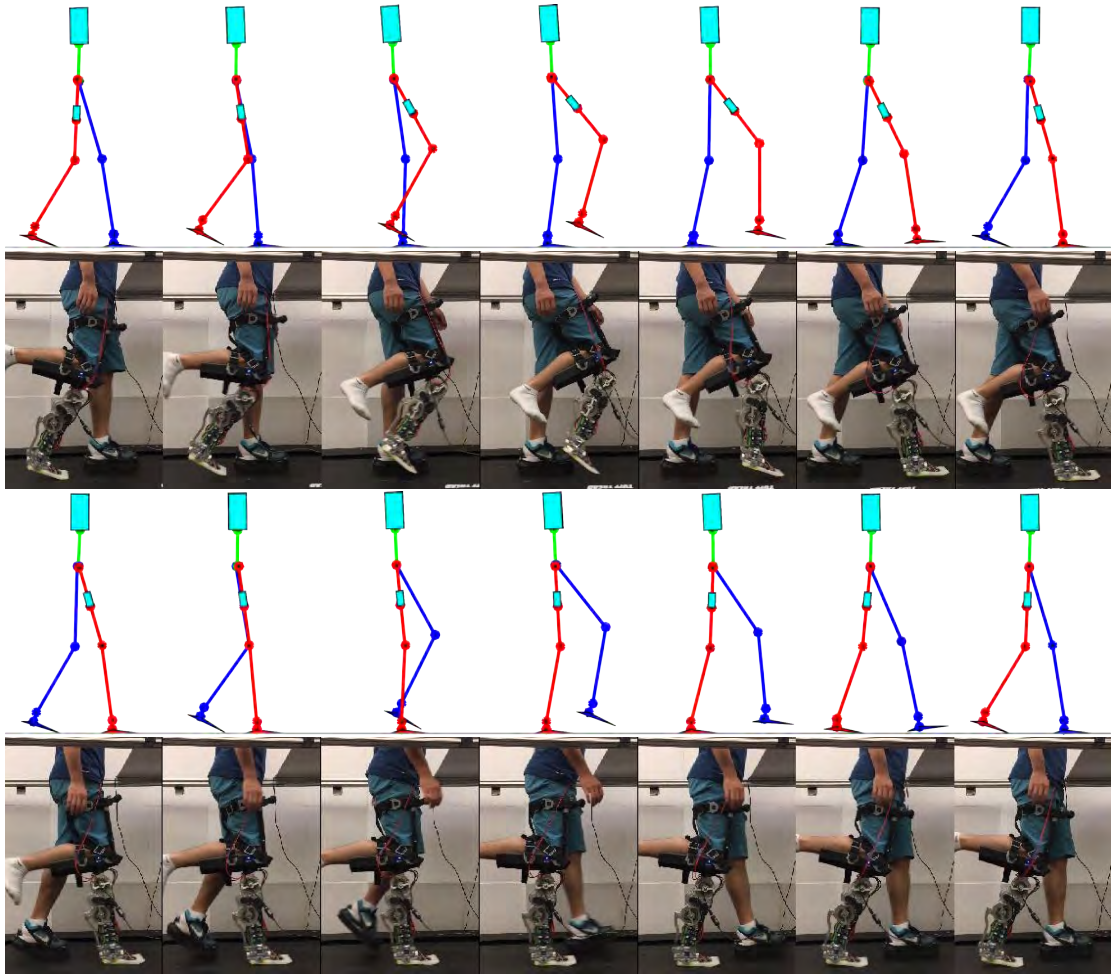

Figure 49: AMPRO3 Gait tile comparison between the experimental walking and the simulated walking.

showing that the obtained prosthetic walking is able to realize the designed gait successfully and shares a similar pattern as the healthy human locomotion, which can be referred to Figure 44. Note that, for the preliminary testing, we neglect the effects of the torsional springs during the control and tracking. Only one incremental encoder is considered for each joint. Therefore, because of the compliance effect of the torsional springs, the tracking results are not as good as the cases of AMPRO1, which use rigid chain drive. Smart SEA control will be a future topic as an extension research of this dissertation.

The experiment gait tiles of the multi-contact level-ground walking using the proposed optimization-based controller along with the simulated prosthetic walking

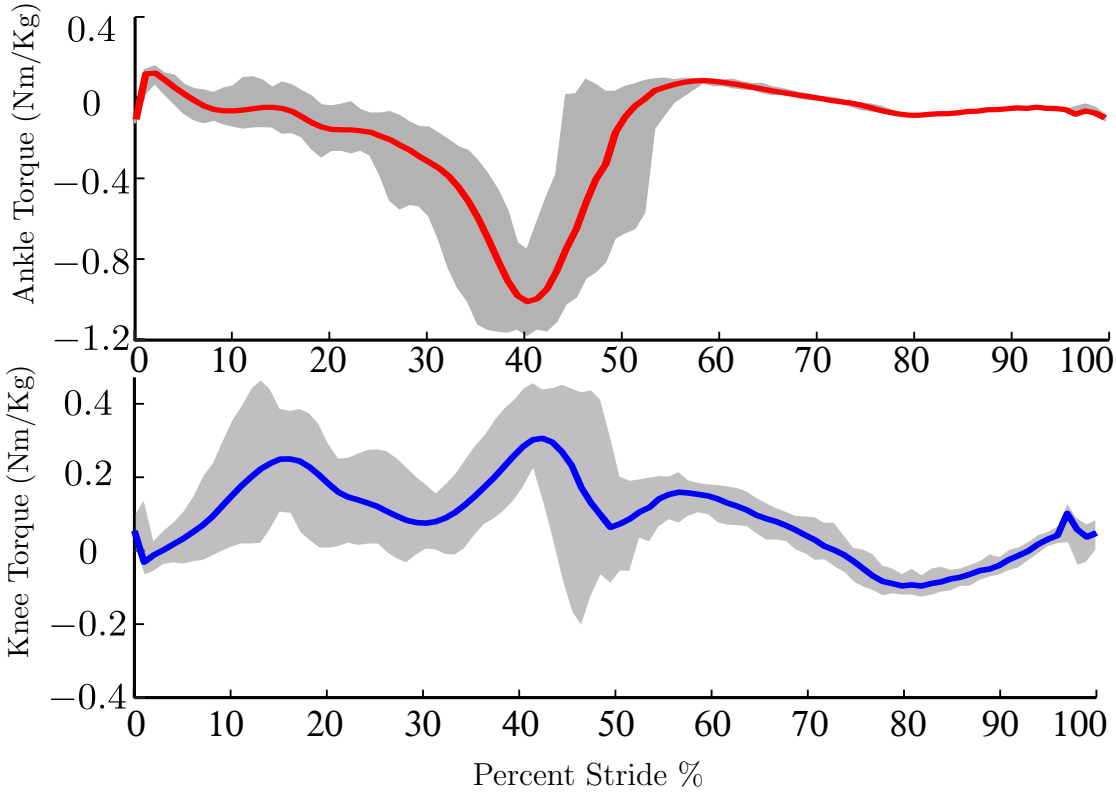

Figure 50: Normalized experimental joint torques of 3D multi-contact prosthetic walking. Grey area is the boundary of the experiment results over 20 steps.

are shown in Figure 49. Figure 50 shows the averaged torques (over 20 steps) of both joints. A video of the resulting multi-contact walking can be seen at [7]. We also took the AMPRO3 in a travel to DC. The AMPRO3 was successfully demonstrated in both outdoor and indoor environments in DC. A video is attached to show the walking demonstration [6].

7.4.5 Discussion

The main goal of this chapter is to extend the systematic methodology from 2D case of AMPRO1 to the 3D case of AMPRO3. With a 3D asymmetric hybrid system model, more realistic amputee-prosthesis model can be constructed. Based on this model, a two-step direct collocation optimization method is developed, which allows one to impose various constraints for designing a better prosthetic gaits in 3D. CoT is used as the objective function with the goal of achieving more energy efficient gait.

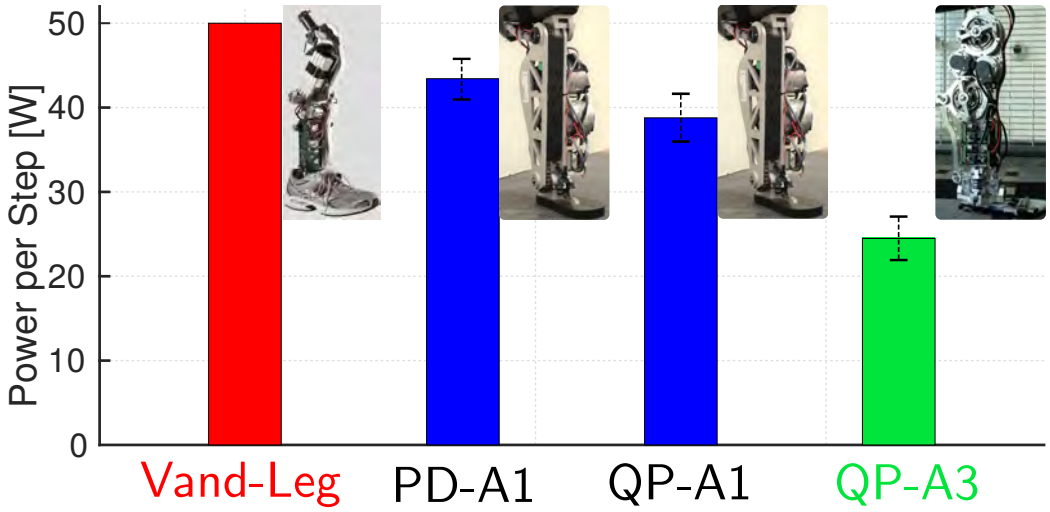

Figure 51: Comparison of natural multi-contact prosthetic walking among Vanderbilt Leg (Vand-Leg), AMPRO1 (A1) and AMPRO3 (A3). PD-A1 is the averaged power (over 20 steps) of one step (two strides) of using PD+Impedance controller with AMPRO1; QP-A1 is MIQP+Impedance controller with AMPRO1 and QP-A3 is MIQP+Impedance controller with AMPRO3.

To experimentally validate the obtained 3D prosthetic gait, a new powered prosthesis AMPRO3 is designed and built with several advancement comparing to AMPRO1. In particular, two SEA joints are added for AMPRO3, which opens the potential for compliant joints control with energy saving. However, the control of SEA remains to be a hard research topic in the literature, which can be an extension research of this dissertation. The focus of this chapter is to introduce the system design and experiment setup of AMPRO3. The preliminary results of testing AMPRO3 for the cases of both flat-foot and multi-contact walking fulfill this objective.

From Figure 44, we can see that the tracking performance is not as good as the case of AMPRO1. This is because of the existence of the passive spring between the joint and the motor. The torque profile of the ankle joint in Figure 50 clearly indicates a foot push at the end of the stance phase, which is an essential character for multi-contact walking. Therefore, we can conclude that AMPRO3 has achieved realistic human-like walking, which can be further validated by the gait tile plots in Figure 49. To further show the power performance of AMPRO3, we compare the average power consumption of one step (over 20 steps) with both AMPRO1 and the Vanderbilt

Leg [112] in Figure 51. Clearly, we can see that the proposed optimization-based controller outperforms both the traditional controller and the Vanderbilt Leg. More importantly, AMPRO3 consumes much less energy than AMPRO1. The possible reasons are threefold: a) AMPRO3 is lighter and smaller than AMPRO1; b) The tracking of AMPRO3 is not as good as AMPRO1; therefore, less energy is required; c) the passive springs in the system can help restore and release energy, which can also be seen from the lower torque of AMPRO3 comparing to AMPRO1.

To summarize, the main contribution of this chapter are threefold: a) propose a new optimization method for solving more complicate 3D prosthetic gaits; b) develop the full system integration of a 3D transfemoral prosthesis: AMPRO3; c) realize the preliminary experimental testing of a 3D multi-contact prosthetic gait on AMPRO3 with achieving stable prosthetic walking.

CHAPTER VIII

CONCLUSION AND FUTURE WORK

This dissertation presented a systematic methodology—including gait generation and optimization-based nonlinear control—for achieving stable human-like prosthetic walking. Compared to traditional prosthetic control such as variable impedance control, the motivation was to achieve prosthetic walking that is energy efficient and requires less parameter-tuning. The approach of this dissertation began with looking into bipedal robotic locomotion research. In particular, inspired by the essential multi-contact behavior encoded in human walking, this feature was analyzed and used to motivate the construction of a hybrid system model representing a multi-contact robotic walking gait. Based on this hybrid system model, an optimization framework was developed to formally generate stable robotic walking gaits for bipedal robots. Because of specific constraints considered during solving the optimization problem, the generated gaits can be directly implemented on hardware, which was validated on the physical robot AMBER2.

Motivated by the common locomotion style (in the sense of hybrid and bipedal) of both bipedal robots and prostheses, this work took the first steps by modeling the amputee-prosthesis system as a hybrid system model similarly as bipedal robots. Therefore, the framework of both gait generation and control design can be translated from bipedal robotic locomotion to prosthetic walking. Considering the fact that prosthetic devices can only access to local feedback information, a novel model independent optimization-based controller was proposed with the goal of achieving tuning free and torque optimal prosthetic control. This controller was first verified on the robotic platform AMBER1 in both simulation and experiment. Two powered transfemoral prostheses were designed from the ground up to test this systematic method with real human subjects. The experimental results demonstrated that this methodology can be successfully applied to prosthetic walking while reaching the

stated design goal.

The main contribution of this dissertation is that we took the first steps to bridge the gap between bipedal robots and prostheses from a control experts' perspective. The advantages of this framework are twofold. The first advantage is that human-like prosthetic gaits can be designed by using an optimization problem. While the gait design parameters still need tuning in order to generate a proper gait, the benefaction is that this tuning process can be done in simulation in a high level fashion. To be more explicit, the tuning process can be shifted to the robots side more, which will potentially reduce testing effort on human subjects. Note that, the work in this dissertation didn't claim that a more human-like gait with a better tracking controller is superior than the traditional finite state based linear control method. A commonly accepted benchmark or criterion for quantizing a better prosthetic controller or walking is important for future research. Importantly, because of the general formalization of the proposed optimization problem, these criteria can be viewed as constraints, which can be used to improve the gait design procedure. Secondly, different controllers can be designed and tested on the formal hybrid system model before being implemented on actual devices. These controllers can also be verified on bipedal robots considering the similar formal mathematical construction shared between bipedal robots and prostheses. Therefore, this framework opened possibilities to various nonlinear prosthetic control methods such as adaptive control or robust control.

8.1 Summary of Contribution

In conclusion, the contribution of this dissertation can be summarized with five components, which is also shown visually in Figure 52. More explicit summarization is discussed as the following.

Multi-Domain Optimization Framework. Firstly, a formal human-inspired multi-domain optimization framework for generating stable multi-domain robotic walking gaits was developed. A theory was formulated and proved to formally guarantee stability of the generated multi-domain (or multi-contact) gaits. Addition to the stability constraints, physical constraints along with full model dynamics are considered

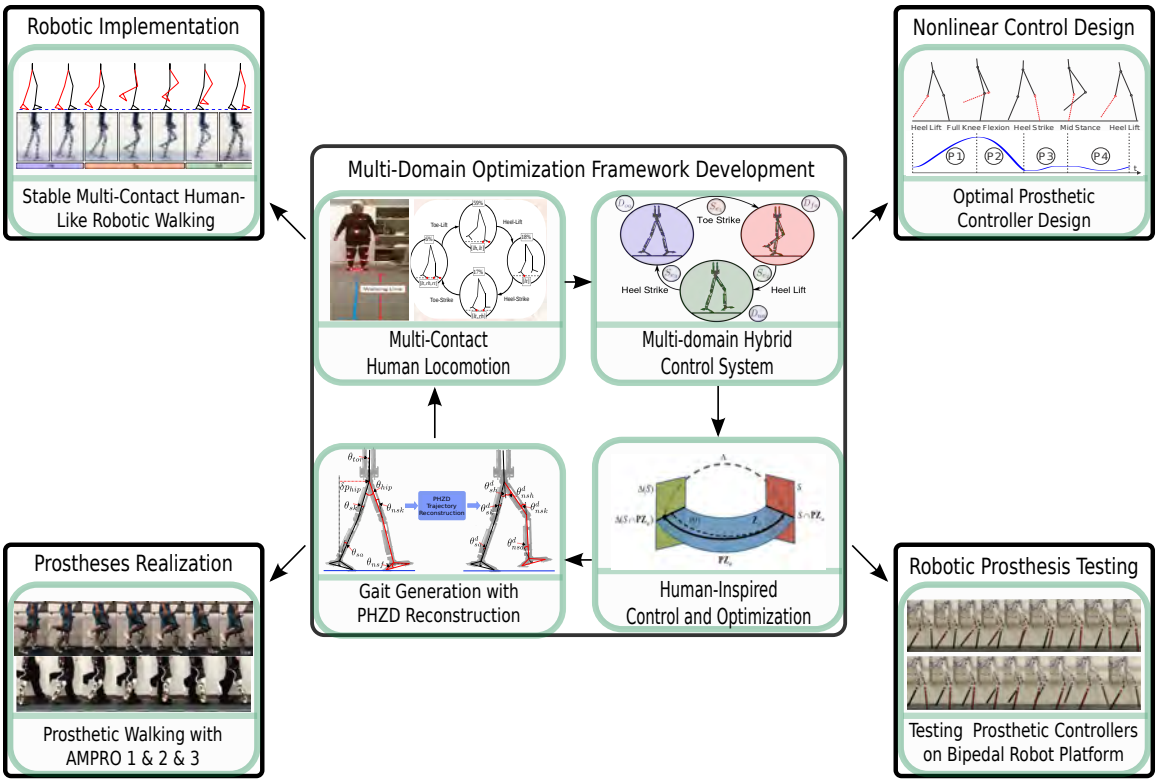

Figure 52: Contribution summarization of this dissertation.

in the optimization framework. The end result was a stable gait that can be applied to physical robots directly.

Robotic Implementation. Secondly, to experimentally validate the optimized multi-contact gaits, a physical robot AMBER2 was specifically designed and built for realizing multi-contact robotic walking. The hybrid system model of AMBER2 was constructed and the multi-domain optimization along with constraints was explicitly explained. The gait, which was designed using the multi-domain optimization framework was successfully realized on AMBER2 in experiment with achieving sustainable multi-contact robotic walking.

Nonlinear Control Design. With the goal of transferring bipedal robotic control to power prostheses, the first steps was taken to design controllers for prostheses. In particular, a RES-CLF motivated optimization-based nonlinear prosthetic controller was developed for realizing prosthetic walking that requires less parameter-tuning and is more energy efficient. This novel controller has two major advantages when

comparing to other traditional controllers such as variable impedance control. First, it does not require extensive tuning given a desired trajectory. Second, it solves control input in a point-wise optimal fashion while at the same times respecting hardware torque bounds.

Robotic Prosthesis Testing. The idea of using bipedal robot platform (which displays human-like walking) for testing prosthetic controllers was proposed. A systematic method was developed and verified on the physical robot AMBER1 in both simulation and experiment. The results showed that the novel nonlinear controller can perform better w.r.t both tracking and robustness.

Prostheses Realization. Finally, in order to transfer this systematic methodology—including automatic gait generation and nonlinear controller—to achieve prosthetic walking. Three generations of a powered transfemoral prosthesis (AMPRO1 & 3) were designed and built from the ground up. The effort included both software part and hardware part for developing these fully functional powered prosthetic legs with on-board processing and self-contained power. In particular, the software side covered robot modeling, control simulation, trajectory optimization and embedded software development. The hardware part consisted of electric parts selection, sensor fusion, PCB design and system integration. Stable human-like prosthetic walking with essential multi-contact feature were achieved with these prostheses. Both reduced tuning effort and improved energy performance were observed during these prosthetic walking. Additionally, motion intention recognition algorithm was developed to expand the functionality of the powered prostheses.

8.2 Future Work

With the two-step direct collocation optimization method for prosthetic gait design and the 3D capable SEA prosthetic device AMPRO3, this thesis opens up several interesting topics for future research. A few of the possible directions are listed below.

8.2.1 Control-in-the-Loop Prosthetic Design

The two-step direct collocation optimization method has the potential to consider much more complex models. In particular, the SEA joint can be potentially added in this optimization problem. In this way, spring constants for the SEA can be estimated based on the optimization problem with the goal of achieving optimal energy performance. A more realistic gait for AMPRO3 can also be designed with the existence of SEAs in the model.

8.2.2 Smart SEA Controller

AMPRO3 is equipped with two SEA joints, each of which has two encoders on both the motor side and joint side. This allows us to measure the actual torque applied on the joints. A low-level controller can be implemented to achieve smart SEA torque control. For example, during the weight acceptance phase (i.e., the beginning of stance phase after heel strike), the motor can be set at a fix position, which allows the torsional spring store energy. Then the motor can merge in when active turning is necessary.

8.2.3 Clinical Testing with Amputees

With the low-cost IMU motion capture system, the proposed optimization can be utilized to design gaits for different amputee subjects and motion types. It would be necessary to get feedback from clinical testing with different amputee subjects. In particular, metabolic cost and amputee feedback along with the device power consumption can be used as measures to further validate the proposed method in this dissertation.

APPENDIX I

MAIN THEORY PROOF

The proof of the **Main Theorem** can come directly from the proof for *Theorem 2* in [19] with the reconstructed single-domain hybrid zero dynamics system (51). Because of a multi-domain system can be reconstructed as a single-domain hybrid system, the only difference between a multi-domain hybrid system and a single domain hybrid system is the reset map. Similarly to the single domain case, in which the reset map is Lipschitz continuous [19], the main idea is to show that the meta reset map in (48) is also Lipschitz continuous, which we will show in the following.

The reset map of each domain can be explicitly stated as (14), which is a function of the inertial matrix $M(x)$. Because of the boundedness property of $M(x)$, we can conclude that the reset map for every transition is Lipschitz. For the purpose of proof, we could write (14) for each transition e_i using the zero dynamics coordinates $\Delta_{e_i}(\theta, \dot{\theta}) := \Delta_{e_i}(\eta_{v_i}, \xi_{v_i})$, For simplicity of notation,, we define $\Delta_{e_i}(\eta_{v_i}, \xi_{v_i}) = (\Delta^{\eta}_{e_i}(\eta_{v_i}, \xi_{v_i}), \Delta^{\xi}_{e_i}(\eta_{v_i}, \xi_{v_i}))$. Because of the Lipschitz property, we have

$$||\Delta^{\eta}_{e_i}(\eta_{v_i}, \xi_{v_i})|| = ||\Delta^{\eta}_{e_i}(\eta_{v_i}, \xi_{v_i}) - \Delta^{\eta}_{e_i}(0, \xi_{v_i})|| \leq L_{\Delta^{\eta}_{e_i}} ||\eta_{v_i}||. \tag{130}$$

By assumption that the dynamics of each domain is continuously differentiable, therefore, the flow $\varphi^{\varepsilon_i}_{v_i,t}$ is C^1. More importantly, from (81) and with applying the RES-CLF human-inspired controller (defined in (37) and (33)) on each domain, we have that

$$\begin{aligned} ||\varphi^{\varepsilon_i}_{v_i,t}(\eta_{v_i}, \xi_{v_i}) - \varphi^{\varepsilon_i}_{v_i,t}(0, \xi_{v_i})|| &\leq L_{\varphi^{\varepsilon_i}_{v_i}} ||\eta_{v_i}(t)|| \\ &\leq L_{\varphi^{\varepsilon_i}_{v_i}} \frac{1}{\varepsilon_i} \sqrt{\frac{c_2}{c_1}} e^{-\frac{c_3}{2\varepsilon_i} t} ||\eta_{v_i}(0)|| \end{aligned} \tag{131}$$

Now we have the framework to show that the general *Poincaré* map (44) is both Lipschitz and rapidly attractive. By definition, we can rewrite the general *Poincaré* map (44) as $P^{\varepsilon_i}_{v_i}(\eta_{v_{i-1}}, \xi_{v_{i-1}}) = \varphi^{\varepsilon_i}_{v_i, T^{\varepsilon_i}_{I_{v_i}}} \circ \Delta_{e_{i-1}}(\eta_{v_{i-1}}, \xi_{v_{i-1}})$. Additionally,

based on the Implicit Function Theorem [103], $T^{\varepsilon_i}_{I_{v_i}}$ is well-defined around a neighborhood of $(\eta^*_{v_{i-1}}, \xi^*_{v_{i-1}})$, which yields that we could find a constant $T_{I_{v_i}}$ such that $T^{\varepsilon_i}_{I_{v_i}}(\eta^*_{v_{i-1}}, \xi^*_{v_{i-1}}) = T_{I_{v_i}}$ [19]. Here $(\eta^*_{v_{i-1}}, \xi^*_{v_{i-1}})$ is a fixed point on $S^X_{e_{i-1}}$. Therefore, followed by the fact that if two sub-systems are Lipschitz the concatenate system is also Lipschitz, we have

$$\begin{aligned} ||P^{\varepsilon_i}_{v_i}(\eta_{v_{i-1}}, \xi_{v_{i-1}}) - P^{\varepsilon_i}_{v_i}(0, \xi_{v_{i-1}})|| &\leq L_{\Delta^\eta_{e_i}} L_{\varphi^{\varepsilon_i}_{v_i}} \frac{1}{\varepsilon_i} \sqrt{\frac{c_2}{c_1}} e^{-\frac{c_3}{2\varepsilon_i} t} ||\eta_{v_{i-1}}(0)|| \\ &\leq L^{\varepsilon_i}_{P^{\varepsilon_i}_{v_i}} ||\eta_{v_{i-1}}(0)|| \end{aligned} \tag{132}$$

More importantly, because we can choose ε_i sufficiently small, the *Poincaré* map can be rapidly exponential stable. This result is important in two perspectives. First, we show that the *Poincaré* map for domain v_i is Lipschitz w.r.t η_{v_i}. Secondly, by choosing small enough ε_i, the domain v_i can be guaranteed to converge to the zero dynamics sufficiently fast, i.e., the dynamics of domain v_i is attractive and behave properly with the human-inspired controller.

Single Domain Construction. With the goal of utilizing the framework of a single domain case in [19], it is necessary to introduce basic terms first based on the reconstructed single-domain hybrid system (47). Let $(\eta^*, \xi^*) \in \bar{S}$ a fixed point of hybrid system (47), we say that $\bar{\varphi}^\varepsilon_t$ is hybrid periodic for (47) if $\bar{\varphi}^\varepsilon_{t+\bar{T}}(\eta^*, \xi^*) = \varphi^\varepsilon_t(\eta^*, \xi^*)$ with period $\bar{T}$. Note that, by definition, the convergence gain ε here is simply ε_1 for domain v_i. Similarly, the hybrid periodic orbit can be defined as $\bar{\mathcal{O}} = \{\bar{\varphi}^\varepsilon_t(\bar{\Delta}(\eta^*, \xi^*)) | 0 < t < \bar{T}\}$. For a system with a hybrid zero dynamics periodic orbit, we know $\eta* = 0$. Additionally, without loss of generality, we can assume that $\xi^* = 0$ as well since we are focusing on local stability [19]. Taking $\bar{S}$ as a *Poincaré* section, we can define the *Poincaré* map $\bar{P}^\varepsilon : \bar{S} \to \bar{S}$, which is a partial function

$$\bar{P}^\varepsilon = \bar{\varphi}^\varepsilon_{\bar{T}^\varepsilon_I(\eta,\xi)}(\bar{\Delta}(\eta, \xi)), \tag{133}$$

where $(\eta, \xi) \in \bar{D}$ and $\bar{T}^\varepsilon_I : \bar{S} \to \bar{D}$ is the time-to-impact function defined as

$$\begin{aligned} \bar{T}^\varepsilon_I(\eta, \xi) := \inf\{t \geq 0 \mid \bar{\varphi}^\varepsilon_t(\bar{\Delta}(\eta, \xi)) \in \bar{S}\}, \\ \text{if } \exists\, t \text{ such that } \bar{\varphi}^\varepsilon_t(\bar{\Delta}(\eta, \xi)) \in \bar{S}, \end{aligned} \tag{134}$$

which is obtained through the Implicit Function Theorem [103] and the assumption that the function $\bar{H}(t,\eta,\xi) = \bar{h}(\bar{\varphi}_t^{\varepsilon}(\bar{\Delta}(\eta,\xi)))$ for which $\bar{H}(\bar{T},\eta^*,\xi^*) = 0$. By definition that on $\bar{S}$, $\frac{\partial H}{\partial t}(\bar{T},\eta^*,\xi^*) < 0$, the Implicit Function Theorem implies that $\bar{T}_I^{\varepsilon}$ is well-defined in a neighborhood of (η^*,ξ^*). Therefore, $\bar{T}_I^{\varepsilon}(\eta^*,\xi^*) = \bar{T}$ and $\bar{P}^{\varepsilon}(\eta^*,\xi^*) = (\eta^*,\xi^*)$. More importantly, because $\bar{H}(t,\eta,\xi)$ is Lipschitz continuous (since $\bar{h} = h_{v_1}$ is continuously differentiable by construction), we can conclude that both $\bar{\varphi}_t^{\varepsilon}(\bar{\Delta}(\eta,\xi))$ and $\bar{T}_I^{\varepsilon}$ are Lipschitz [19].

Similarly, we could define the corresponding *Poincaré* $\bar{\rho} : \bar{S} \cap \bar{Z} \to \bar{S} \cap \bar{Z}$ for the zero dynamics with a hybrid periodic orbit $\bar{\mathscr{O}}_Z$. In this case,

$$\bar{\rho}(\xi) = \bar{\varphi}^z_{\bar{T}_{\bar{\rho}}(\xi)}(\bar{\Delta}^z(0,\xi)), \tag{135}$$

where $\bar{\varphi}^z$ is the flow of $\dot{\xi} = \bar{q}(0,\xi)$ and $\bar{T}_{\bar{\rho}}(\xi)$ is the restricted time-to-impact function which is given by $\bar{T}_{\bar{\rho}}(\xi) = \bar{T}_I^{\varepsilon}(0,\xi)$.

With the above construction in hand, we could explicitly state a lemma to show that the meta reset map $\bar{\Delta}(\eta,\xi)$ is Lipschitz.

Lemma 1. *Let* (47) *be the reconstructed single domain hybrid system of the original multi-domain hybrid system* (2) *with a wrapped reset map* $\bar{\Delta}$ *defined as* (48)*, there exists* $\varepsilon_i \in (0,1)$ *with* $i \in \{2,...,N\}$ *and for all the human-inspired controllers in each domain* D_{v_i} *as defined in* (33) *and* (37)*,* $\bar{\Delta}$ *is Lipschitz w.r.t* η*, i.e.,*

$$||\bar{\Delta}(\eta,\xi) - \bar{\Delta}(0,\xi)|| \leq L_{\bar{\Delta}^{\eta}}^{\varepsilon_i}||\eta||. \tag{136}$$

Proof. With (130) and (132) for each domain D_{v_i}, the lemma can be proved by the fact that if two sub-system is Lipschitz, the complete system is also Lipschitz. □

Based on *Lemma 1* and the construction of the wrapped single domain hybrid system, the *Lemma 1* from [19] is also true here. In the following, $B_{\delta}(r)$ denotes an open ball of radius $\delta > 0$ centered on the point r, and $\bar{P}_{\xi}^{\varepsilon}(\eta,\xi)$ is the ξ-component of $\bar{P}^{\varepsilon}(\eta,\xi)$.

Lemma 2. *Let* $\bar{\mathscr{O}}_{\bar{Z}}$ *be a periodic orbit of the hybrid zero dynamics* $\bar{\mathscr{H}}_{\mathbf{Z}}$ *transverse to* $\bar{S} \cap \bar{Z}$ *and assume there exists a RES-CLF* V_{ε} *for the continuous dynamics* (39) *of*

$\bar{\mathscr{H}}$. *Then there exist finite constants* L_{T_I} *and* A_1 *(both independent of* ε*) such that for all* $\varepsilon > 0$ *and the human-inspired controller in* (33) *or* (37)*, there exists a* $\delta > 0$ *such that for all* $(\eta, \xi) \in B_\delta(0,0) \cap \bar{S}$

$$||\bar{T}_I^\varepsilon(\eta,\xi) - \bar{T}_{\bar{p}}(\xi)|| \leq L_{T_I}||\eta|| \tag{137}$$

$$||\bar{P}_\xi^\varepsilon(\eta,\xi) - \bar{\rho}(\xi)|| \leq A_1||\eta|| \tag{138}$$

Followed by the problem construction and the fact that the human-inspired controller (33) and (37) are RES-CLF controllers, proof of *Lemma 1* in [19] can also be applied here for the proof of *Lemma 2*. We now have the necessary framework in which we can develop stability guarantee for the reconstructed single domain hybrid system. This is followed by the *Theorem 2* in [19].

Theorem 1. *Let* $\bar{\mathscr{O}}_Z$ *be an exponentially stable periodic orbit of the hybrid zero dynamics* $\bar{\mathscr{H}}_{\mathbf{Z}}$ *transverse to* $\bar{S} \cap \bar{Z}$ *and assume there exists a RES-CLF* $V_{\bar{\varepsilon}}$ *for the continuous dynamics* (39) *of* $\bar{\mathscr{H}}$*. There exists* $\bar{\varepsilon} \in (0,1)$ *such that* $\bar{\varepsilon} = \min\{\varepsilon_1, \ldots, \varepsilon_N\}$ *with each* ε_i *belonging to the set* $(0,1)$ *for all the human-inspired controllers in each domain* D_v *as defined in* (33) *and* (37)*,* $\bar{\mathscr{O}} = \iota_0(\bar{\mathscr{O}}_Z)$ *is an exponentially stable periodic orbit for the full order dynamics of the reconstructed single domain hybrid system* (47).

Proof. The proof follows from the proof of *Theorem 2* in [19] with *Lemma 1* and *Lemma 2* being true. □

Since the reconstructed single domain hybrid system (47) is equivalent to the multi-domain hybrid system (2), *Theorem 1* here also guarantees the stability of the multi-domain hybrid system. Therefore, the **Main Theorem** is proved.

REFERENCES

[1] Learning Impedance Controller Parameters for Lower-Limb Prostheses. https://youtu.be/Q4O25BR5oG8.

[2] AMPRO1 walks with the nonlinear real-time optimization controller. http://youtu.be/NxJ7nMsJ63o.

[3] Realization of Multi-Contact Prosthetic Walking with AMPRO1. https://youtu.be/K6mKYrVYVwE.

[4] Realization of Stair Ascent and Motion Transitions with AMPRO1. https://youtu.be/oNZxkiiCnUg.

[5] Simulation of 3D Multi-Contact Prosthetic Walking. https://youtu.be/eH6NRq1OK3w.

[6] AMPRO3 walks outdoor in DC: https://youtu.be/YyVP_Rqm-fY.

[7] Multi-contact walking of AMPRO3: https://youtu.be/2MWUW4_FOuA.

[8] Multi-contact walking of PETMAN: https://youtu.be/mclbVTIYG8E.

[9] Robustness tests of AMBER2: http://youtu.be/q0FThc1fe_U.

[10] Sustained walking of AMBER2: http://youtu.be/VvkIdCKlL54.

[11] M. Ackermann. Dynamics and energetics of walking with prostheses. Stuttgart, 2007.

[12] Navid Aghasadeghi, Huihua Zhao, Levi J Hargrove, Aaron D Ames, Eric J Perreault, and Timothy Bretl. Learning impedance controller parameters for lower-limb prostheses. *Intelligent Robots and Systems (IROS), 2013 IEEE/RSJ International Conference on*, pages 4268–4274.

[13] Cheol Ki Ahn, Min Cheol Lee, and Seok Jo Go. Development of a biped robot with toes to improve gait pattern. In *Advanced Intelligent Mechatronics, 2003*

IEEE/ASME International Conference on, volume 2, pages 729–734. IEEE, 2003.

[14] Juan José Alcaraz-Jiménez, D Herrero-Pérez, and H Martínez-Barberá. Robust feedback control of zmp-based gait for the humanoid robot nao. *The International Journal of Robotics Research*, 32(9-10):1074–1088, 2013.

[15] Aaron D. Ames. *Robot Motion and Control 2011*, chapter First Steps toward Automatically Generating Bipedal Robotic Walking from Human Data, pages 89–116. Springer London, London, 2012.

[16] Aaron D. Ames. Human-inspired control of bipedal walking robots. *Automatic Control, IEEE Transactions on*, 59(5):1115 – 1130, 2014.

[17] Aaron D Ames, Eric A Cousineau, and Matthew J Powell. Dynamically stable bipedal robotic walking with nao via human-inspired hybrid zero dynamics. In *Proceedings of the 15th ACM international conference on Hybrid Systems: Computation and Control*, pages 135–144. ACM, 2012.

[18] Aaron D. Ames, K. Galloway, and Jessy W. Grizzle. Control lyapunov functions and hybrid zero dynamics. In *Decision and Control (CDC), 2012 IEEE 51st Annual Conference on*, pages 6837–6842.

[19] Aaron D Ames, Kevin Galloway, Koushil Sreenath, and Jessy W Grizzle. Rapidly exponentially stabilizing control lyapunov functions and hybrid zero dynamics. *Automatic Control, IEEE Transactions on*, 59(4):876–891, 2014.

[20] Aaron D Ames and Matthew Powell. Towards the unification of locomotion and manipulation through control lyapunov functions and quadratic programs. In *Control of Cyber-Physical Systems*, pages 219–240. Springer, 2013.

[21] Aaron D. Ames, Ramanarayan Vasudevan, and Ruzena Bajcsy. Human-data based cost of bipedal robotic walking. In *14th international conference on Hybrid systems: computation and control*, pages 153–162. ACM, 2011.

[22] Gunnar Andreasson and Lars Peterson. Effects of shoe and surface characteristics on lower limb injuries in sports. *Journal of Applied Biomechanics*, 2(3):202 – 9, 2010.

[23] Takemasa Arakawa and Toshio Fukuda. Natural motion trajectory generation of biped locomotion robot using genetic algorithm through energy optimization. In *Systems, Man, and Cybernetics, 1996., IEEE International Conference on*, volume 2, pages 1495–1500. IEEE, 1996.

[24] Zvi Artstein. Stabilization with relaxed controls. *Nonlinear Analysis: Theory, Methods & Applications*, 7(11):1163–1173, 1983.

[25] Derek P Atherton and S Majhi. Limitations of pid controllers. In *American Control Conference*, pages 3843–3847, 1999.

[26] Samuel Au, Max Berniker, and Hugh Herr. Powered ankle-foot prosthesis to assist level-ground and stair-descent gaits. *Neural Networks*, 21(4):654 – 666, 2008.

[27] Samuel K Au, Peter Dilworth, and Hugh Herr. An ankle-foot emulation system for the study of human walking biomechanics. In *IEEE Intl. Conf. Robotics and Automation*, pages 2939–2945, Orlando, 2006.

[28] Samuel K. Au and Hugh M. Herr. Powered ankle-foot prosthesis. *Robotics & automation magazine, IEEE*, 15(3):52–59, 2008.

[29] V. Azimi, D. Simon, H. Richter, and S. A. Fakoorian. Robust composite adaptive transfemoral prosthesis control with non-scalar boundary layer trajectories. In *American Control Conference (ACC)*, July 2016.

[30] Sven Behnke. Human-like walking using toes joint and straight stance leg. In *3RD International Symposium on Adaptive Motion in Animals and Machines*, 2005.

[31] Guy Bessonnet, Pascal Seguin, and Philippe Sardain. A parametric optimization approach to walking pattern synthesis. *The International Journal of Robotics Research*, 24(7):523–536, 2005.

[32] Joaquin A Blaya and Hugh Herr. Adaptive control of a variable-impedance ankle-foot orthosis to assist drop-foot gait. *Neural Systems and Rehabilitation Engineering, IEEE Transactions on*, 12(1):24–31, 2004.

[33] N. Alberto Borghese, L Bianchi, and F Lacquaniti. Kinematic determinants of human locomotion. *The Journal of physiology*, 494(Pt 3):863–879, 1996.

[34] Christine Chevallereau and Yannick Aoustin. Optimal reference trajectories for walking and running of a biped robot. *Robotica*, 19:557–569, 8 2001.

[35] Christine Chevallereau, Dalila Djoudi, and Jessy W Grizzle. Stable bipedal walking with foot rotation through direct regulation of the zero moment point. *Robotics, IEEE Transactions on*, 24(2):390–401, 2008.

[36] S. H. Collins, A. Ruina, R. Tedrake, and M. Wisse. Efficient bipedal robots based on passive-dynamic walkers. *Science*, 307:1082–1085, 2005.

[37] Steve H. Collins and Andy Ruina. A bipedal walking robot with efficient and human-like gait. In *Robotics and Automation, 2005. ICRA 2005. Proceedings of the 2005 IEEE International Conference on*, pages 1983–1988, April 2005.

[38] Frédéric Dierick, Massimo Penta, David Renaut, and Christine Detrembleur. A force measuring treadmill in clinical gait analysis. 20(3):299–303, December 2004.

[39] Timothy Dillingham. Limb amputation and limb deficiency: Epidemiology and recent trends in the united states. *Southern Medical Journal*, 2002.

[40] Aaron M. Dollar and Hugh Herr. Lower Extremity Exoskeletons and Active Orthoses: Challenges and State-of-the-Art. *IEEE Transactions on Robotics*, 24(1):144–158, 2008.

[41] W. R. Dyck, S. Onyshko, D. A. Hobson, and D. A. Winter. Voluntary controlled electro-hydraulic above-knee prosthesis. *Bull. Prosth. Res.*, pages 169–185, 1975.

[42] Kemalettin Erbatur, Akihiro Okazaki, Keisuke Obiya, Taro Takahashi, and Atsuo Kawamura. A study on the zero moment point measurement for biped

walking robots. In *Advanced Motion Control, 2002. 7th International Workshop on*, pages 431–436. IEEE, 2002.

[43] Woodie C Flowers and Robert W Mann. An electrohydraulic knee-torque controller for a prosthesis simulator. *Journal of biomechanical engineering*, 99(1):3–8, 1977.

[44] Randy Freeman and Petar V Kokotovic. *Robust nonlinear control design: state-space and Lyapunov techniques*. Springer Science & Business Media, 2008.

[45] Masahiro Fujita. Digital creatures for future entertainment robotics. In *Robotics and Automation, 2000. Proceedings. ICRA'00. IEEE International Conference on*, volume 1, pages 801–806. IEEE, 2000.

[46] Michael Gienger, K Loffler, and Friedrich Pfeiffer. Towards the design of a biped jogging robot. In *Robotics and Automation, 2001. IEEE International Conference on*, volume 4, pages 4140–4145. IEEE, 2001.

[47] Robert D. Gregg, Tommaso Lenzi, Levi J. Hargrove, and Jonathon W. Sensinger. Virtual constraint control of a powered prosthetic leg: From simulation to experiments with transfemoral amputees. *Robotics, IEEE Transactions on*, 30(6):1455–1471, Dec 2014.

[48] Jessy W. Grizzle, Christine Chevallereau, R. W. Sinnet, and Aaron D. Ames. Models, feedback control, and open problems of 3d bipedal robotic walking. *Automatica*, 50(8):1955 – 1988, 2014.

[49] K. A. Hamed and R. D. Gregg. Decentralized feedback controllers for exponential stabilization of hybrid periodic orbits: Application to robotic walking*. In *American Control Conference*, Boston, 2016.

[50] N. Handharu, J. Yoon, and G. Kim. Gait pattern generation with knee stretch motion for biped robot using toe and heel joints. In *Humanoid Robots, 8th IEEE-RAS International Conference on*, pages 265–270. IEEE, 2008.

[51] Ayonga Hereid, Eric A. Cousineau, Christian M. Hubicki, and Aaron D. Ames. 3D dynamic walking with underactuated humanoid robots: A direct collocation

framework for optimizing hybrid zero dynamics. In *To appear in the IEEE International Conference on Robotics and Automation (ICRA)*. IEEE, 2016.

[52] Ayonga Hereid, Christian M Hubicki, Eric A Cousineau, Jonathan W Hurst, and Aaron D Ames. Hybrid zero dynamics based multiple shooting optimization with applications to robotic walking. In *2015 IEEE International Conference on Robotics and Automation (ICRA)*, pages 5734–5740. IEEE, 2015.

[53] Ayonga Hereid, Shishir Kolathaya, Mikhail S Jones, Johnathan Van Why, Jonathan W Hurst, and Aaron D Ames. Dynamic multi-domain bipedal walking with atrias through slip based human-inspired control. In *17th International Conference on Hybrid Systems: Computation and Control*, pages 263–272. ACM, 2014.

[54] Masato Hirose1 and Kenichi Ogawa. Honda humanoid robots development. *Phil. Trans. R. Soc.*, 365(1850):11–19, Jan 2007.

[55] Daan GE Hobbelen and Martijn Wisse. Ankle actuation for limit cycle walkers. *The International Journal of Robotics Research*, 27(6):709–735, 2008.

[56] Neville Hogan. Impedance control: An approach to manipulation. pages 304–313, 1984.

[57] Kevin W. Hollander and Thomas G. Sugar. A robust control concept for robotic ankle gait assistance. In *Rehabilitation Robotics, ICORR, IEEE 10th International Conference on*, pages 119–123, 2007.

[58] He Huang, Fan Zhang, L.J. Hargrove, Zhi Dou, D.R. Rogers, and K.B. Englehart. Continuous locomotion-mode identification for prosthetic legs based on neuromuscular-mechanical fusion. *Biomedical Engineering, IEEE Transactions on*, 58(10):2867–2875, 2011.

[59] Qiang Huang, Kazuhito Yokoi, Shuuji Kajita, Kenji Kaneko, Hirohiko Arai, Noriho Koyachi, and Kazuo Tanie. Planning walking patterns for a biped robot. *IEEE Transactions on Robotics and Automation*, 17:280–289, 2001.

[60] Yildirim Hurmuzlu and Dan B Marghitu. Rigid body collisions of planar kinematic chains with multiple contact points. *Intl. J. of Robotics Research*, 13(1):82–92, 1994.

[61] Chris A Ihrke, Adam H Parsons, Joshua S Mehling, and Bryan Kristian Griffith. Planar torsion spring, US 20100145510. June 2010.

[62] I. Otto Bock Orthopedic Ind. Manual for the 3c100 otto bock c-leg. Duderstadt, Germany, 1998.

[63] V. T. Inman and J. Hanson. Human locomotion. In J. Rose and J. G. Gamble, editors, *Human Walking*. Williams & Wilkins, Baltimore, 1994.

[64] Ali Jadbabaie, Jie Yu, and John Hauser. Stabilizing receding horizon control of nonlinear systems: a control lyapunov function approach. In *American Control Conference, 1999. Proceedings of the 1999*, volume 3, pages 1535–1539. IEEE, 1999.

[65] SM. Jaegers, JH. Arendzen, and HJ. de Jongh. Prosthetic gait of unilateral transfemoral amputees: a kinematic study. *Archives of physical medicine and rehabilitation*, 76(8):736–743, 1995.

[66] K. Kaneko, F. Kanehiro, S. Kajita, K. Yokoyama, K. Akachi, T. Kawasaki, S. Ota, and T. Isozumi. Design of prototype humanoid robotics platform for hrp. In *Intelligent Robots and Systems, 2002. IEEE/RSJ International Conference on*, volume 3, pages 2431–2436 vol.3, 2002.

[67] I. Kato and H Tsuiki. The hydrauliclly powered biped walking machine with a high carrying capacity. In *In IV Symposium on External Control of Human Extremities*. Yugoslav Committee for Electronics and Automation, 1972.

[68] R.E. Kearney, I.W. Hunter, et al. System identification of human joint dynamics. *Critical reviews in biomedical engineering*, 18(1):55, 1990.

[69] Robert E Kearney and Ian W Hunter. System identification of human joint dynamics. *Critical reviews in biomedical engineering*, 18(1):55–87, 1989.

[70] Shishir Kolathaya, Wen-Loong Ma, and Aaron D. Ames. Composing dynamical systems to realize dynamic robotic dancing. pages 425–442, 2015.

[71] M. Kristic, I. Kanellakopoulos, and P. Kokotovic. *Nonlinear and Adaptive Control Design, Adaptive and Learning Systems for Signal Processing, Communications and Control*.

[72] Arthur D. Kuo. Energetics of actively powered locomotion using the simplest walking model. *Journal of Biomechanical Engineering*, pages 113–120, 2001.

[73] Jordan Lack, Matthew J Powell, and Aaron D Ames. Planar multi-contact bipedal walking using hybrid zero dynamics. *International Conference on Robotics and Automation 2014*, pages 2582 – 2588.

[74] B. Lawson, H.A. Varol, A. Huff, E. Erdemir, and M. Goldfarb. Control of stair ascent and descent with a powered transfemoral prosthesis. *Neural Systems and Rehabilitation Engineering, IEEE Transactions on*, 21(3):466–473, May 2013.

[75] Brain E. Lawson, Huseyin A. Varol, and Michael Goldfarb. Standing stability enhancement with an intelligent powered transfemoral prosthesis. *IEEE Transactions on Biomedical Engineering*, 58(9):2617–2624, Sept 2011.

[76] Yung-Hui Lee and Wei-Hsien Hong. Effects of shoe inserts and heel height on foot pressure, impact force, and perceived comfort during walking. 36(3):355–362, May 2005.

[77] Zhibin Li, Bram Vanderborght, Nikos G Tsagarakis, and Darwin G Caldwell. Human-like walking with straightened knees, toe-off and heel-strike for the humanoid robot icub. In *Control 2010, UKACC International Conference on*, pages 1–6, Sept 2010.

[78] Henk J Luinge and Peter H Veltink. Measuring orientation of human body segments using miniature gyroscopes and accelerometers. *Medical and Biological Engineering and computing*, 43(2):273–282, 2005.

[79] Wen-Loong Ma, Huihua Zhao, Shishir Kolathaya, and Aaron D. Ames. Human-inspired walking via unified pd and impedance control. In *2014 IEEE International Conference on Robotics and Automation (ICRA)*, pages 5088–5094. IEEE, 2014.

[80] J.B. MacNeil, RE Kearney, and IW Hunter. Identification of time-varying biological systems from ensemble data (joint dynamics application). *Biomedical Engineering, IEEE Transactions on*, 39(12):1213–1225, 1992.

[81] Ernesto C Martinez-Villalpando, Jeff Weber, Grant Elliott, and Hugh Herr. Design of an agonist-antagonist active knee prosthesis. pages 529–534, 2008.

[82] T. McGeer. Passive dynamic walking. *Intl. J. of Robotics Research*, 9(2):62–82, April 1990.

[83] T. McGeer. Passive walking with knees. In *IEEE Intl. Conf. on Robotics and Automation*, pages 1640–1645, Cincinnati, May 1990.

[84] Tad McGeer. Passive dynamic walking. *the international journal of robotics research*, 9(2):62–82, 1990.

[85] John W Michael and John H Bowker. *Atlas of amputations and limb deficiencies: surgical, prosthetic, and rehabilitation principles*. American Academy of Orthopaedic Surgeons, 2004.

[86] Nathan Miller, Odest Chadwicke Jenkins, Marcelo Kallmann, and Maja J Mataric. Motion capture from inertial sensing for untethered humanoid teleoperation. In *Humanoid Robots, 2004 4th IEEE/RAS International Conference on*, volume 2, pages 547–565. IEEE, 2004.

[87] Kazuhisa Mitobe, Genci Capi, and Yasuo Nasu. Control of walking robots based on manipulation of the zero moment point. *Robotica*, 18(06):651–657, 2000.

[88] Gaspar Mora, Rafael R Torrealba, José Cappelletto, Leonardo Fermín, G Fernández-López, and Juan C Grieco. Cybernetic knee prosthesis: application of an adaptive central pattern generator. *Kybernetes*, 41(1/2):192–205, 2012.

[89] David C Morgenroth, Ava D Segal, Karl E Zelik, Joseph M Czerniecki, Glenn K Klute, Peter G Adamczyk, Michael S Orendurff, Michael E Hahn, Steven H Collins, and Art D Kuo. The effect of prosthetic foot push-off on mechanical loading associated with knee osteoarthritis in lower extremity amputees. *Gait & posture*, 34(4):502–507, 2011.

[90] B. Morris and J. W. Grizzle. Hybrid invariant manifolds in systems with impulse effects with application to periodic locomotion in bipedal robots. *IEEE Transactions on Automatic Control*, 54(8):1751–1764, Aug 2009.

[91] Benjamin Morris and Jessy W. Grizzle. A restricted Poincaré map for determining exponentially stable periodic orbits in systems with impulse effects: Application to bipedal robots. In *IEEE Conf. on Decision and Control*, pages 4199 – 4206, Seville, Spain, 2005.

[92] Benjamin Morris, M.J. Powell, and A.D. Ames. Sufficient conditions for the lipschitz continuity of qp-based multi-objective control of humanoid robots. In *Decision and Control (CDC), 2013 IEEE 52nd Annual Conference on*, pages 2920–2926.

[93] Richard M. Murray, Zexiang Li, and Shankar S. Sastry. *A Mathematical Introduction to Robotic Manipulation*. CRC Press, Boca Raton, 1994.

[94] R.R. Neptune, S.A. Kautz, and F.E. Zajac. Contributions of the individual ankle plantar flexors to support, forward progression and swing initiation during walking. *J. of Biomechanics*, 34(11):1387–1398, 2001.

[95] Koichi Nishiwaki, Satoshi Kagami, Yasuo Kuniyoshi, Masayuki Inaba, and Hirochika Inoue. Toe joints that enhance bipedal and fullbody motion of humanoid robots. In *Robotics and Automation, 2002. Proceedings. ICRA '02. IEEE International Conference on*, volume 3, pages 3105–3110, 2002.

[96] Eric Perreault, Levi Hargrove, Daniel Ludvig, Hyunglae Lee, and Jon Sensinger. Considering limb impedance in the design and control of prosthetic devices. In *Neuro-Robotics*, pages 59–83. Springer, 2014.

[97] I. R. Petersen and B. R. Barmish. Control effort considerations in the stabilization of uncertain dynamical systems. In *American Control Conference, 1984*, pages 490–495, June 1984.

[98] Dejan Popovic, Rajko Tomovic, Dejan Tepavac, and Laszlo Schwirtlich. Control aspects of active above-knee prosthesis. *International Journal of Man-Machine Studies*, 35(6):751 – 767, 1991.

[99] David Quintero, Dario J. Villarreal, and Robert D. Gregg. Preliminary experiments with a unified controller for a powered knee-ankle prosthetic leg across walking speed. In *To appear in IEEE Int. Conf. Intelligent Robots & Systems*, June 2016.

[100] Daniel Roetenberg, Henk Luinge, and Per Slycke. Xsens mvn: full 6dof human motion tracking using miniature inertial sensors. *Xsens Motion Technologies BV, Tech. Rep*, 2009.

[101] Wilson J Rugh. *Linear system theory*, volume 2. prentice hall Upper Saddle River, NJ, 1996.

[102] Ricardo G Sanfelice. Control lyapunov functions and stabilizability of compact sets for hybrid systems. In *2011 50th IEEE Conference on Decision and Control and European Control Conference*, pages 7404–7409. IEEE, 2011.

[103] Shankar S. Sastry. *Nonlinear Systems: Analysis, Stability and Control*. Springer, New York, 1999.

[104] Ramzi Sellaouti, Olivier Stasse, Shuuji Kajita, Kazuhito Yokoi, and Abderrahmane Kheddar. Faster and smoother walking of humanoid HRP-2 with passive toe joints. In *Intelligent Robots and Systems, 2006 IEEE/RSJ International Conference on*, pages 4909–4914, Oct 2006.

[105] Amanda H Shultz, Brian E Lawson, and Michael Goldfarb. Running with a powered knee and ankle prosthesis. *IEEE Transactions on Neural Systems and Rehabilitation Engineering*, 23(3):403–412, 2015.

[106] Ann M Simon, Kimberly A Ingraham, Nicholas P Fey, Suzanne B Finucane, Robert D Lipschutz, Aaron J Young, and Levi J Hargrove. Configuring a powered knee and ankle prosthesis for transfemoral amputees within five specific ambulation modes. *PloS one*, 9(6):e99387, 2014.

[107] Rryan Sinnet, Matthew Powell, Rajiv P. Shah, and Aaron D. Ames. A human-inspired hybrid control approach to bipedal robotic walking. In *18th IFAC World Congress*, volume 18, pages 6904–6911, Milano, Italy, 2011.

[108] Ryan W Sinnet and Aaron D Ames. 2d bipedal walking with knees and feet: A hybrid control approach. In *Decision and Control, 2009. Proceedings of the 48th IEEE Conference on*, pages 3200–3207. IEEE, 2009.

[109] S Šlajpah, Roman Kamnik, and Marko Munih. Kinematics based sensory fusion for wearable motion assessment in human walking. *Computer methods and programs in biomedicine*, 116(2):131–144, 2014.

[110] Eduardo D Sontag. A universalconstruction of artstein's theorem on nonlinear stabilization. *Systems & control letters*, 13(2):117–123, 1989.

[111] Eduardo D Sontag. *Mathematical control theory: deterministic finite dimensional systems*, volume 6. Springer Science & Business Media, 2013.

[112] Frank Sup, Amit Bohara, and Michael Goldfarb. Design and Control of a Powered Transfemoral Prosthesis. *The International journal of robotics research*, 27(2):263–273, February 2008.

[113] Frank Sup, Huseyin Atakan Varol, and Michael Goldfarb. Upslope walking with a powered knee and ankle prosthesis: initial results with an amputee subject. *IEEE transactions on neural systems and rehabilitation engineering : a publication of the IEEE Engineering in Medicine and Biology Society*, 19:71–8, February 2011.

[114] D. H. Sutherland, K. R. Kaufman, and J. R. Moitoza. *Human Walking*. Williams & Wilkins, Baltimore, 1994.

[115] Taro Takahashi and Atsuo Kawamura. Posture control using foot toe and sole for biped walking robot" ken". In *Advanced Motion Control, 2002. 7th International Workshop on*, pages 437–442. IEEE, 2002.

[116] SAIDA Takao, Hirokazu Ohta, Yasuyoshi Yokokohji, and Tsuneo Yoshikawa. Function analysis of human-like mechanical foot, using mechanically constrained shoes. In *Intelligent Robots and Systems, 2004. IEEE/RSJ International Conference on*, volume 4, pages 3847–3852. IEEE.

[117] Hiroshi Takemura, Hiroya Iwama, Jun Ueda, and Tsukasa Ogasawara. A study of the toe function for human walking.

[118] David Tlalolini, Christine Chevallereau, and Yannick Aoustin. Comparison of different gaits with rotation of the feet for a planar biped. *Robotics and Autonomous Systems*, 57(4):371 – 383, 2009.

[119] David Tlalolini, Christine Chevallereau, and Yannick Aoustin. Human-like walking: Optimal motion of a bipedal robot with toe-rotation motion. *Mechatronics, IEEE/ASME Transactions on*, 16(2):310–320, April 2011.

[120] Michael R Tucker, Jeremy Olivier, Anna Pagel, Hannes Bleuler, Mohamed Bouri, Olivier Lambercy, José del R Millán, Robert Riener, Heike Vallery, and Roger Gassert. Control strategies for active lower extremity prosthetics and orthotics: a review. *Journal of neuroengineering and rehabilitation*, 12(1):1, 2015.

[121] Huseyin Atakan Varol, Frank Sup, and Michael Goldfarb. Multiclass real-time intent recognition of a powered lower limb prosthesis. *Biomedical Engineering, IEEE Transactions on*, 57(3):542–551, 2010.

[122] M. Vukobratović and B. Borovac. Zero-moment point—thirty-five years of its life. *Intl. J. of Humanoid Robotics*, 1(1):157–173, 2005.

[123] Miomir Vukobratović and Branislav Borovac. Zero-moment pointthirty five years of its life. *International Journal of Humanoid Robotics*, 1(01):157–173, 2004.

[124] Radcliffe C. W. Biomechanical basis for the design of prosthetic knee mechanisms. *Rehabilitation Engineering International Seminar*, 1980.

[125] TK Wang, MS Ju, and YG Tsuei. Adaptive control of above knee electro-hydraulic prosthesis. *Journal of biomechanical engineering*, 114(3):421–424, 1992.

[126] PL Weiss, RE Kearney, and IW Hunter. Position dependence of ankle joint dynamicsi. passive mechanics. *Journal of biomechanics*, 19(9):727–735, 1986.

[127] Eric Wendel and Aaron D. Ames. Rank properties of Poincaré maps for hybrid systems with applications to bipedal walking. In *Hybrid Systems: Computation and Control*, pages 151–60, Stockholm, Sweden, 2010.

[128] Eric R. Westervelt, Jessy W. Grizzle, Christine Chevallereau, Jun Ho Choi, and Benjamin Morris. *Feedback Control of Dynamic Bipedal Robot Locomotion*. CRC Press, 2007.

[129] Eric R. Westervelt, Jessy W. Grizzle, and D. E. Koditschek. Hybrid zero dynamics of planar biped walkers. *IEEE TAC*, 48(1):42–56, 2003.

[130] David A. Winter. *Biomechanics and Motor Control of Human Movement*. Wiley-Interscience, New York, 2 edition, 1990.

[131] David A. Winter. *The Biomechanics and Motor Control of Human Gait: Normal, Elderly, and Pathological*. University of Waterloo Press, 1991.

[132] Martijn Wisse and Jan Van Frankenhuyzen. Design and construction of mike; a 2-d autonomous biped based on passive dynamic walking. In *Adaptive motion of animals and machines*, pages 143–154. Springer, 2006.

[133] Shishir Nadubettu Yadukumar, Murali Pasupuleti, and Aaron D. Ames. Human-inspired underactuated bipedal robotic walking with amber on flat-ground, up-slope and uneven terrain. In *IEEE/RSJ International Conference on Intelligent Robots and Systems*, pages 2478–2483, Portugal, 2012.

[134] Shishir Nadubettu Yadukumar, Murali Pasupuleti, and Aaron D. Ames. From formal methods to algorithmic implementation of human inspired control on

bipedal robots. In *Algorithmic Foundations of Robotics X*, pages 511–526. Springer, 2013.

[135] Aaron J. Young, Ann M. Simon, and Levi J. Hargrove. An intent recognition strategy for transfemoral amputee ambulation across different locomotion modes. In *2013 35th Annual International Conference of the IEEE Engineering in Medicine and Biology Society (EMBC)*, pages 1587–1590, July 2013.

[136] Aaron J Young, Ann M Simon, and Levi J Hargrove. A training method for locomotion mode prediction using powered lower limb prostheses. *Neural Systems and Rehabilitation Engineering, IEEE Transactions on*, 22(3):671–677, May 2014.

[137] Guoqiang Zhang. Neural networks for classification: a survey. *Systems, Man, and Cybernetics, Part C: Applications and Reviews, IEEE Transactions on*, 30(4):451–462, Nov 2000.

[138] Huihua Zhao and Aaron D. Ames. Quadratic program based control of fully-actuated transfemoral prosthesis for flat-ground and up-slope locomotion. pages 4101 – 4107. IEEE, 2014.

[139] Huihua Zhao, Ayonga Hereid, Wen-loong Ma, and Aaron D. Ames. Multi-contact bipedal robotic locomotion. *Robotica*, FirstView:1–35, 4 2016.

[140] Huihua Zhao, Jonathan Horn, Jacob Reher, Victor Paredes, and A. D. Ames. A hybrid systems and optimization-based control approach to realizing multi-contact locomotion on transfemoral prostheses. *IEEE Transactions on Automation Science and Engineering*, Jan 2016.

[141] Huihua Zhao, Shishir Kolathaya, and Aaron D Ames. Quadratic programming and impedance control for transfemoral prosthesis. pages 1341 – 1347. IEEE, 2014.

[142] Huihua Zhao, Wen-Loong Ma, Michael B Zeagler, and Aaron D Ames. Human-inspired multi-contact locomotion with amber2. pages 199–210. IEEE, 2014.

[143] Huihua Zhao, Mathew Powell, and Aaron D. Ames. Human-inspired motion primitives and transitions for bipedal robotic locomotion in diverse terrain. *Optimal Control Applications and Methods*, 35:730–755, 2013.

[144] Huihua Zhao, Jacob Reher, Jonathan Horn, Victor Paredes, and Aaron D. Ames. Realization of nonlinear real-time optimization based controllers on self-contained transfemoral prosthesis. In *Proceedings of the ACM/IEEE Sixth International Conference on Cyber-Physical Systems*, pages 130–138, Seattle, WA, 2015. ACM.

[145] Huihua Zhao, Jacob Reher, Jonathan Horn, Victor Paredes, and Aaron D. Ames. Realization of stair ascent and motion transitions on prostheses utilizing optimization-based control and intent recognition. In *2015 IEEE International Conference on Rehabilitation Robotics (ICORR)*, pages 265–270, Aug 2015.

[146] Huihua Zhao, Shishir Nadubettu Yadukumar, and Aaron D. Ames. Bipedal robotic running with partial hybrid zero dynamics and human-inspired optimization. In *IROS, 2012 IEEE/RSJ International Conference on*, pages 1821–1827. IEEE, 2012.

[147] Kathryn Ziegler-Graham, Ellen J MacKenzie, Patti L Ephraim, Thomas G Travison, and Ron Brookmeyer. Estimating the prevalence of limb loss in the united states: 2005 to 2050. *Archives of physical medicine and rehabilitation*, 89(3):422–429, 2008.